Alma Mater Studiorum – Università di Bologna

DOTTORATO DI RICERCA IN
AUTOMOTIVE PER UNA MOBILITA' INTELLIGENTE

Ciclo 34

**Settore Concorsuale:** 09-B1 – TECNOLOGIE E SISTEMI DI LAVORAZIONE

**Settore scientifico disciplinare:** ING-IND/16 – TECNOLOGIE E SISTEMI DI LAVORAZIONE

DRY GRINDING TECHNOLOGY FOR AUTOMOTIVE GEARS
MANUFACTURING: PROCESS MODELLING AND OPTIMIZATION

**Presentata da:** Flavia Lerra

**Coordinatore Dottorato**                    **Supervisore**

Prof. Nicolò Cavina                           Prof. Alessandro Fortunato

                                              **Co-supervisore**

                                              Ing. Francesco Grippo

**Esame finale anno 2022**

# Index

# Figures index

# Tables index

# Abstract

The following thesis focused on the dry grinding process modelling and optimization for automotive gears production. A FEM model was implemented with the aim at predicting process temperatures and preventing grinding thermal defects on the material surface. In particular, the model was conceived to facilitate the choice of the grinding parameters during the design and the execution of the dry-hard finishing process developed and patented by the company Samputensili Machine Tools (EMAG Group) on automotive gears. The proposed model allows to analyse the influence of the technological parameters, comprising the grinding wheel specifications, on the grinding process temperatures and material microstructures. Automotive gears finished by dry-hard finishing process are supposed to reach the same quality target of the gears finished through the conventional wet grinding process with the advantage of reducing production costs and environmental pollution. But, the grinding process represents, among the material removing technologies, the one with the highest value of specific pressure and heat absorbed by the material, therefore, removing the lubricant increases the risk of thermal defects occurrence. An incorrect design of the process parameters set could cause grinding burns, which affect the mechanical performance of the ground component inevitably. Therefore, a modelling phase of the process could allow to enhance the mechanical characteristics of the components and avoid waste during production. A hierarchical FEM model was implemented to predict dry grinding temperatures and was represented by the interconnection of a microscopic and a macroscopic approach. A microscopic single grain grinding model was linked to a macroscopic thermal model to predict the dry grinding process temperatures and so to forecast the thermal cycle effect caused by the process parameters and the grinding wheel specification choice. At first, the model was elaborated on simple prismatic geometry to directly validate it with temperature measurements, subsequently, it was applied to the real gear geometry and validated through microstructural analysis to verify the relevance with the process. Good agreement between the model and the experiments was achieved making the dry-hard finishing an efficient and reliable technology to implement in the gears automotive industry.

# Introduction

In the last decades, much attention has been focused on social, economic and technical strategies aiming at reducing global environmental pollution. The automotive sector has also changed to deal with this question. Main sustainability research points to the life cycle assessment approach, the end-of-life perspective and the light-weight engineering and material selection studies [1]–[4]. In the automotive sector, in addition to the $CO_2$ emissions reduction, the green manufacturing also plays an important role [5] and this concept was applied also in the gear production chain.

Although the birth and growth of drivetrains of hybrid (HEV) and full electric (EV) vehicles has changed the concept of transmissions, the required gears amount is always considerable in demand and quality due to the introduction of evolved gearboxes [6], [7]. Rather recent studies of the global market for the manufacture of transmissions predict an increase in demand for high-speeds transmissions equal to 20% over the next five years considering automatic and dual-clutch 7-speed and above [8]. The considerable transmissions demands together with the gears production led gears producers to focus in gears and machines manufacturing capacity, trying to reduce process and machines cost and environmental impact [9]. Some of the recent developments to achieve sustainability in gear manufacturing comprise reducing the use of mineral-based cutting fluids by employing alternative lubricants [10] and lubrication techniques i.e. minimum quantity lubrication (MQL) [11], [12] and dry machining, material saving and waste reduction, minimizing energy consumption and reducing the number of gear manufacturing stages, eliminating the necessity of finishing processes by utilizing advanced methods such as gear rolling and wire electric-discharge machining (WEDM) and finally increasing productivity by minimizing tool wear at high gear cutting speeds through the use of alternative tool materials and coatings [13].

Recently, research on tool materials and machine architectures has led to the elimination of oil from many of the cutting processes [14], allowing, in the case of gear manufacturing, to have an almost entirely dry supply chain [15]. Grinding usually represents the final phase of a manufacturing chain because it aimed at reaching high dimensional and geometrical tolerances to satisfy the design specifications and it allows

to finish very hard materials, so it can follow a heat treatment step. But, nowadays, grinding continues to use huge amount of lubricant because it involves the highest specific energy values among machining processes during the material removal phase [16]. The high energy consumption during a grinding operation is mainly due to grains non-defined shape with prevalent negative cutting angles. Moreover, grinding generally adopts limited depth of cut and very high cutting speeds which usually increase process specific energy and temperature [17]. But, the complete elimination of oil could lead to a substantial reduction in costs and environmental pollution while keeping the gears standard requirement high [18].

The gear dry grinding process and machine were recently developed by Samputensili Machine Tools (EMAG Group) and are based on minimizing the material removed during the grinding by previously introducing, in the same finishing step, a defined skive-hobbing phase which removes the main part of the material allowance [19]. Even though the process was successfully applied to many industrial cases, it needs to be improved because an incorrect design of the process parameters set could cause thermal defects affecting the mechanical performance of the ground component.

The Ph.D. activities have been concentrated on implementing a model with the aim at predicting grinding burns occurrence on gear material and optimizing the gear dry grinding process. Micro and macroscopic aspects of the grinding process were considered in a hierarchical FEM combined model. At first the microscopic interaction between a single grain and the material was analysed through a mechanical removing material model developed in DEFORM 3D. It was validated by means of single grain grinding tests performed by measuring the grinding forces generated and allows to calculate the single grain grinding power of the process. The single grain grinding power consider the kinematic process parameters and the material properties and was used to design the moving heat source representing the pass of the grinding wheel in a macroscopic thermal model. A tangential grinding process was modelled in COMSOL MULTIPHYSICS version 5.4 and was validated through temperatures measurements by means of the application of embedded thermocouples in tangential grinding tests which adopted different grinding wheel specifications and process parameters. At the end the model was applied on the gear tooth geometry considering the actual gear generating grinding kinematics to evaluate the effect of two different grinding wheels on the gear surface

integrity and verified the approach definitively. In Figure 1 a-c the followed procedure was schematically shown.

In support of the activities carried out, the presented thesis was conceived to deal with the grinding technology with its physical and operative characteristics pointing to modeling the process and forecast thermal burns in function of the process parameters and grinding wheel specifications. To predict the process thermal outcomes derives from the necessity to optimize the finishing process applied on automotive gears with the innovative technology of dry grinding. Therefore, in Chapter 1, the current gear manufacturing chain will be described focusing on the grinding technology and its basic principles. In Chapter 2, the state of the art of grinding modeling and the current thermal burns prediction strategies will be analyzed. Contextually, advantage and limits of each modeling approach will be discussed. In Chapter 3, the context where the Ph.D. topic and activities were carried out will be explained in detail showing the main goals to achieve. Chapters 4 and 5 will describe the proposed model and will explain in detail the experimental procedure followed to validate the proposed approach. In particular, Chapter 4 will focus on the single grain grinding model and experiments, instead, Chapter 5 will concentrate on the thermal grinding model introducing the wheel specification analysis and showing the tangential grinding tests procedure followed. Finally, the conceived model, previously validated through temperature measurements and microstructural analysis on prismatic samples, will be applied to the gear tooth geometry and results will be reported in Chapter 6. The effect of two different grinding wheel specifications was analysed at equal other conditions to verify the model. Gear dry grinding tests followed by the microstructural analysis of the gear tooth were performed to effectively verified the thermal effect of the dry grinding process on the gears tooth flanks. Therefore, the model is theoretically made up of two main parts, the single grain grinding model and the thermal model, and the third step sees the application of the validated model on the gear tooth geometry to effectively replicate the gear dry grinding process.
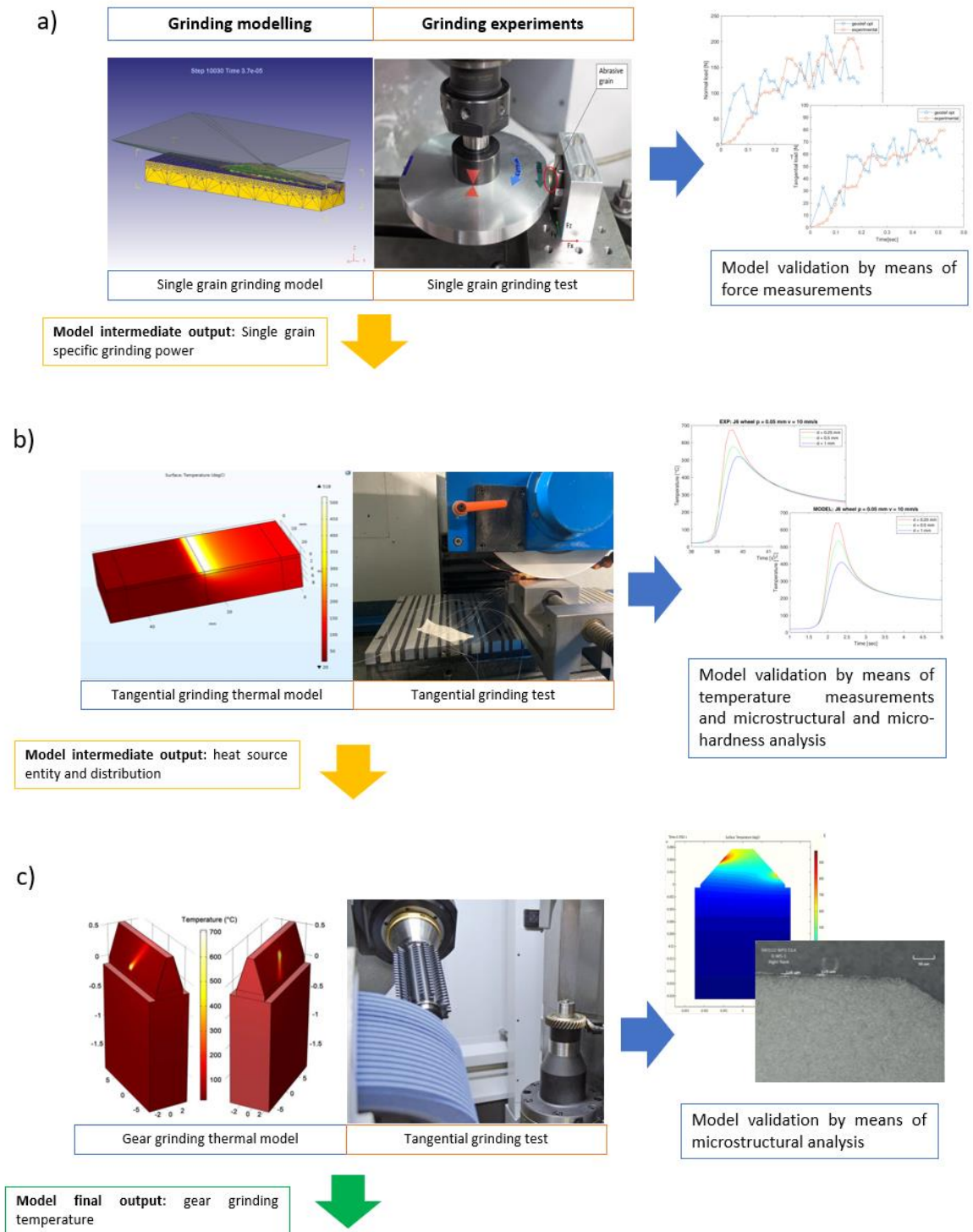
Figure 1. Grinding thermal defects prediction modelling and experimental procedure

# Chapter 1

## Theory of the grinding technology

In this chapter, the theory at the basis of the grinding technology will be described. Being the context focusing on gears grinding process, at first the attention will concentrate on the gears manufacturing processes that will be briefly described with particular attention to the production chain related to automotive gears. Subsequently, the focus will concentrate on the last step of the gear manufacturing route, that is the grinding process. The mechanics of the process will be described considering the material removal phenomena and the principal process parameters. The principal materials adopted for the grinding wheels manufacturing will be shown and a brief mention will be made of the lubricants commonly used in the process. This section will end with the analysis of the thermal defects induced by the process and their effect on the material.

### 1.1. Introduction to the gear grinding processes

In this work, the focus concentrated on the production chain and the grinding process of high-quality automotive transmissions. Therefore, only processes directly correlated to this field will be described in more details. Anyway, the classification of processes related to the roughing and finishing phase of teeth gears will be reported with particular emphasis on the gear grinding process alternatives.

Automotive transmissions have undergone a rapid development in recent years. Gearboxes with up to ten speeds and dual-clutch configurations or with planetary continuous gearboxes are nowadays mounted not only on the top cars brands but also in the large production. Being the gearboxes complexity and the number of gears increased, to minimize friction between the gears teeth to reduce wear, vibration and noise, became essential to maximize the performance of the transmissions. To make more progressive the teeth contact, gear design of tooth shapes has developed by introducing numerous corrections [20]. All automotive gears nowadays have helical teeth and present a crowning on both the profile and the lead. The high accuracy required on

the transmissions will therefore depend more on the final grinding phase, but of fundamental importance are also the previous cutting steps.

## 1.1.1. Gear roughing processes

Gear teeth could be produced based on plastic deformation or machining processes. In Figure 2 the gear roughing processes classification was reported. In the first case, gears could be produced through molding, forging, rolling, sintering and fusion. But to increase the productivity, gears generally are produced by machining, through milling and broaching, but more often through hobbing operations.
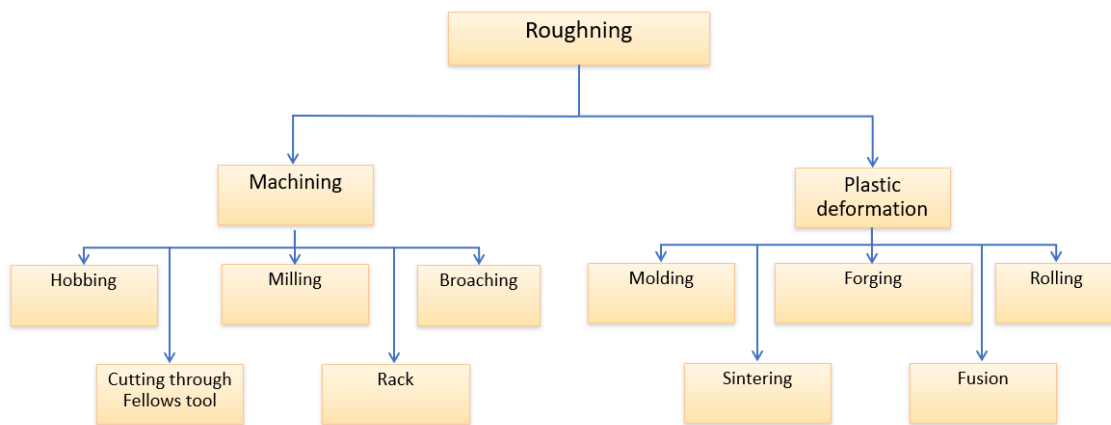


Figure 2. Gear roughing processes classification

Within the machining manufacturing processes, the cutting operations are divided into two main categories [21]:

- Division cutting, which takes place using shaped tools (mills or broaches).

- Envelope cutting, which is widespread in the automotive sector (Hobbing, Fellows cutter, rack) and involves the use of non-shaped tools and, ensuring lower costs and adapting very well to high production volumes.

Within gear cutting by division the generation of the teeth takes place using a form cutter. Through a chip removal process, the space between two consecutive teeth is generated, so that the side of the tooth traces the shape of the tool. The creation of the entire crown takes place by cutting one tooth at a time, rotating the workpiece by the appropriate angle, also using normal horizontal axis milling machines. Division cutting is a process rarely used in the manufacture of gear because, working one tooth at a time, the productivity is poor. A further disadvantage of this solution lies in the fact that each value of the module must correspond to a specific tool.

Envelope cutting is the most used manufacturing process to produce large series of automotive gears. The principle behind the latter is to move the cutting tool and the blank in which the toothed profile is gradually created as if they were a pair of conjugated toothed wheels that mesh with each other. The concomitance of the relative motion and the cutting action of the tool leads to the generation of the desired toothing in the piece. The main advantages of this solution are two: greater productivity and the possibility of producing different tooth shape with the same tool if they are characterized by the same module. There are several processes that exploit the principle of envelope for the teeth generation with an involute profile, among which the main ones are the hobbing, Fellows cutting and rack cutting. Among all these envelope cutting processes, gear hobbing is the most efficient method of manufacturing high-quality gears. The hob, reported in Figure 3, is a cutting tool, usually build in HSS or WC, used to cut the teeth into the cylindrical workpiece. It is cylindrical in shape with helical cutting teeth. These teeth have grooves towards the length of the hob, which aid in cutting and chip removal. The cross-section shape of the hob teeth is almost the same shape as teeth of a rack gear that usually is trapezoidal. The tool geometry in conjunction with appropriate machine tool kinematics leads to the same contact conditions as in the characteristic gears' pair [22].
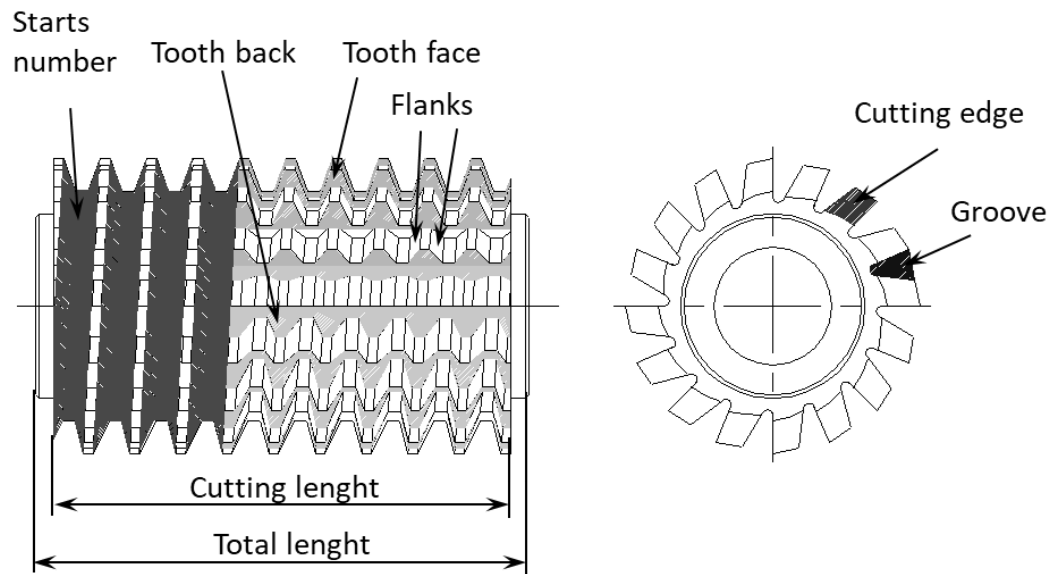
Figure 3. Hobbing tool

Form errors on the tooth profile are mainly due to three factors: the profile of the cutting edges, that is not exactly an involute, the axial feed of the tool and the discontinuous cut towards the flank since an entire flank is cut by the action of more hob teeth. Figure 4. Shape errors on profile and helix due to cutting with hob tool schematically represents the errors generated on the surface of the tooth after cutting with a hobbing tool and on the surface of a gear tooth acquired by contact profilometer. The error is due to the discontinuous cut which generates a tooth with a broken line profile that moves away from the theoretical involute shape. The angle $\varepsilon$ is the angle between the tangent line of two consecutive curves that make up the broken line of the real profile created. From a kinematics point of view, the angle $\varepsilon$ corresponds to the rotation that the component in machining performs in correspondence of a rotation $\theta$ of the hob. Given the condition of meshing between tool and piece, the angle $\varepsilon$ is expressed as a function of $\theta$:

$$\varepsilon = \frac{i \cdot \theta}{z} = \frac{2\pi \cdot i}{z \cdot n} \quad (1)$$

Where $i$ corresponds to the number of principles of the hobbing, while $z$ to the number of gear teeth and $n$ is the number of cutting edges engaged at each cutting pass.
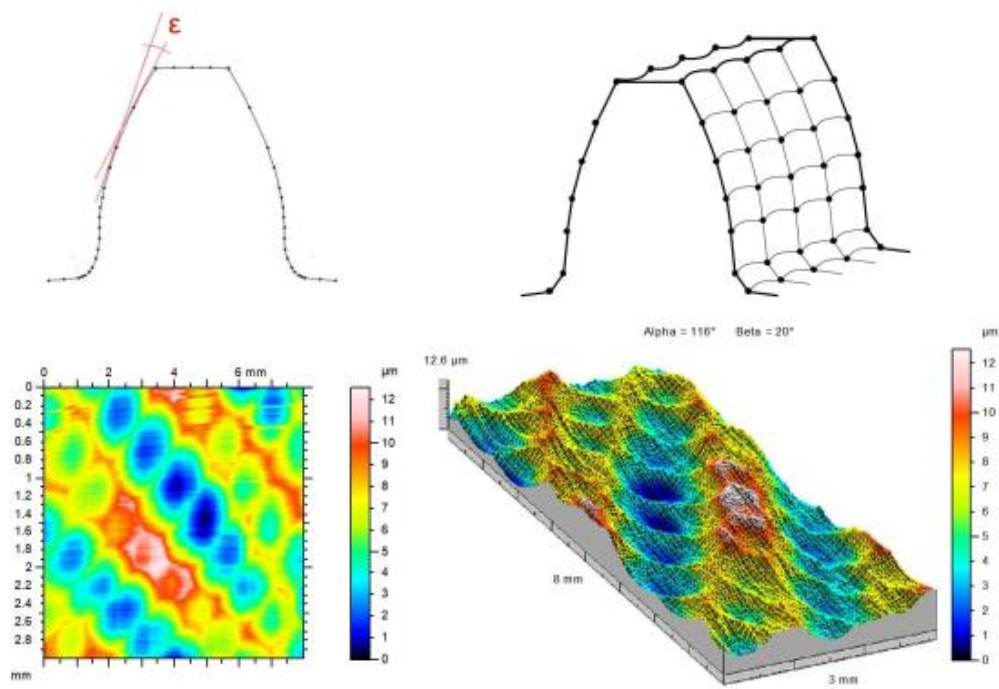
Figure 4. Shape errors on profile and helix due to cutting with hob tool

The errors on the profile can be reduced minimizing the amplitude of the angle ε. This could be achieved by designing the creator with a minimum number of principles and a maximum number of teeth possible, therefore, it needs to present a large diameter with the same module *m*. But these two conditions (number of starts equal to 1 and maximum diameter possible) affect other aspects of the process, such as the productivity, indeed, the following problematics could be involved:

- Larger diameter means higher cost of the tool per material.
- Larger diameter causes an increase in the weight of the hob, increase in inertia in machine and the difficulties in handling the tool.
- Lower number of principles leads to longer working time, as by decreasing the hob angular speed, also the gear angular speed decreases and so the generation speed decreases.

## 1.1.2. Gear finishing processes

Gear finishing processes are necessary to recover geometric errors left by previous hobbing. Within the industrial gear manufacturing there are two main alternatives, that consist in adopting a defined or an undefined tool geometry (Figure 5). In the first case, the shaping is a finishing process that allows to obtain, at low cost, a good surface quality, both in terms of geometry and roughness. However, one of its major limitations lies in the fact that the shaping cannot be applied to heat treated gears. Hardening, nitriding or carburizing must in fact be carried out after shaving with consequent geometric and dimensional distortions that lead to lower efficiency and greater noise of the transmission. The shaving tool is geometrically similar to an evolving gear wheel in which, along its teeth, grooves are obtained and contain the sharp edges. The working kinematics is carried out by the gear of the shaving tool with the gear to be finished. To date, the shaving tool represents a gear finishing alternative, but the most commonly used in automotive gears production is the grinding process thanks to its ability to finish hardened material.
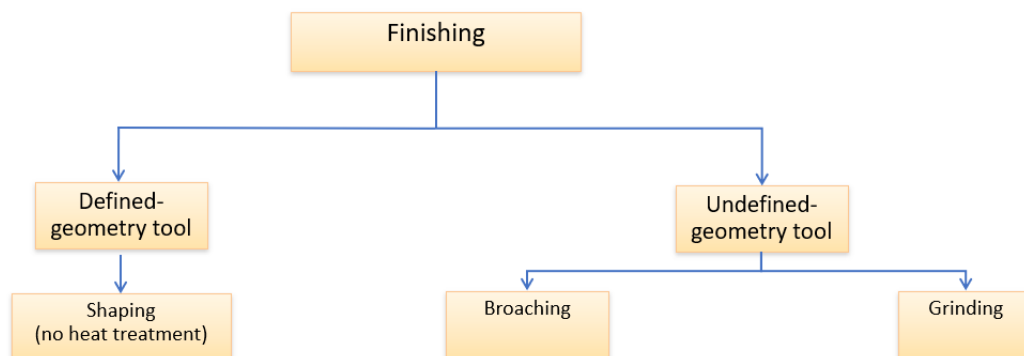
Figure 5. Gear finishing processes classification

## 1.1.3. Gear grinding processes

High-quality automotive gears were usually finished by grinding. The grinding process is characterized by cutting speeds up to 100 m/s that allow to remove very small allowances and reach very high dimensional accuracy with surface roughness lower than those obtained with traditional finishing processes. Moreover, given the extreme hardness

of the abrasive grains, the process can also be easily applied to heat treated gears. Therefore, the most suitable process to finish gears in the mass production field with high quality is the grinding because it can be applied after heat treatment reducing distortions risk. Grinding operations have the objective to generate very contained surface roughness (Ra < 1 µm) with excellent geometric and dimensional tolerances, so very high cutting speed and reduced material removal rate are used, because shape changes are not required [23]. In Figure 6 the gear grinding processes are classified in generating and profile grinding and both could be continous or discontinous based on the tool kinematics. With discontinuous profile grinding, the tooth flanks of a gear can be ground separately. It is currently applied for modules of 1–35 mm for internal and external spur-gears manufacturing. The essential characteristic of profile grinding is the identical shape geometry of the grinding wheel and the tooth gap which is supposed to be ground [24]. The continuous profile grinding of tooth flanks is applied by using a globoid worm shaped grinding wheel which can only be used for one specific workpiece geometry.
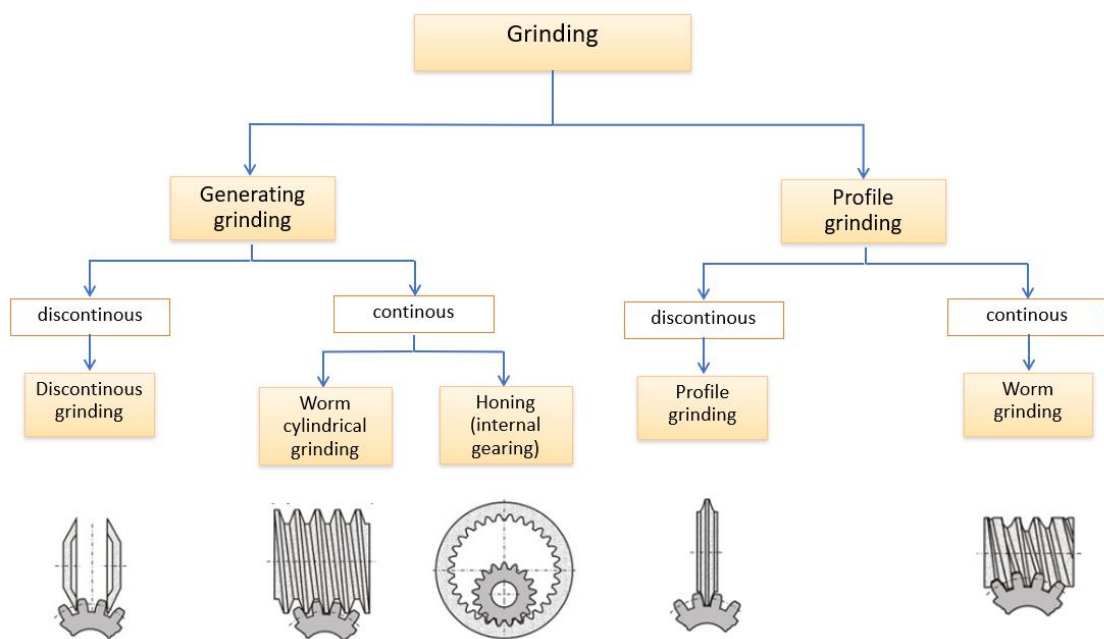


Figure 6. Gear grinding processes classification

For cylindrical and conical gears, the most established process is generating gear grinding. Discontinuous generating grinding can be distinguished between one flank and two flanks grinding. One flank grinding, which has a varying grinding wheel width, generates a better gearing accuracy compared to two flank grinding. This process is less productive compared to the more competitive processes like the discontinuous profile grinding. Honing process specific advantages are the possibility of adjustment of gearing failures and the favourable surface structure in height and width direction of the tooth flank. A gear shaped body with abrasive material is used as tool, which removes material from the tooth flanks under crossing rotational axes. For the honing of external gearing, a ring shaped tool with an integrated internal gearing is used [23]. In 1945 continuous generating grinding was employed for the first time to manufacture spur gears. The shape of the grinding worm corresponds with the profile of a straight gear rack. The geometry of the worm grinding wheel only depends on the workpiece geometry regarding module and penetration angle. The science-based analysis of generating gear grinding is complex due to the continuously changing contact conditions between tool and gear flank. In comparison with other grinding processes in generating gear grinding always multiple points of the grinding tool are in contact [25]. This motion of the contact points is called contact sequence and can be a reason for the characteristic dynamic excitation of the generating gear grinding process due to varying cutting forces during the generating process [26].

Manufacture of gears needs several processing operations in sequential stages depending upon the material, the type of the gears and the quality desired. Generally, high-quality automotive gears are made starting from the raw material which could be forged or rolled, then a hobbing phase follows to obtain rough teeth around the cylindrical surface. A phase of de-burring and chamfer could be applied to improve the gear quality, followed by the heat treatment, generally represented by case-hardening. Finally, the hobbed and heat-treated gears are finished by means of a grinding operation. Among grinding processes, automotive gears mass production generally adopts generating grinding and the worm grinding wheel to enhance productivity. Therefore, top range gear production process can be summarized as follows:

1. Raw material turning
2. Hobbing
3. De-burring
4. Chamfer
5. Heat treatment
6. Generating grinding

The materials of most of the gears used for transmitting reasonable torque and speed mainly need to be mechanically strong in shear and bending, sufficiently tough and resistant to wear, fatigue and chemical degradation. Generally, the gear material is selected based on the working condition, i.e., power, speed and torque to be transmitted, working environment, such as temperature, vibration and chemical conditions and overall cost of material and manufacture. The materials generally used in gear automotive production for high performance are high carbon steels and alloy steels (Ni-Cr, Mo etc.) which are either surface hardened for use under high stresses and speed [27].

## 1.2.    The basic principles of grinding processes

Grinding is an abrasive machining process that adopts very hard material particles and aims at enhancing the dimensional tolerances and the surface integrity of the manufactured parts. Beyond accuracy and surface texture requirements, another relevant characteristic of grinding process is the possibility to finish hard materials and/or hardened surfaces. The grinding process could lead to very low roughness values guaranteeing the best surface quality among all the other machining processes. Therefore, it is usually applied at the end of a manufacturing chain.

Grinding is an ancient technology; indeed, the history of grinding technology originates with the discovery of abrasive minerals and continues until today with the development of machine tools and grinding wheel materials.

Grinding machines primary functional requirements aim at obtaining high static and dynamic stiffness, fatigue strength, damping, thermal and long-term stability and low weight for moving parts. But, as the grinding is the finishing process, grinding machine

manufacturers have a relevant interest to reduce vibrations and distortions due to thermal effects [28]. Currently, the types of grinding machine tools vary from the simplest and cheapest alternative grinding machines to very complex and expensive machines with more than 5 controlled axes. Many grinding machines combine the use of computer-controlled spindles and linear tables that allow the creation of very complex shapes automatically without the intervention of a manual operator. In addition to this, being the grinding process a highly non-stationary process, development and implementation of the process control became essential [29]. The recent introduction of sensor and intelligent monitoring systems offer potential for increasing the process performance.

Considering the developments in grinding wheels, the manufacture of high performance grinding wheels is heavily dependent on the correct abrasive grain material in terms of shape, cutting ability and fracturing ability that influence the material removal rate, dressing interval, coolant delivery to the wheel-workpiece interface and chip evacuation [30]. Progress in increasing the productivity of grinding processes has been possible thanks to research carried out on the abrasive materials involved in the process. The range of possibilities offered by the abrasive industry has expanded with the introduction of new ceramic abrasives based on sol-gel technologies, the development of super abrasives in cubic boron nitride (CBN) and natural and synthetic diamond abrasives.

Nowadays, grinding is a major manufacturing process which accounts for about 20–25% of the total expenditures on machining operations in industrialized countries [31] and it is highly specialized to meet particular process and product requirements [32]–[34]. Obtaining such high levels of finishing leads the grinding processes to be characterized by a very low material removal rate and therefore, they are not used to change the shape of the part but only to ensure the required surface quality.

In this section, the physical phenomena at the basis of the grinding mechanism will be described and its main process parameters will be discussed with a brief mention to the commonly used lubricants. Grinding wheels configurations and materials characteristics will be also described and the thermal defects induced by grinding will be analysed considering the process like a fast-heating thermal cycle.

## 1.2.1. Grinding mechanics

The grinding tool is a grinding wheel working with high surface speed compared to other machining processes. Generally, the main elements representing a grinding operation could be indicated as the workpiece, the grinding wheel coupled to the grinding machine, the lubricant and the generated swarf. The lubricants are usually involved in the grinding process because they can reduce the huge amount of heat generated during the process and remove the swarf from the working zone. Chip formation and material removal depend mainly on the grinding wheel characteristics, the work material and the grinding kinematic parameters [35]. The chips produced in grinding are relatively small and their dimensions are variable due to the randomly oriented cutting edges on the grinding wheel. In addition, a dressing tool always equip the grinding machine and aims at sharpening the wheel. In Figure 7 the basic elements of a surface grinding operation are shown.
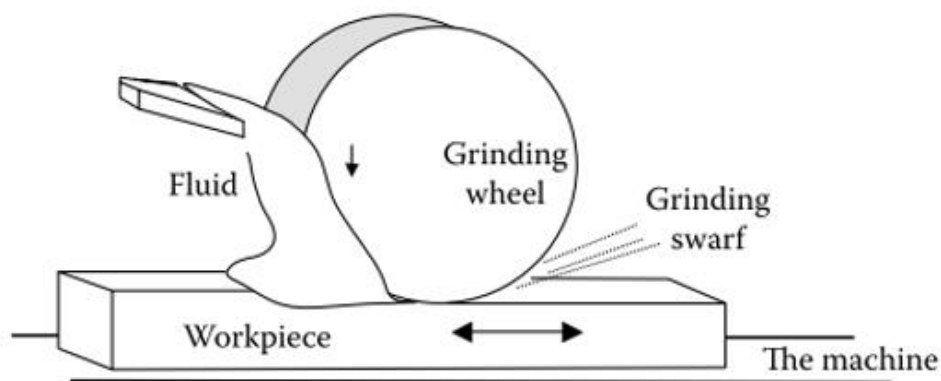
Figure 7. Surface grinding configuration and elements [36]

Summarizing, the main elements of an abrasive removal processes are:

- The component being processed characterized by the material, the shape, the hardness, the thermal and chemical properties;
- The abrasive tool with its structure, binder material and hardness, particle material and size, rotation speed, thermal and chemical properties;

- The geometry and kinematics parameters that define the contact between the abrasive tool and the workpiece
- The fluid with its flow, speed, pressure, physical, thermal and chemical properties;
- The machine: accuracy, stiffness, thermal stability, vibration.

The examination of material removal methods in grinding is difficult due to a variety of circumstances. The abrasives are initially three-dimensional and statistically dispersed throughout the grinding wheel's volume. The single cutting edges have a complicated form, and the operation involves simultaneous engagement of them. As a result, surface formation is the assemblage of these interdependent contacts, which are stochastically distributed. Furthermore, the production of chips during grinding occurs within a few microns, making observation even more challenging.

Grinding, from a technological point of view, is a process characterized by indeterminate geometry tool due to the non-deterministic shape and structure of grains. Aside from the uncertainty caused by the undefined abrasive particle forms, another element making the grinding process difficult to manage is the increased process specific energy caused by negative cutting angles. The prevalence of grains with negative cutting angles causes massive deformations and residual stresses in the material, implying the production of a hardened chip that allows to need higher forces and energy consumption during the material removal. Furthermore, unlike built-up edges, large negative rake angles tend to develop a stable stagnant region on the rake face from the start of cutting, and its size and shape do not change throughout cutting, influencing tool life, surface roughness, and dimensional accuracy of the workpiece [37], [38]. Furthermore, because of the depth of cut is limited and the material removal occur with negative rake angles, cutting pressures can reach extremely high levels. As a result of these circumstances, grinding is the machining method that produces the most highest levels of heat [21].

During material removal action, it can be noticed three different deformation zones (Figure 8):

1) Primary deformation zone (I), where contact between grain and workpiece starts and the deformation is predominantly elastic;

2) Secondary deformation zone (II), where the grain sinks in the material and plastic deformation occurs;

3) Tertiary deformation zone (III), where deformation is maximum and material removal occurs.

The rubbing phase (I), which is caused only by elastic deformation, is the shortest one and has a minor contribution to material removal. The ploughing phase (II) includes both elastic and plastic deformation but does not include chip removal. It is crucial in the creation of the surface and the generation of heat during the process. Grinding specific energy is substantially higher than other cutting processes because the ploughing process consumes a lot of energy without directly contributing to material removal. The production of severely distorted chips occurs during this phase, necessitating the employment of high energy to complete the process. Finally, the cutting phase (III), which comprises elastic and plastic deformation as well as chip removal, is where the real chip production takes place. Because it expends energy to remove materials and produce new surfaces, this phase is considered the most desirable.
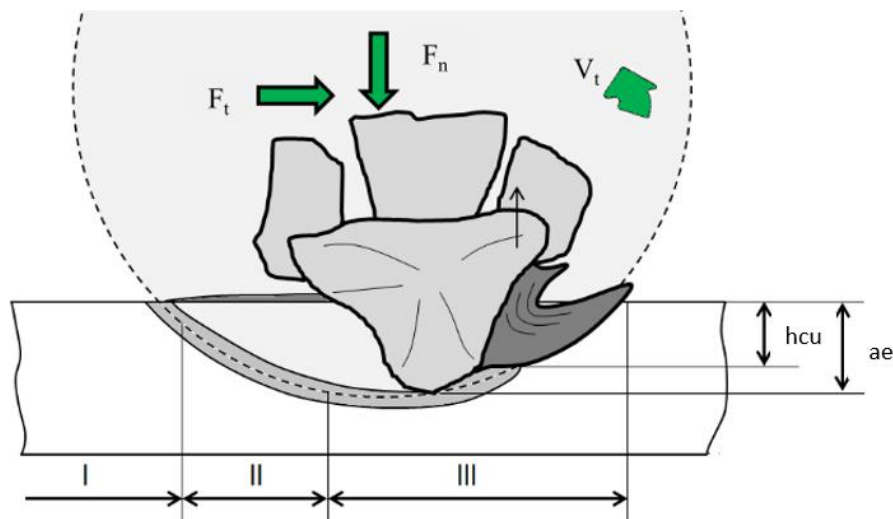


Figure 8. Grinding material removal mechanisms

Considering also the workpiece materials properties, the material removal mechanisms could be distinguished in micro-ploughing, microchipping, and microbreaking [36].

Micro-ploughing involves elastic and plastic deformations, whereas micro-chipping, as previously said, results in chip creation. Micro-breaking, in addition to micro-ploughing and microchipping, is a possible material removal process. When a fracture forms and spreads, it is common for micro-breaking to occur. This material removal mechanism is most likely to occur in the machining of brittle-hard materials like glass, ceramics, and silicon.
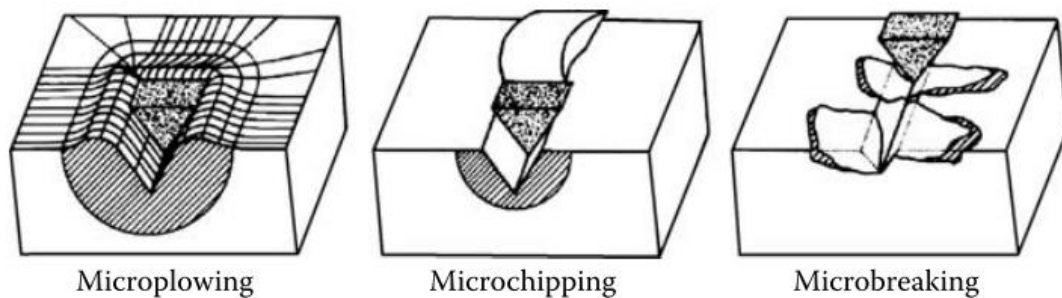


Figure 9. Material removal processes

Considering the chip formation process during the machining of ductile materials with high cutting speeds (Figure 10), it can be noticed that, at the beginning of the contact length (phase 1), the engaging abrasive grain first makes a groove, causing plastic and elastic deformation in the material. A flow chip is withdrawn, squeezed, and bent in response to the pore space as the cutting edge advances farther (phase 2). The chip is flat and offers a broad surface for heat transfer by radiation and convection due to the great point angle of a cutting edge. The working contact ends in the third phase (phase 3), if the penetration depth is small; otherwise, the cutting edge enters the material deeper. The high pressure creates strong material accumulation, which raises the contact zone temperature and tends to melt the produced chip, increasing the heat absorbed by the material that cannot be evacuated by the lubricant (phase 4). After the thread-shaped chip falls off, the entire material is liquefied in the pore space if the engagement occurs along the entire contact length (phase 5). The molten chip turns spherical after leaving the contact surface due to surface tension, and this occurs in a zone where there is no or only a small amount of cooling lubricant (phase 6).
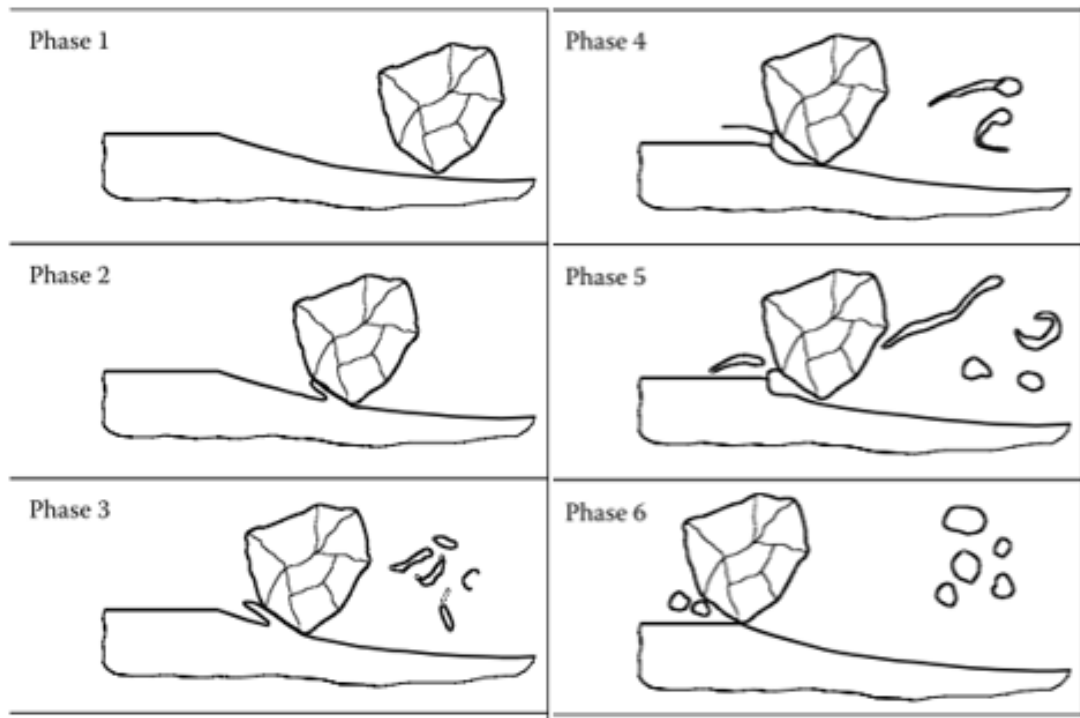
Figure 10. Removal process during the machining with high cutting speeds [36]

When the grit penetration depth reaches the critical cutting depth *T* after the rubbing and ploughing stages, the cutting phase begins, and the chip is removed. The critical cutting depth depends on the materials used and the process conditions. Furthermore, as friction increases, the critical cutting depth reduces, implying a reduction in plastic deformation in the dry grinding process because the cutting phase occurs faster, resulting in a reduced chip thickness. Generally, removed allowances $h_{cu}$ are lower than the value set in the machine ($a_e$) because of the material elastic springback, the tool deviation from the workpiece due to system deformation and the thermal expansions due to the heat dissipation and the wheel wear, as reported in Eq. (1):

$$h_{cu} << a_e \quad (1)$$

where $h_{cu}$ represents chip thickness and $a_e$ depth of cut value set.

## 1.2.2. Grinding parameters

There are numerous types of grinding operations which vary according to the shape of the wheel and the kinematic motions of the workpiece and grinding wheel. Some of the most common ones for machining flat and cylindrical surfaces are illustrated in Figure 11.
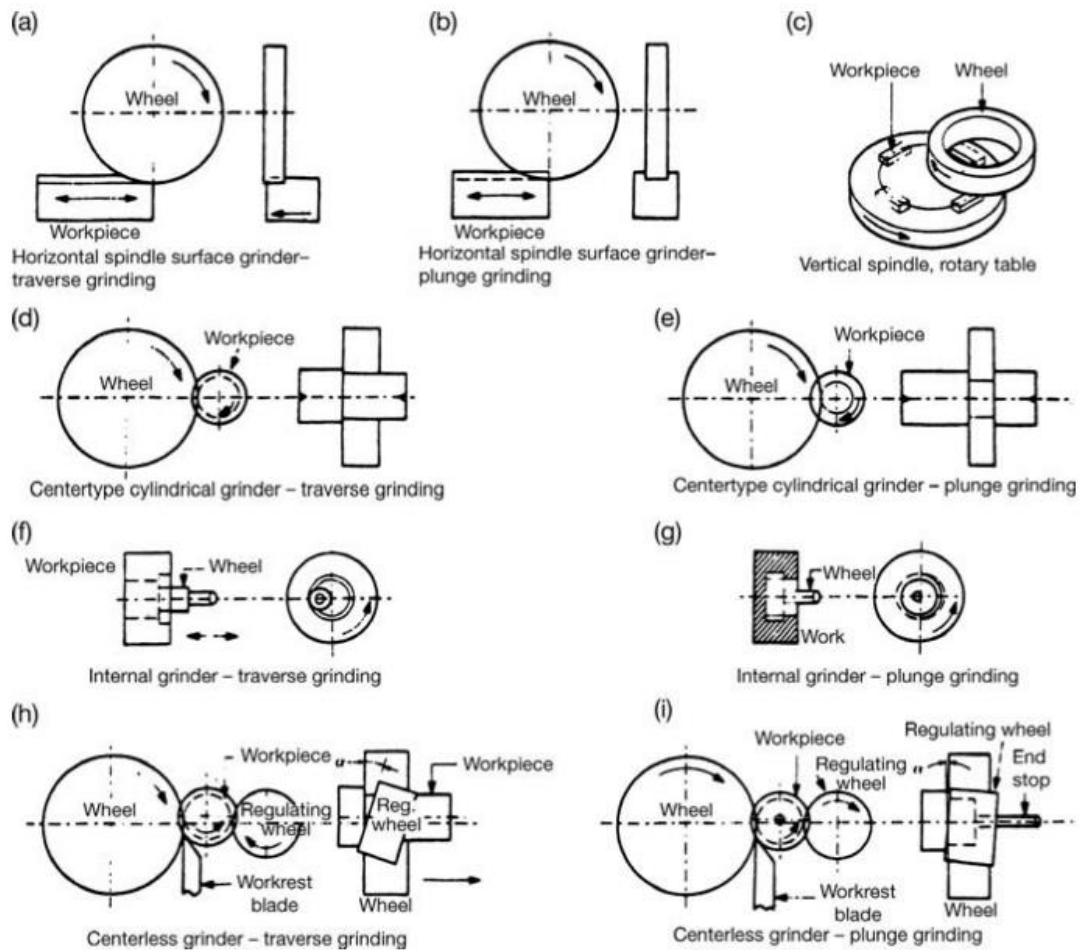


Figure 11. Illustration of some common grinding operations for machining flat and cylindrical surfaces [31]

In general, the working motions in a grinding operation are correlated to the kinematic parameters, as follows:

- The cutting motion, that is held by the grinding wheel, is rotational and defined by the *cutting speed $v_s$* parameter;
- The feed motion, that could be held by the grinding wheel and/or the workpiece, is rectilinear and defined by the *feed rate $v_w$* parameter;
- The stock motion, held by the grinding wheel and defined by *depth of cut $a_e$* parameter.

More complex machines and kinematics motion are adopted to generate other shapes. In gear grinding process (Figure 12), the cutting motion $n_o$, the feed motion $f_a$ and the stock motion $a_e$ are held by the worm grinding wheel and the gear moves with the generation motion $n$ which must respect the geometrical engagement between the two parts in contact required by the gear design.
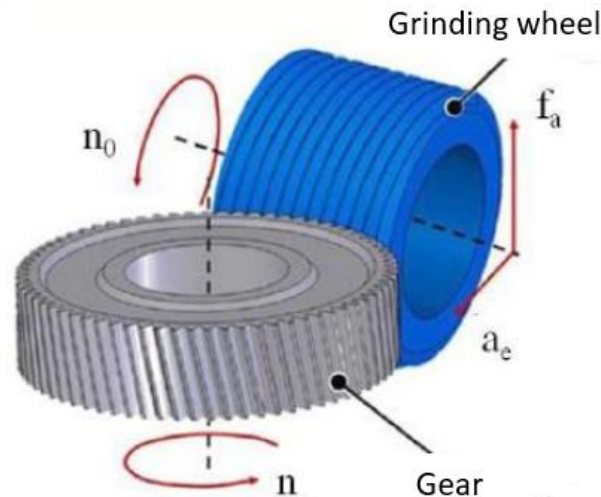


Figure 12. Gear grinding process kinematic motions

The grinding process differs from the other machining processes especially for the very high cutting speed adopted. Indeed, in conventional grinding, speeds are typically in the range of 20 m/s to 45 m/s. Instead, in high-speed grinding, speeds reach values of 140 m/s with wheels especially designed to withstand the high bursting stresses [39]. In gear grinding, the grinding wheel moves to a speed of 60 m/s to a maximum value of 80 m/s in function of the grinding wheel adopted. A further shifting motion could be assign to

the wheel. The wheel assumes an axial motion which guarantee that new grinding wheel surfaces are used in the cutting so as to compensate for tool wear.

Among process parameter, much attention must be focused on the *undeformed chip thickness $h_{cu}$*. It represents the base for predicting surface roughness, cutting power and wear. Its calculation is typically based on the representation of the removed material during grinding as a triangular shape with average height $h_{cu}$ (Figure 13) and can be derived from standard process parameters and surface morphology of the wheel, as follows in eq. (2):

$$h_{cu} = \sqrt{\frac{v_w}{v_s} \cdot \frac{1}{C \cdot r} \cdot (\frac{a_e}{d_e})^{\frac{1}{2}}} \quad (2)$$

Where $d_e$ is the equivalent wheel diameter, $C$ represents the grains density and so the number of abrasive grains actively involved in cutting at a given time present per unit area, finally, $r$ is the grain cutting edge shape factor ad it is represented by the ratio of the width to the depth of the groove produced from a single grain.
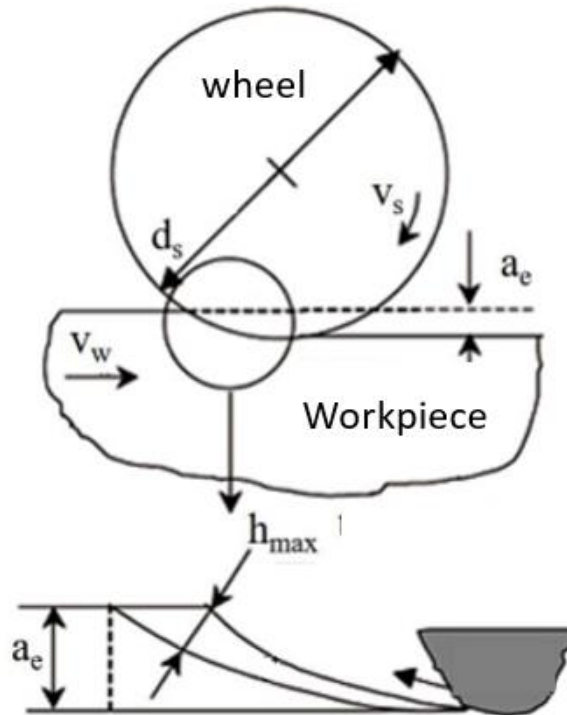


Figure 13. Undeformed chip thickness

The *equivalent wheel diameter* $d_e$ is a parameter that considers the conformity of the wheel and the workpiece in cylindrical grinding and gives the equivalent wheel diameter for the same contact length in a surface grinding application. It is expressed through eq. (3), where the plus sign is for es external cylindrical grinding, while the negative sign is for internal cylindrical grinding.

$$d_e = \frac{d_s \cdot d_w}{d_s \pm d_w} \quad (3)$$

where $d_s$ is the wheel diameter and $d_w$ is the workpiece diameter.

*Specific grinding energy* $e_c$ is the energy that must be expended to remove a unit volume of workpiece material. Its unit is usually J/mm$^3$ and it could be determined with eq. (4):

$$e_c \approx \frac{1}{h_{cu}^n} \approx \sqrt{\frac{v_s}{v_w} \cdot C \cdot r \cdot \sqrt{\frac{d_e}{a_e}}} \quad (4)$$

where n = 1 for precision grinding. Therefore, it is noticed that it takes more energy to make smaller chips, but this is valid only so long as chip formation is the dominant source. Indeed, being the chip formation mechanism not the only phenomenon that occurs during the material removal, the specific energy described in eq. (4) could be considered approximated.

*Specific removal rate Q'* is defined as the metal removal rate of the workpiece per unit width of wheel contact, as follows in eq. (5):

$$Q' = a_e \cdot v_w \quad (5)$$

For very low values of Q', rubbing and ploughing dominate, but as Q' increases, also the proportion of energy consumed in chip formation increases. Therefore, the energy consumed by rubbing and ploughing remains constant and become a smaller proportion of the total energy consumed as stock removal rates increase.

*Grinding power P* can be estimated from the specific grinding energy $e_c$ using the eq. (6):

$$P = e_c \cdot Q' \cdot b_w \quad (6)$$

Where $b_w$ is the wheel width.

The *tangential force Ft*, which has a tangential direction with respect to the circumference of the grinding wheel and coincides with the tool's rotational direction, and the *normal force Fn*, which is perpendicular to Ft and acts upwards from the grinding wheel inwards of the component, are the main forces acting at the grain-material contact point in the grinding process. Process parameters, kinematics, and the nature of the grinding wheel and component materials all influence force modules. Tangential and normal forces $F_t$ and $F_n$ are correlated by means of the *friction coefficient μ* through the eq. (7):

$$\mu = \frac{F_t}{F_n} \quad (7)$$

where the tangential force could be approximated through the eq. (8) starting from the grinding power P:

$$F_t = \frac{P}{v_s} = \frac{e_c Q' b_w}{v_s} \quad (8)$$

The value for μ can vary from as little as 0.2 for low stock removal applications for grinding hard steels and ceramics to as high as 0.8 in very high stock removal applications or grinding soft steels. In the case of tangential grinding, the graph in

Figure 14 reports the values of the friction coefficient μ in function of the hardness for different types of material.
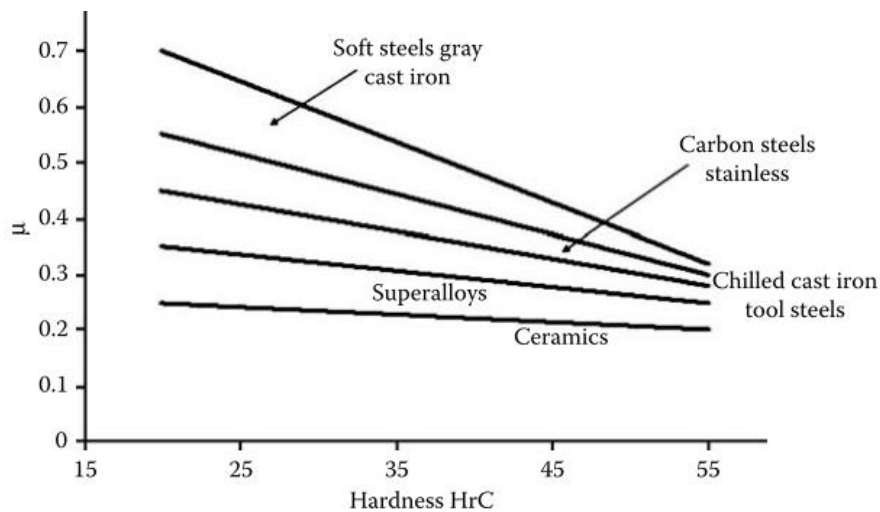


Figure 14. Friction coefficient trend for major material types in precision grinding.

Surface roughness could also be calculated using an analytical equation based on the thickness of the uncut chip. The largest difference between peak height and valley depth within the sampling length is represented by *theoretical roughness Rt*. Rt could be estimated as a first approximation using eq. (9), as follows:

$$R_t = \frac{h_{cu}^{4/3}}{a_e^{1/3}} \approx \left( \frac{v_w}{v_s} \cdot \frac{1}{C \cdot r \cdot \sqrt{d_e}} \right)^{2/3} \quad (9)$$

Surface roughness can be measured in a variety of ways, and Rt is just one of them. The *arithmetic roughness Ra*, which is the arithmetic average of maximum peak-to-valley measurements over five adjacent individual sampling lengths, and the *maximum roughness Rz*, which is the arithmetic average of maximum peak-to-valley measurements over five adjacent individual sampling lengths, are two other common roughness standards.

The *G-ratio*, which is defined as the ratio between the volume of material ground per unit wheel width and the volume of wheel worn per unit wheel width, is commonly used to identify wheel wear.


## 1.2.3. Grinding wheels


The tool used in a grinding process is a composite wheel made up of hard abrasive grains surrounded by a weaker bonding matrix. Depending on the bond type, the gap between the abrasives may be partially filled or completely filled with binder, therefore the principal elements of a grinding wheel are:

- Abrasive grains, that have the duty to effectively cut and remove the material and are defined by the material and the size;
- Binder, that maintains the grains linked to each other and is defined by the material and the hardness;
- Porosity, that represents the void among the grains and allow to dispose of the heat generated during the process.

In Figure 15 the standard marking system used for vitrified grinding wheels was reported. Grinding wheel specification is identified by using an alpha-numeric initials composed by means of six elements:

- Manufacturer's indication;

- Abrasive's material;

- Abrasive's size, represented by a number from 8 to 600 that increases when the grain size decreases;

- Grade, represented by a letter from A to Z, where Z is the highest value, and give an information about the hardness;

- Structure, represented by a number higher than 1 that increase with the porosity;

- Binder material.
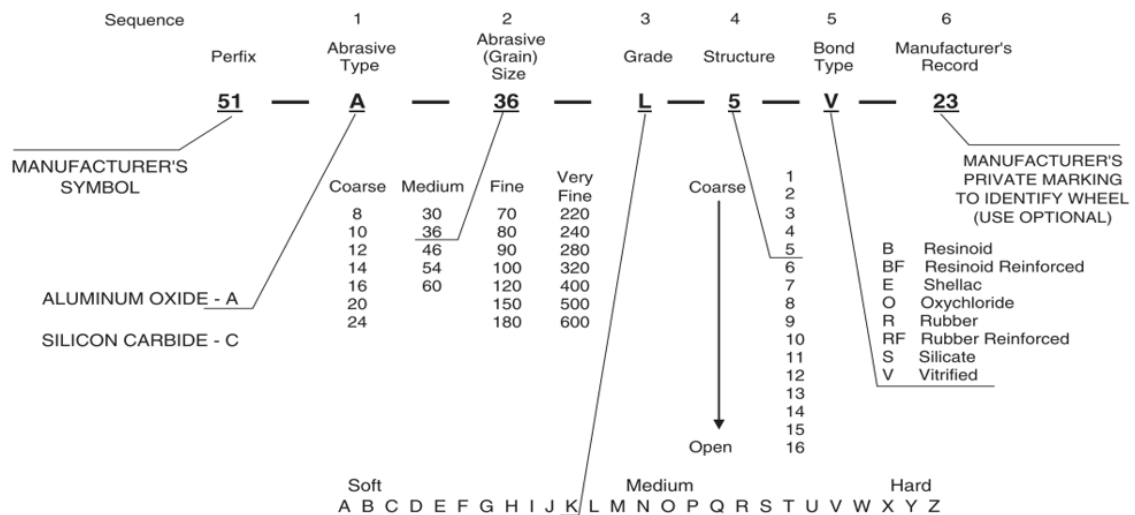


Figure 15. Standard marking system chart for grinding wheels

Abrasive materials include natural minerals and synthetic products. Abrasive grains can be considered as cutting tools with geometrically undefined cutting asperities that are characterized by high hardness, sharp edges and good cutting ability. The sharpness of abrasive grains may be mainly described in terms of edge radius and apex angle [39]. Industrial abrasives can be distinguished in conventional abrasives and super abrasives. Basically, super abrasives compared to conventional abrasives show higher hardness

values. Among conventional abrasives, silicon carbide (SiC) and aluminum oxide (alumina, Al2O3) are the most common. Instead, the super abrasives category includes diamond and cubic boron nitride (CBN). Generally, conventional wheels use vitrified or resinoid bonds. Super abrasive wheels could be produced with vitrified, resin, and metal bonds. Whereas conventional abrasive wheels usually comprise the entire bonded abrasive structure, instead, super abrasive wheels are limited to a thin layer on a metal hub to reduce the amount of costly diamond and CBN.

The principal requirement in the choice of the abrasive material is the hardness, but the decision to choose a specific abrasive is based on the workpiece material, wheel geometry and removal conditions. Silicon carbide and aluminium oxide are the less expensive and could be used in many applications. Alumina is used on most steels, but it is less efficient on nonferrous metals and non-metallic materials than SiC. Diamond is harder than CBN, and is very efficient for grinding carbides, but less efficient for grinding steels because of the chemical affinity of diamond with metals, which melts the abrasive and causes excessive wear. Diamond wheel are often used for the dressing tool manufacturing.

*Aluminium oxide abrasives*

Aluminium oxide is also known as Corundum and derives from raw bauxite. Aluminium oxide abrasives could be obtained by the traditional electrofusion route or by sintering and/or chemical precipitation. In function of the other materials traces, alumina could show different shades, for example, red with chromium, black with iron and blue with titanium. Concerning the electrofusion process, the bauxite, containing 85–90 % alumina, 2 – 5 % of $TiO_2$, up to 10 % iron oxide, silica, and basic oxides, is fused in an electric-arc furnace at 2,600 °C. A layer of bauxite crushed and calcined, mixed with coke and iron to remove impurities, is deposited at the bottom of the furnace and a carbon bar is put in contact to apply a heavy current. The bar is quickly consumed and the alumina is melt thanks to the heat generated. Thanks to the aluminium oxide low thermal conductivity, a wall of water running over the outside of the furnace shell is able to cool the system maintaining the shell integrity. After cooling, the alumina is broken up and passed through a series of hammer, roller, and/or ball mills to reduce it to the required grain size and shape. Downstream of the crushing process the product is sieved through

progressive metal sieves to form groups of decreasing grain size with size variability of less than 5% and up to 40 μm of minimum size. The granulometry is identified according to different scales that associate to each size a corresponding number. The most used is the FEPA scale (Federation European Abrasive Manufacturers) following ISO 6106-1979. Depending on additive materials, different alumina grains could be distinguished (Figure 16):

- brown alumina, which contains typically 3% of $TiO_2$, that has a Knoop hardness of 2090 and a medium friability, but increasing the $TiO_2$ content, toughness increases while hardness decreases.

- white alumina (pure more than 99%), that is produced by adopting low-soda Bayer process. It is characterized by very high hardness and friability and is used for manufacture wheels for the precision grinding.

- Pink alumina, produced by adding chromium oxide in quantity less than 5% to white alumina. The resulting grains are slightly harder than white alumina and are available in elongated form or sharp blocks of average size.

- Red alumina, produced with a percentage of chromium oxide equal to 3%. It is more friable compared to pink alumina. The grains are block-shaped with sharpen edges and it guarantee an excellent cold cutting effect.

- Green alumina, which presents similar properties and applications to those of the red alumina.

- Alumina-Zirconium, when zirconium dioxide is added to alumina to refine the structure of the grains and increase their toughness. These abrasives extremely tenacity and fine grain ensure excellent durability in applications with high removal of excess metal.
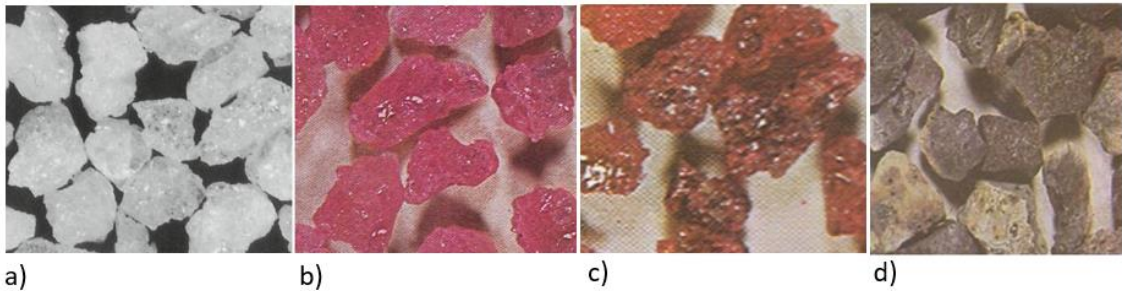


Figure 16. Alumina oxide abrasives: a) White, b) pink, c) red and d) zirconium alumina

The electrofusion process produces abrasives with very large crystalline structures and as a result, when a grain breaks during cutting, it lost a big portion of material leading to new sharp edges but quickly increasing the wheel wear. To improve the efficiency of the alumina grains, the sintering process was developed to drastically reduce the size of the crystals. In this way, when the grain breaks, it lost a minimum quantity of material reducing the wheel wear phenomenon. An example of the different structures of grains is shown in Figure 17.
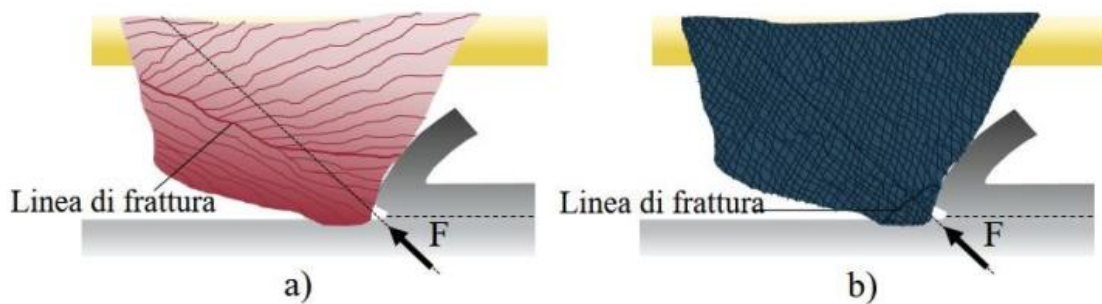


Figure 17. Alumina crystalline structure: a) fused alumina; b) sintered alumina

The first microcrystalline grains were produced in 1963 (Patent U.S. 3 079 243) compacting a mixture of bauxite previously reduced in very fine grain, then sintered at a temperature of 1500 ℃. With this innovation, the capacity of control the shape and proportions of the grains increases creating many different grains shaped characteristics. The most common abrasive grains of this type are those in blue alumina, also called blue corundum that, while maintaining a predominantly prismatic form similar to that of grains in molten alumina, have a better life thanks to micro-fracturing guaranteed by the very fine structure. The most significant development, however, was the release in 1986 of SG (seeded gel) abrasive (Figure 18) by means of chemical precipitation methods by the Norton Company (U.S. Patents 4,312,827 1982; 4,623,364 1986) [36]. This class of abrasives is often termed "ceramic" and comprises MgO precipitated to create 50 µm-sized alumina-magnesia spinel seed crystals. The resulting gel is dried, granulated to size, and sintered at 1,200°C. The resulting abrasive is unusually tough but self-sharpening because fracture now occurs at the micron level [39].
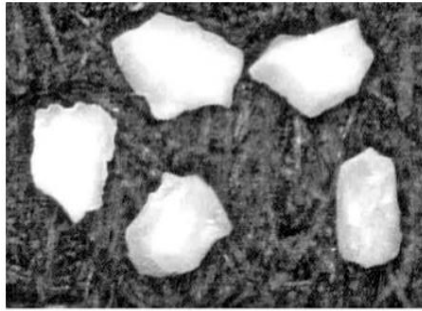
Figure 18. Examples of seeded gel abrasive grains [36]

## Silicon carbide abrasives

Silicon carbide (SiC), initially called carborundum, was discovered in 1891 by Acheson, who electrically heated a mixture of sand and coke and produced shiny black grains tough enough to scratch glass. The raw material includes sawdust to add porosity to help release CO, and salt to remove iron impurities. Silicon carbide has Knoop hardness values ranging between 2500 and 2800 and is very friable and compared to alumina has a much sharper shape (Figure 19). Above 750 ºC, SiC is chemical reactive with metals with carbon affinities such as iron and nickel. This limits its use for working on non-ferrous hard materials. It reacts with oxide of boron and sodium silicate, both common constituents of vitrified binder wheels.
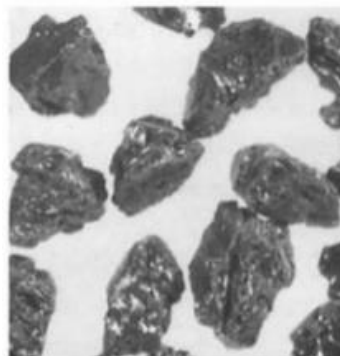


Figure 19. Silicon carbide abrasive grains

## Superabrasives

Diamond and cubic boron nitride are the hardest material present in nature (Figure 20). Diamond is used in both its natural and its synthetic forms, although synthetic diamond

dominates in wheel manufacture. Synthetic diamond is created by the application of extreme high temperatures and pressures to graphite. Depending on the processing parameters, diamonds are obtained with different crystal sizes and structures and are often used for dressing tool manufacture. Anyway, it cannot be used for grinding ferrous materials due to the graphitization and carbon diffusion into the material which could cause excessive diamond wear. Cubic Boron nitride, in both its cubic and its soft hexagonal forms, is a synthetic material and represents an alternative in grinding steels and some non-ferrous high-strength alloys. CBN compared to diamonds shows higher thermal stability. By contrast, diamond is thermally stable only to a much lower temperature of about 800 °C in normal atmosphere. Therefore, CBN wheels with vitrified bonds can be fired to a much higher temperature than diamond, and so a much wider range of vitreous bonds can be considered for their manufacture.
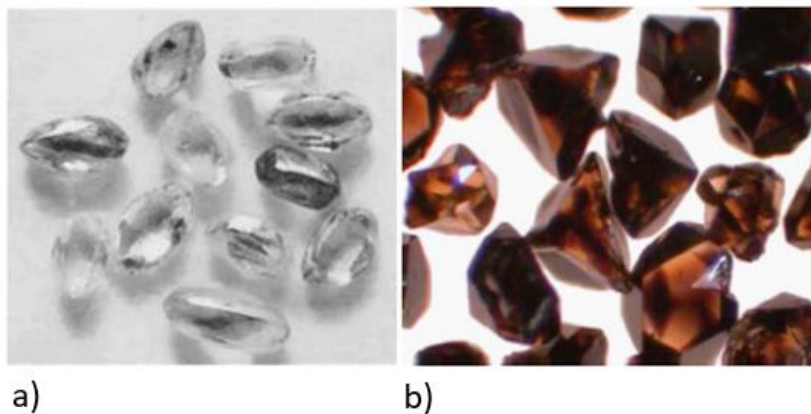


Figure 20. Super abrasives: a) diamond; b) CBN

Several methods are adopted for the characterization of abrasive grains and grinding wheels and consider the friability, the hardness and the wear of the grains [40]. In Table 1 some properties of the conventional and super abrasives were reported.

Table 1. Most common abrasive's properties [31]

| Material properties | Aluminum oxide ($Al_2O_3$) | Silicon carbide (SiC) | Cubic boron nitride (CBN) | Diamond (C) |
|---|---|---|---|---|
| Crystal structure | Hexagonal | Hexagonal | Cubic | Cubic |
| Density (g/cm$^3$) | 3.98 | 3.22 | 3.48 | 3.52 |
| Melting point (°C) | 2040 | ≈2830 | ≈3200 | ≈3700 |
| Knoop hardness (GPa) | 20.6 | 23.4 | 46.1 | 78.5 |

The bond has the duty to hold the abrasive grains all together avoiding their pull-out before they are worn out enough, therefore its main responsibility is to maintain a stable hold of grains allowing a controlled erosion of the wheel and leading to gradual exposure of the new cutting edges. Moreover, the bond must provide sufficient strength to transfer the forces from the spindle to the workpiece during the process and contribute to heat removal. Grinding wheel binder could be identified in function of the wheel types, therefore, it could be distinguished between those that are characterized by a single layer of abrasives reported on a solid steel support and those that provide a monolithic structure composed by many consumable abrasive grains layers that could be mounted on a resilient core. In function of the binder material another classification could be made. For conventional abrasive wheels, three general types of binder materials are used: resinoid, vitrified and metallic bond. Vitreous bonds and resin bonds are also employed for super abrasives but in these situations the bond requirements differ. In Table 2 the principal mechanical properties of the most common bonds were reported.

Table 2. Mechanical properties of most used bonds [39]

| Mechanical properties | Resin bond | Vitrified bond | Metallic bond |
|---|---|---|---|
| Brinell hardness (HB) | 228 | 380 | 278 |
| Rupture strength (psi) | 1,046 | 1,243 | 2,073 |
| Elastic modulus (psi) | 173,500 | 599,500 | 792,000 |

*Vitrified bonds*

Vitreous bonds are based on glasses materials and are produced by means of high temperature sintering of powdered glass frits, clays, and chemical fluxes such as feldspar and borax. Main characteristics are the high temperature stability, brittleness, rigidity, moreover, they can support high levels of porosity in the wheel structure. The mixture is blended with the abrasive and a binder, such as dextrin and water, and pressed in a mold usually at room temperatures. The binder gives sufficient strength for the melded body to be mechanically handled to a furnace where it is fired under a well-controlled temperature/time cycle in the range of 90°C– 1300°C. The pressing step in wheel manufacture is performed at a fixed pressure or a fixed volume, providing a controlled volume of porosity after firing. The compacting level obtained during the wheel manufacturing influence the wheel strength, indeed, in case the pressure applied does not reach a sufficient level, the abrasive grains are not in contact with each other and only the binder could provide support and give resistance to the whole by filling the spaces between the grains. These points become critical to the holding performance of the grinding wheel. Indeed, higher is the distance between the grains lower is the strength of the bond bridges. Therefore, the abrasive grains percentage is a critical factor in the grinding wheel design and it is identified with a specific number called Structure number. When the grain volume is defined, the remaining part is composed by the binder and the porosity. The bond bridges can become stronger by increasing the amount of binder to make them thicker. Another parameter that identifies a wheel is the grade, whose definition varies from supplier to supplier. In some cases, it is a direct correlation to porosity, in another cases, it is a more complicated combination of porosity % P and structure number. In addition to the size of the bond-bridge, the fracture mode is also critical. The bond must be strong enough to hold the grains under normal grinding conditions, but under higher stress it must allow the grains fracture in a controlled way. Moreover, the bond should not be so strong compared to the grit strength. In Figure 21, three different grain breaks were reported. The first case showed the pull-out mechanism that see the grain leaves the binder with all its material portion, in the second case, the grain breaks with a stable mechanism through micro-fractures, and finally, the third configuration showed the undesired glazing phenomena, where the binder is more strength than the grain that, although it is worn-out, it remains attached to the bond. The

first mechanism led to a premature wheel wear, instead the last one tends to produce grinding burns on the material, because the grain flat cutting edges are not sufficient for cutting. The stable breakdown allows to control the process ensuring a good cutting mechanism during all the process.

The tendency is to try to produce strength, but at the same time, porous grinding wheels. But, producing grinding wheels with a high structure number means obtaining the highest porosity possible maintaining the structural integrity, guaranteeing a better cooling and lubricant absorption by the grinding wheel. However, it is problematic to maintain resistance to wheel body during the grinding wheel manufacturing process, therefore, often the presence of additives is expected acting as structural supports in the formation of pores.
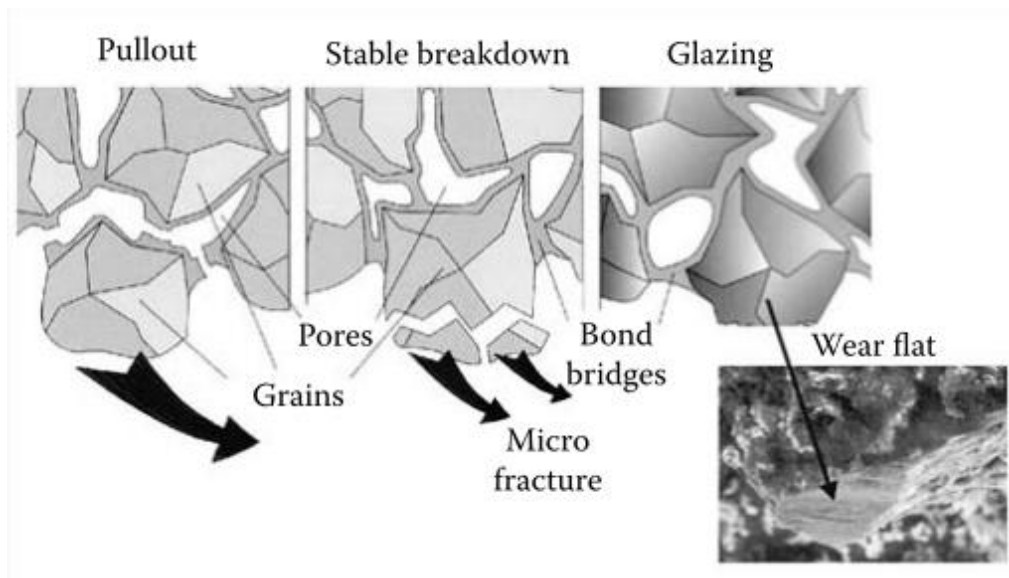


Figure 21. Pull-out, stable breakdown, and glazing regimes in grinding [36]

Typically, the additives used are alumina or glass particles that remain an integral part of the grinding wheel structure but, they break opening once in contact with the ground surface. Universal Grinding Wheel (Saint-Gobain Abrasives) introduced a further step in the evolution of wheel porosity structuring, creating the brand "Poros 2" that includes wheels with a double level of porosity, a macroscopic to ensure the permeability and a microscopic one to control the binder fracture (Figure 22).
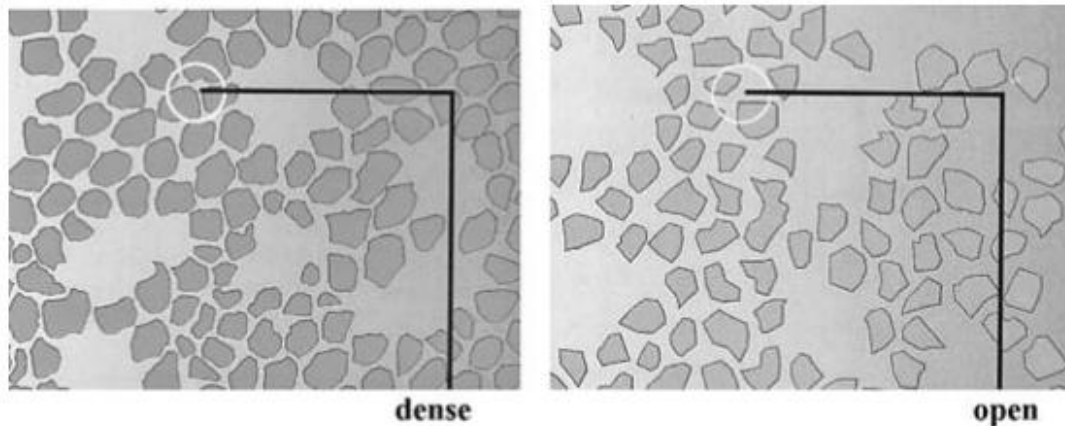
Figure 22. Comparison of regular induced porosity wheels and Poros 2 dual structure wheels [36]

## Resin bonds

Resin bonds are manufactured using organic bonds and are fabricated through hot pressing at relatively low temperatures. They are characterized by a soft nature of the cutting action and low temperature resistance. Grade and structure are defined in a different way compared to vitrified bond. Grain retention is dependent on the localized strength and bond resilience, moreover, it is influenced by localized temperatures and the chemical environment. Resin bonds can be classified in three classes based on strength/ temperature resistance and are plastic, phenolic resin, and polyamide resin.

## Metal bonds

Metal bonds are extensively used with super abrasive wheels. The most common derive from sintered bronze, which are produced by means of powder metallurgy methods. But other metal powder used are iron and nickel. The wheel grade depends on metal composition. Tungsten powder infiltrated with a low melting point alloy is used in diamond wheels for grinding diamond tools. A different type of metal bond for super abrasive wheels is manufactured by electroplating. These grinding wheels consist of a single layer of diamond or CBN held in place on a form or hub by an electroplated nickel binder [36]. Since the reduction of the environmental pollution generated by the massive

use of lubricants is one of the key points for industry to evolve within a green and eco-friendly vision of the production, the future trend related to the grinding wheel manufacturing also aims to the minimum fluid applications. Therefore, many efforts have been dedicated to the research based on the reduction or the elimination of lubes. Examples are the super abrasive wheels impregnated with resin and proprietary solid lubricant, Sol-gel alumina grain in vitrified bond, filled with oil/wax mixture and vitrified aluminium oxide wheels impregnated with water-insoluble, sulphur bearing, organic substance [41].

## *Dressing*

The dressing process is an essential operation applied to the grinding wheels. With dressing, the profiling and the sharpening processes are included. Indeed, grinding wheels before grinding process needs to be profiled and dressed often. The first process allows to obtain the macro-geometrical shape of the wheel that is reproduced on the component and guarantees the workpiece accuracy surface [42]. Instead, the second one has the duty to sharpen the wheel from time to time in series production. The sharpening process removes part of the binder around the grains to enhance the cutting properties of the abrasives. Dressing process, especially in the case of ceramic or resin bond grinding wheels can be performed using various types of diamond tools, such as single and multigrain stationary dressers and rotating dressers. Also, during dressing, a significant amount of heat is generated. In this case, the main problematic is correlated to the diamond oxidation and graphitization processes causing its mechanical damage due to thermal fatigue or decreasing hardness [43]. Dressing has an essential influence on the grinding process and the flank topography of gear teeth [44]. During the dressing of conventional wheels with a single-point diamond tool, the dresser moves across the wheel surface with a defined feed rate and depth of cut following a path represented by a thread with a pitch equal to the feed rate. But, the removal mechanism on the grinding wheel by means of the dressing tool does not follow the theoretical cutting path (Figure 23). Indeed, the abrasive particles removed by dressing appear to be produced mainly by brittle fracture [31].
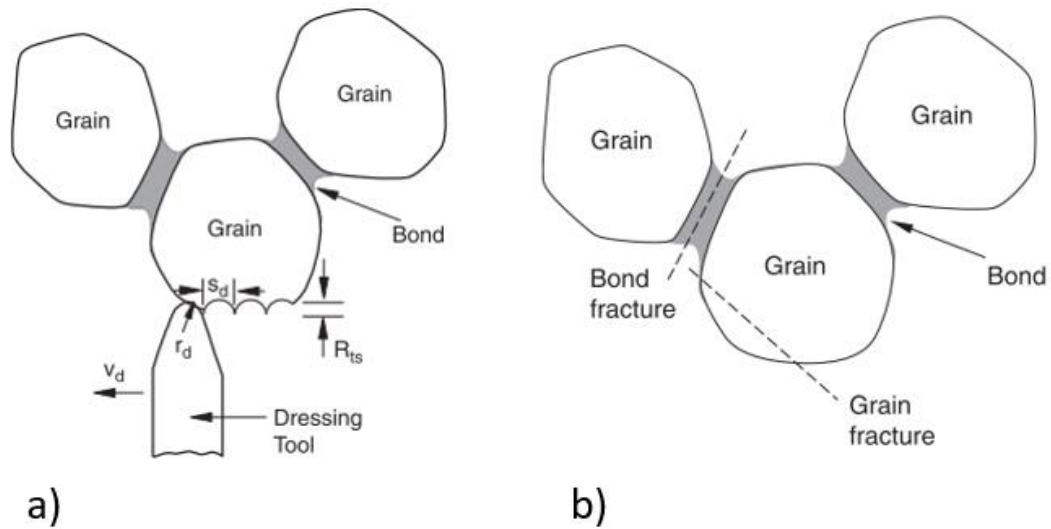
Figure 23. Dressing of conventional wheels: a) theoretical cutting path of a single-point diamond dressing tool through an abrasive grain; b) actual grain and bond fracture [31]

In the gears grinding processes that use worm generating wheels, the final gear tooth shape is obtained thanks to the combination of the grinding process kinematics and the wheel profile shape. The grinding wheel is machined to obtain on its surface a helix, whose profile represents the space between two consecutive gear teeth. To obtain the characteristic shape of the screw cylindrical wheels, they are roughened through turning operations that realize the raw thread, then the grinding wheel is profiled and sharpened to achieve the correct shape and cutting ability. Being the dressing time a down time that influences the production costs and efficiency, it needs to be faster as possible. For this reason, in general, the worm generating grinding wheel dressing is performed by means of a profiling roller, consisting of a disc having section corresponding to the tooth of the gear to be ground. The ratio between roller and grinding wheel speeds represents the profiling rate and it is the parameter that most influences the action of the grinding wheel dressing. But, as the profiling ratio increases also the profiling forces increase causing a raise of the roll wear. The wheel dressing could enhance the wheel porosity, in particular, higher profiling speeds increase the effect of macroscopic wheel fractures by opening the structure of the grinding wheel, instead, with lower profiling speeds, the grinding wheel seems to become less porous due to the main wear effect of the grains due to friction. In Figure 24 an example of dressing tool is shown.

Figure 24. a) dressing tool; b) dressing of a grinding worm with combined tool [23]

## 1.2.4. Grinding lubricants

Lubricants use and selection is essential to cover two main roles. Type, base oil, additives, and concentration of the fluid are all important for the efficiency of cooling and lubrication. Other requirements of a grinding fluid are flushing performance and high corrosion protection. In grinding processes, temperature generation in the contact zone depends on the tribological interaction between the grain cutting edge, the grinding wheel bonding, the workpiece and the chip as it forms, so that cooling lubrication plays a decisive role during grinding with respect to heat generation and dissipation [17]. Indeed, the thermal effect of the process on the material can be evaluated to describe the efficiency of fluid supply which strongly depends on various parameters such as the jet velocity, the jet shape caused by the fluid supply nozzle, and the nozzle position [45]. Grinding fluids are commercially available with different properties to meet the requirements of specific machining tasks and they could be classified in:

- Water-immiscible, that are generally not mixed with water for any application [DIN 51 385];
- Water-miscible, that are emulsifiable, emulsifying, or water-soluble concentrates, to which water is added before use;

- Water composite fluid, that are ready-for-use composites of water-miscible cooling lubricants with water.

For cutting, mainly oil-in-water emulsions and solutions are used, whereas water-in-oil emulsions are less common. Water-immiscible lubricants are usually referred as mineral oils and are obtained by distillation of petroleum. In the pure state, they do not have particular active properties, therefore they are mainly used as support to other lubricants or are mixed with appropriate additives that have the task of improving the lubricating power to increase the wear resistance of the tool and to improve its resistance to the shear pressures (in particular EP additives). The additives can be based on sulphur, chlorine or phosphorus promoting the formation of compounds with the metal, such as sulphurised, chlorinated or phosphoric, that mediate the friction between the piece and the tool. But most of the coolants used is miscible with water. These fluids combine the high-water capacity of heat dispersion to the lubricating power of the dissolved chemical substances. The water-soluble coolants include emulsifiable oils, which are dissolved in water in a proportion of about 1:10. These fluids have large cooling capacities and therefore allow high cutting speeds. In addition to the coolants described above, it is also possible to use gaseous fluids such as compressed air, argon, helium or nitrogen (for special applications) and carbon dioxide.

Therefore, the benefits of cutting fluid are multiple because they reduce thermal effect of the process, maximize the life of the tool and improve the operation accuracy reducing the consumption of power [46]. But other approaches, such as mist cooling, high pressure system, cryogenic machining and minimum quantity lubricant (MQL) techniques were experimented and analysed [47]. The latter implies the use of a small amount of fluid in the tool-workpiece area by means of a compressed air jet, which, thanks to the high pressure and speed, is able to penetrate the air flow reaching the working area and creating a lubricating film. The MQL technique was considered as a suitable technique for replacing the conventional wet method, thanks to its benefits of reduced but efficient lubrication and low implementation costs. But, among all the alternatives, dry machining would be the ideal technique, due to the total absence of cutting fluids [48].

## 1.2.5. Grinding thermal defects

Recently, the reduction of coolant flow rate or even dry-machining has been taken in consideration as an alternative to conventional finishing process [17]. In general, machining, and even more, finishing processes remove material generate a huge amount of heat that in part is absorbed by the workpiece. For this reason, lubricants are usually abundantly adopted in cutting operations with the aim at removing part of the heat generated and absorbed by the wheel. Therefore, it is natural to think that the complete elimination of lubricant in a grinding process becomes difficult to manage due to the substantial thermal effect. The mechanical energy produced by grinding is due to the relative movement between the tool and the workpiece (Figure 25). This energy is mainly transformed into heat through friction and deformation processes, leading to temperature increase in the contact zone [36]. In general, the heat produced during a material removal process is dispersed in four main elements: the workpiece, the tool, the chip and in the lubricant. In grinding, a minimum part of the heat is absorbed by the grinding wheel and the chip. Indeed, the wheel usually has a very low thermal conductivity and the chip is characterized by a negligible thickness.
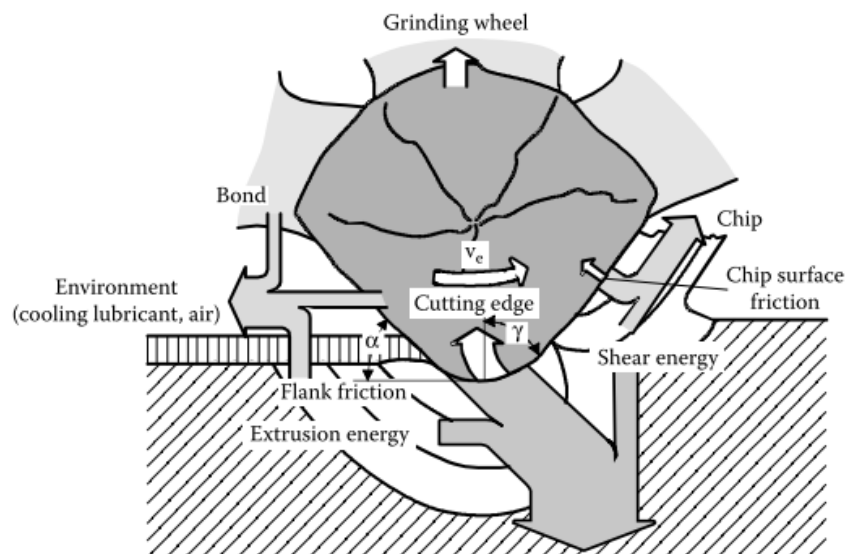


Figure 25. Heat flow during the grinding of metallic materials [36]

Therefore, during a grinding process, the main portion of the heat is absorbed by the workpiece. During the material removal mechanism, the first two deformation phases, rubbing and ploughing, release the main part of the heat compared to the cutting phase, due to the friction within a relatively short time, in a region of a few square millimetres. The resulting high temperatures could lead to thermal fatigue, phase transformation, recrystallisation and microhardness variation and these phenomena must be taken under control especially in the gear production, and in general in machining of hardened steel components, wherein the heat generation and technical responsibility of the component are normally high [49]. The thermal cycle induced by the grinding process generates thermal expansion due to the temperature gradient between the rapidly heated surface and colder sub-surface layers leading to tensile residual stresses. Other typical surface alterations were identified as micro-cracking, tears and laps related to built-up edge formation. Therefore, if excessive heat is generated in the workpiece, it may be damaged as thermal overloading leads to microstructural changes and degradation of surface integrity. The surface integrity is defined as the sum of all the elements that describe the conditions existing on a material surface finished by means of a surface process [50]. Grinding, as well as machining processes, includes different physical mechanisms in the material action. Indeed, the workpiece is exposed to a mechanical, thermal and chemical loading. In some cases, the material could be suffer the combined effect of these mechanisms, which contribute to the surface formation and influence the surface integrity of the component [51]. In grinding, the surface integrity, resulting from the process, depends on the combination of a mechanical and thermal loads. This undesired overloading effect represents the basic limitation for further development of high performance grinding [52]. Modified layers are often observed on the ground surfaces which could show a top layer, called white layer, generally associated to re-hardening phenomena and severe damage such as cracks, and a subsurface layer, called dark layer, which is assimilated to a softening effect because it occurs at lower temperatures [53]. Microstructural transformations must be avoided to preserve the mechanical performance of the components, especially in gears because such defects could cause local changes in gear flanks hardness and residual stresses and may eventually lead to transmission wear, vibration and noise. Surface features generated by the manufacturing processes [54], together with the applied loading stress, contributes to gear fatigue behaviour, which

represents a continous damaging process that could lead to the definitive material failure [55]. Figure 26 shows the microstructure of a tempering steel at the unaltered core and at the surface after grinding [56].
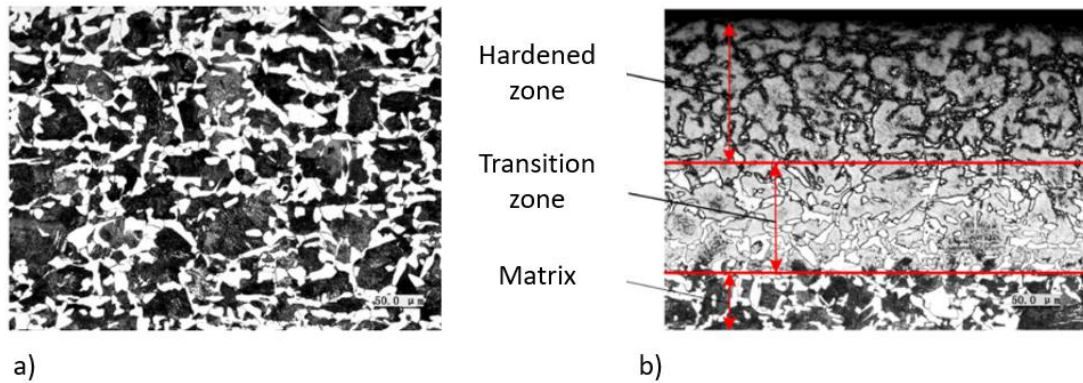


Figure 26. Workpiece microstructure composition and distribution: a) before grinding; b) after grinding

It can be noticed that the surface configuration was significantly changed after the grinding process compared to the core, and so the starting morphology. The surface shows three different zones: a completely hardened zone, the transition zone, and the unaltered core. The hardened zone presents martensite formation because the material during grinding exceeds the $A_3$ temperature and it is quickly cooled. The transition zone is characterized by martensite and tempered sorbite because in that zone the temperature during grinding reaches a value between $A_1$ to $A_3$ (Fe-C diagram in Figure 27). Low and normal heating rates are between 1 °C/s and 20 °C/s, high heating rates are between 20 °C/s and 100 °C/s and ultra-fast heating rates are above 100 °C/s [57]. The grinding technology could be identified as a fast-heating process. For processes that deviates from the thermodynamic equilibrium, the critical temperatures are not uniquely defined and depend on multiple factors including heating rate, cooling rate, and prior microstructure [58]. The hypoeutectoid steel critical temperature as a first attempt could be considered as the starting austenitization temperature $A_1$ (727 °C), but it was demonstrated that in the fast and ultra-fast heating processes the critical temperature could slightly change, as reported in [59].
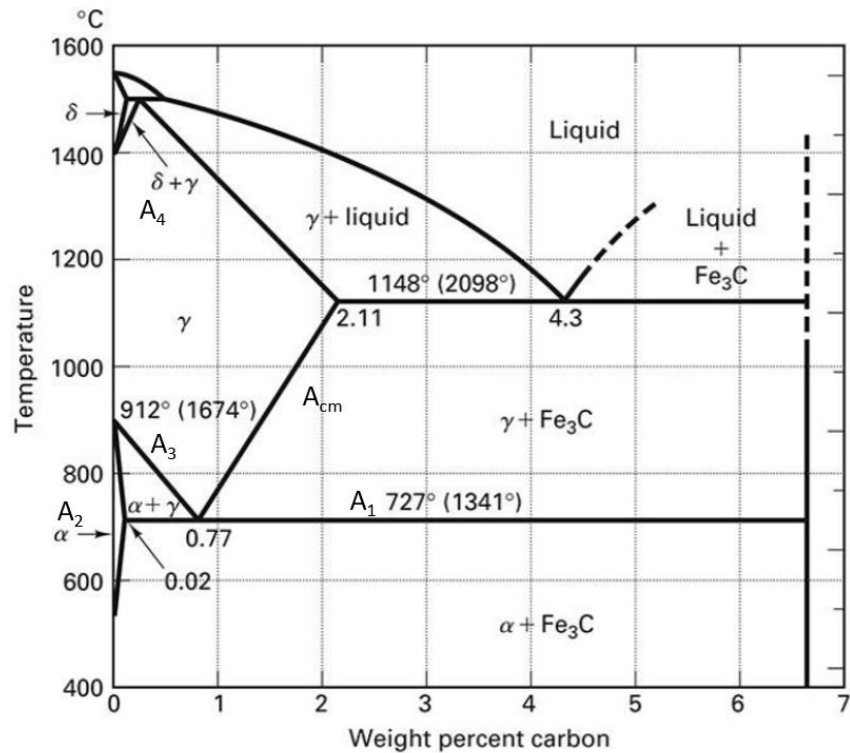
Figure 27. Fe-C diagram

In general, materials adopted for gear production are cemented or nitrided steels, such as 27MnCr5 or 18NiCrMo5 after heat treatment. For these material the grinding burns are classified in three different levels [60]. Up to a temperature of 400-450°C the material surface could be affected by oxidation and the microstructural analysis shows a slightly blue surface layer. This type of defect is not considered dangerous. Increasing the temperature, the surface shows a darkened layer caused by the softening of the martensite due to the carbon separation from the solution. The elongated grains typical of the martensitic structure transformed into spherical and small size ones. A decrease in the mechanical properties usually appears. With a further increase in process temperatures, the steel could reach and overcomes the austenitization temperature causing severe thermal damage. A white layer is formed and usually shows an increase in the surface hardness with the formation of very small and deformed grains difficult to identify through microstructural analysis. In general, when a grinding burn appears, an increase in the surface hardness is followed by a decrease of it in the sublayer, where temperatures reached are lower and a softening effect is visible (Figure 28). But, this phenomenon

depends also on the workpiece mass, which acts as self-cooling system and affects the thermal defect depth thickness.
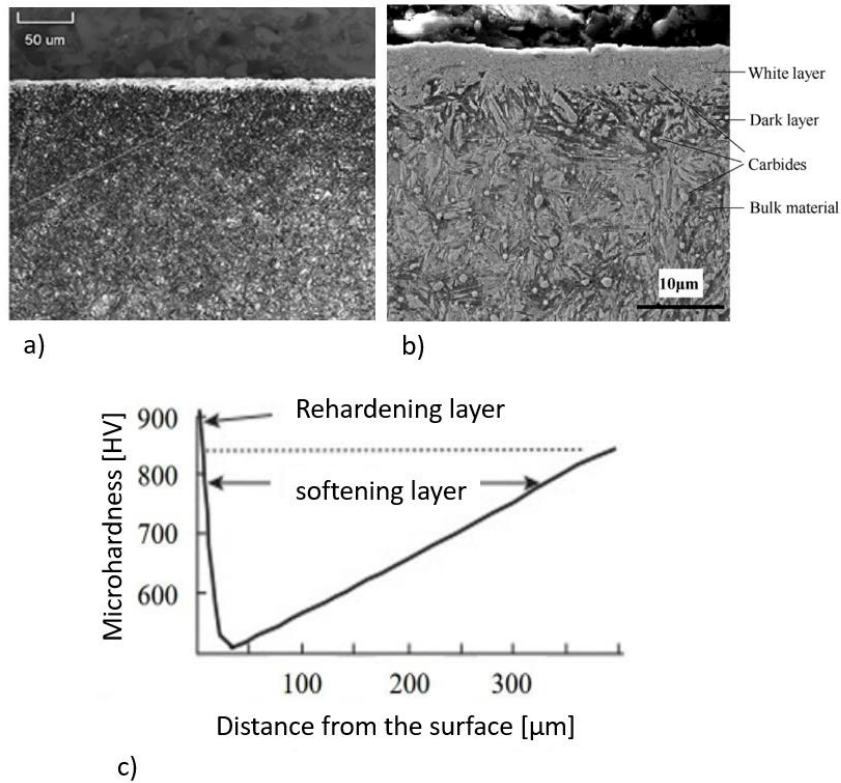


Figure 28. a) Characteristic grinding burn microstructure b) Characteristic grinding burn microstructure SEM magnification; c) Surface hardness trend variation

The extreme consequence of the grinding burn is represented by the possible occurrence of cracks of the surface component after production or in service with deleterious effects. The pitting is a common wear mechanism on gears and it starts with short cracks on the tooth's flank surface and tend to increase the existing cracks [61]. It leads to macro-pitting, spalling, and even tooth fracture failure, which cause destructive damage to gearboxes [62]. Therefore, it must be avoided starting from the manufacturing finishing processes optimization, since it may cause fatigue cracks initiating from the surface or nearby subsurface [63].

# Chapter 2

# Grinding process modelling and thermal defect prediction

Heat-related problems can be managed following two different approaches: post-mortem detection and beforehand prediction methods [64]. As can be guessed, post-mortem methods imply a destructive or non-destructive control on the ground piece that becomes waste if burn appears. This kind of approach generally can identify with high certainty the grinding burns already occurred, but they cannot avoid burns and cannot always be applied, especially on expensive components if a destructive approach is chosen. Instead, the beforehand prediction methods have the possibility to forecast grinding defects before they occur preserving the component integrity, but they need more efforts to be optimized.

Post-mortem methods can distinguish defects on components by inspecting hardness change and surface microstructure, which were induced by the process through various physical and chemical effect. The most common post-mortem controls can be summarized in the following points:

- acid corrosion inspection;
- metallographic testing;
- surface micro-hardness testing;
- residual stress testing;
- chemical composition analysis;
- eddy current testing;
- magnetoelastic methods;
- acoustic emission monitoring;

Considering the acid corrosion inspection and the metallographic testing, they are based on a qualitative inspection of the ground surface by considering the change in colours and microstructures. The ISO 14104 [65] regulates the application of chemical etching for the detection and classification of thermal defects on ground surfaces for standard steel components such as gears. Indeed, a steel sample could present variations in colours on the ground surface when a Nital solution is applied, and this could be considered a first

visual inspection able to detect further burns. Also, metallographic testing methods qualitatively reveal the occurrence of grinding defects, but they analyse alterations in the metallographic structure using optical or electron microscopy and this could be considered a more efficient and univocal way to detect grinding burns [66]–[68]. Even more reliable is the surface micro-hardness testing, which can give a quantitative measure of the thermal defect induced by grinding because it can measure the surface micro-hardness variations due to the thermal cycle. The reduction or the increase in hardness is proportional to the burn entity. Therefore, the grinding burn severity can be evaluated by comparing micro-hardness measurements before and after grinding [69]–[71]. The thermal effect of grinding is a change in microstructures and consequently in the residual stresses, which can be considered an appropriate measure of the degree and the extent of the grinding burn [72]–[74]. This kind of grinding defects approach has the advantages of high accuracy, but it is also an expensive and complicated operation. Also, the chemical composition of a thermally affected surface layer is a direct expression of the degree of grinding burn suffered by a workpiece. It is noticeable that the percentages of nickel, iron, chromium and titanium in the burnt surface decreased significantly due to compounds formation and this represents a clear indication of the grinding burns occurrence. The accuracy of this approach is high, however, complex equipment makes it more suitable for laboratory research [75], [76]. The magnetic permeability and the electrical conductivity of a conductive material are affected by microstructural and stress state changes, therefore eddy current testing is a useful grinding detection testing method. But it is sensitive to edges effect caused by geometrical shapes, therefore it is not a reliable approach for complex parts such as gear teeth. Magnetoelastic methods refer to magnetic Barkhausen noise (MBN) analysis which represents a reliable potential non-destructive evaluation method for characterization of microstructures and assessment of residual stresses in ferromagnetic steels. It is based on the analysis of the magnetic signal that induces voltage pulses in the pick-up coil placed near the surface in function of the microstructural obstacles found. Indeed, the softening of a hardened microstructure with precipitation of carbides is found to increase the signal amplitude due to easier and larger displacement of magnetic domain walls [77]–[79]. Acoustic emission analysis approach as grinding burn detection methods implies installation of sensors and could be identified as useful methods through a calibration phase by comparing the signal before and after

the burn occurrence. The acoustic emission phenomenon is related to the elastic energy release at a very high frequency range during the material removal mechanism where the thermal expansion accompanied by grinding burn influences the acoustic waves [80], [81].

Even though the before mentioned grinding burns detection methods could represent a very useful approach to investigate and identify grinding parameters that easily lead to grinding burns, more interesting and challenging from the scientific and also industrial point of view is the possibility to predict the thermal defect before its occurrence and avoid waste in the production line. For this reason, many efforts have been focused on grinding predicting models. They are mainly concentrated on forces and temperature considered to give a threshold value below which the process could be performed with the nominal operating values without generate thermal defects. Different approaches can be identified. Each of them requires previous knowledge of the phenomenon and implies some difficulties and limits in its application. Many researchers dealt with this challenge using different modelling approaches. Models employed until now can be classified in the following classes:

- Empirical models;
- Physical models.

Empirical models focused on the macroscopic behaviour of the grinding system and are mainly implemented to control the process [82]. Instead, Physical models are based on microscopic phenomena and generally are developed to design the process preventing manufacturing defects. They require previous knowledge for the results analysis and high computational time, but they allow to recognize microscopic phenomena below the process. This section mentions the principal grinding modelling approaches found in literature.

## 2.1. Empirical models

An empirical model is based on recording measured values obtained in grinding tests. In general, grinding tests are performed and all the parameters and outcomes are

registered. The results of these tests are evaluated by choosing a model procedure and by determining the coefficients to verify it in further grinding tests [83]. Therefore, empirical and semi-empirical models were widely used as useful indication for the process application, but they usually work only for a specific parameters and materials set, so they need that several experimental tests have to be performed to introduce calibration coefficients often difficult to obtain. Since the model parameters are often determined with the aid of regression analysis methods on the basis of numerous measured values, every empirical model can be used for the description of one process application only [84]–[86].

## 2.2. Artificial Neural Net models

Grinding processes sometimes involve a large gap between the process applications and human understanding, so finishing processes are often investigated through machine learning (ML) techniques [87]. The application of this kind of techniques imply that modelling is accompanied by process on-line monitoring through sensors capable to consistently catch the physical phenomena occurring. With the rapid development of intelligent manufacturing technology, a huge amount of real-time data and historical data will be generated during the grinding process [88]. Currently, neural network architecture has become even more influencing as an effective technique in pattern recognition because neural networks have strong abilities to acquire and organize information. Moreover, it is an approach that needs few specific requirements and prior assumptions for modelling [89]. But to date, there still are some key technologies to be improved and difficulty of data unification and collection in grinding with lack of advanced integrated multi-sensor online monitoring equipment still limit the ML application in grinding. Moreover, restricted data volume does not allow yet a substantial improvement in this technique, indeed often experimental data are combined with simulation ones to increase the dataset and allows better prediction [90]. Grinding process analysed by means of ANN models becomes even more an efficient alternative in the process modelling, but to date many efforts need to be done to collect and store experimental data. Moreover, this kind of approach finds more possibilities in control of the process rather than the process design.

## 2.3. Analytical and numerical models

A physical analytical model is based on the application of physical principles derived from the analysis of the process phenomena. Therefore, a physical model works in function of the conformity to physical laws, using mathematical formulation of the qualitative model. In literature, analytical approaches can be distinguished in function of the analysed outcomes. Basically, the scope could be represented by calculating the grinding forces and/or the grinding temperature. Indeed, the models can focus on the micro-scale or the macro-scale grinding phenomena. Micro-scale models study the material removal mechanism from a microscopic point of view including all the cutting data information, instead, the macro-scale models focused on the macroscopic effect of the grinding process that involves the thermal phenomena.

Many researchers dealt with the study and the investigation on the microscopic aspect of the grinding. Tohnshoff et al. are the authors of a thorough work that explore and describe the main models developed up to 1992 by comparing them based on the analysis of wheel topography, chip formation, forces and surface integrity [83]. Subsequently, a comparison of two numerical models to predict the grinding forces was studied by Badger et al. starting from the wheel surface topography approximation based on a 2D and 3D approaches [91]. Hecker et al. focused on the prediction of forces and power modelling by developing an analytical and statistical observation on the chip thickness distribution [92]. Also Wang et al. consider the statistical chip thickness occurrence due to the random grit distribution by calculating the force generated by the grinding process as the overlapping of individual grain forces through the use of a grit density function [93]. Park et al., instead, presented a physics-based model considering the mechanical and thermal interaction between the material and a single grit introducing the size effect, which implies an increase of the specific energy during the process due to the decrease of the uncut chip thickness [94]. Tang et al. proposed a formula for the calculation of the chip formation force by analysing the static and dynamic chip formation energy [95]. Also Ghosh et al. analyse the microscopic aspect of the material removal mechanism in grinding by conducting single grit scratch tests and studying the actual dynamic behaviour of grinding process at single grit level [96]. They assume that the specific grinding energy

could be identified through four different contributions: the chip formation, primary rubbing energy due to rubbing between grain tip and the material, secondary rubbing energy due to rubbing along the cutting edge towards the cutting path and the ploughing energy due to the deformation induced by the negative rake angle of the abrasives (Figure 29). Wang et al. also investigated the cutting mechanism during grinding by considering a random grinding wheel topography made of conical abrasives and calculating the single grain grinding force per superposition effect [97].
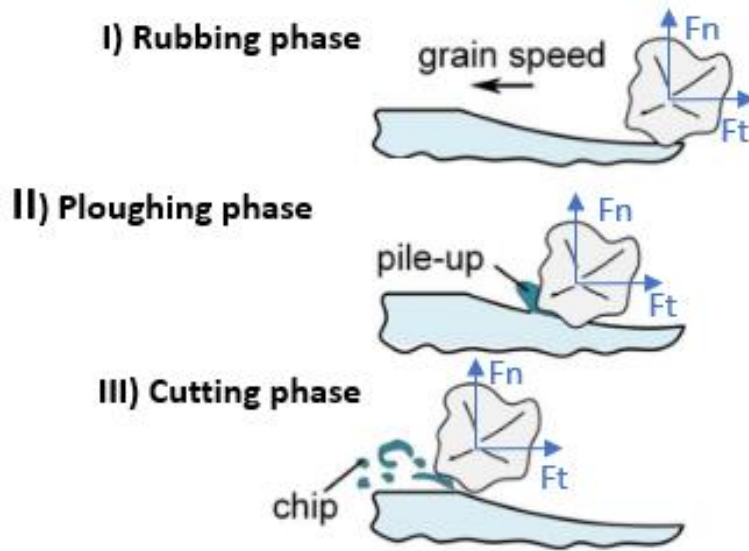


Figure 29. Forces modelling in the three stages of the grinding mechanism

Zhang et al. predicted the grinding forces through a model based on the material-removal and plastic-stacking mechanism estimating the active dynamic grains number [98], [99]. Linke et al. analyzed both macroscopic and microscopic aspect of grinding process considering either the whole grinding tool and the single cutting edge. They proposed a model capable to predict the process energy by comparing the spindle power used during the process with the energy generated during the cutting action of a single grit, being realistic the assumption that all the mechanical energy is transformed in heat in grinding [100]. This concept underlies the main analytical and numerical thermal models that consider the thermal power generated during the process to estimate the temperature field on the ground material.

Considering the macroscopic approach, main thermal analytical approaches are based on Malkin's model [101]–[105] which focused on the evaluation of the temperature reached during the grinding pass by comparing it with the critical temperature of the material. Grinding temperature depends on heat flux calculation, function of the power process, that is experimentally measured during the test, and partition ratio that represents the heat absorbed effectively by the workpiece, which generally needs to be calibrated. It is assumed that the responsible for further thermal damage is the temperature associated with the continous heating of the grinding zone, also called the "background temperature", because the peak flash temperatures, which approach the melting point of the material, occur in an extremely short duration and are highly localized. The interaction between the grinding wheel and the material could be represented by a moving heat source that could be uniformely distributed on the workpiece surface and depends on the grinding process parameters, as shown in Figure 30.
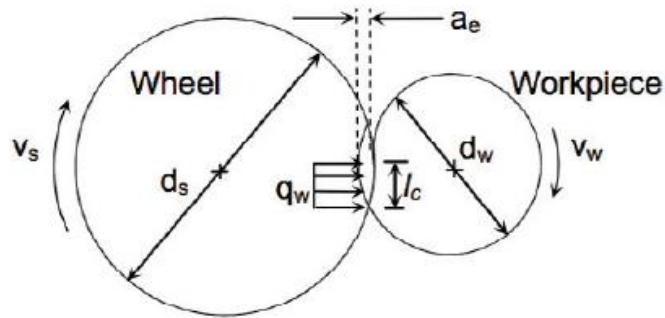


Figure 30. External cylindrical plunge grinding moving source [101]

Therefore, to calculate the temperature reached during the process, it was considered that the grinding energy generated by the grinding process is dissipated through the contact area between the heat source and the workpiece. If the heat source is moving with a sufficiently high speed so that heat conduction into the workpiece is higher than the heat source speed, the maximum temperature rise $\theta_m$ is calculated as:

$$\theta_m = \frac{1.13\, q_w \alpha^{1/2} a_e^{1/4} d_e^{1/4}}{k\, v_w^{1/2}} \quad (9)$$

Where $\alpha$ is the thermal diffusivity, $k$ is the workpiece thermal conductivity, $a_e$ is the depth of cut, $v_w$ is the workpiece speed and $d_e$ is the equivalent diameter calculated as:

$$d_e = \frac{d_w d_s}{d_w \pm d_s} \quad (10)$$

Where $d_s$ is the wheel diameter and $d_w$ is the workpiece diameter.

The heat flux $q_w$ could be determined through the specific grinding energy $u$ or the grinding power $P$ as:

$$q_w = \frac{\varepsilon u v_w a_e b}{l_c b} = \frac{\varepsilon P}{l_c b} \quad (11)$$

Where $b$ is the width and $l_c$ is the arc length of contact between the grinding wheel and the workpiece and is determined as:

$$l_c = (a d_e)^{1/2} \quad (12)$$

The grinding power P could be estimated starting from the tangential grinding forces $F_t$. It represents the main contribution in calculating the heat flux and it usually need to be measured experimentally or analytically approximated as follows:

$$P = F_t v_s \quad (13)$$

Where $v_s$ is the wheel cutting speed. Instead, the energy partition ratio $\varepsilon$ represents the proportion of heat absorbed by the workpiece. It could be approximated as:

$$\varepsilon = (1 + \frac{k_g}{\beta_w \sqrt{r_o v_s}})^{-1} \quad (14)$$

where $k_g$ is the grain thermal conductivity, $r_o$ is the grain contact radius and $\beta_w$ is the transient thermal property and is given by:

$$\beta_w = \sqrt{k \rho c} \quad (15)$$

Where $\rho$ is the workpiece density and c the heat capacity.

But, in general, the partition ratio is derived from a calibration process using temperature matching or inverse heat transfer methods, but greater difficulties are found in obtaining its real value for any application. The temperature matching method is based on calibrating the model by comparing the calculated and the measured temperature. With the inverse heat transfer method, the heat flux to the workpiece surface is calculated from the measured temperature distribution within the workpiece. The surface temperature is usually measured by means of embedded thermocouples or infrared detector with an

optical fiber. Therefore, the model could predict the grinding temperature rise in the working zone and compare it with the critical temperature of the material. Analytical approach represents an important analysis approach of the grinding phenomena as first attempt, because it represents an approximation of the phenomena. But due to the non-deterministic nature of grinding they need to evolve. Moreover, analytical approaches based on temperature prediction generally need to perform experimental tests to measure the grinding forces and power and often in an industrial environment this phase need to be avoid reducing the production time.

## 2.4. Molecular/Smooth Particle Hydrodynamics (SPH) models

To study deeply the microscopic aspect of the grinding material removal mechanism, molecular dynamics and Smooth Particle Hydrodynamics (SPH) models have been developed in recent years. This kind of approach can consider microstructure, chemical elements and atomic interaction giving a more realistic representation of the material and its surface state. Wegener deeply investigated the possibility to simulate the grinding process through an SPH approach. He modelled the interaction of a single grain with a meshless workpiece to calculate the grinding force generated using an engineered grinding tool [106], [107]. The model was able to also analyse the stagnant zones that formed during the grinding pass represented by a zone with an increase in the equivalent plastic strain due to the long duration of compressive stress. Shen et al. developed a multiple-grain cutting model using a combined 3D FE model and a SPH approach to investigate the interaction between the material and the grains under high speed regime [108]. Julean presented a study focusing on the chip formation under the action of a single grain simulating it as an inclined linear scratching of a cuboid part [109]. Papanikolaou et al. presented a thorough work based on simulating the grinding microscopic aspect by means of SPH approach considering the contact stiffness effect due to the bond grinding wheel and the real depth of cut [110]. This approach could explore in deep the material removal mechanism in grinding, but it needs huge computational resources and to date, it finds many difficulties to be easily used yet.

## 2.6. Kinematic geometrical models

The kinematic geometrical approach is based on the geometrical analysis of the workpiece surfaces by calculating the roughness and the chip thickness. The engagement between the grains and the workpiece surface before and after grinding is calculated through coordinate transformation employing matrix formulations. Therefore, the local volume of material removed by every single grain is calculated as a function of the relative motion between the grinding wheel and the workpiece. Konig et al. developed a closed loop simulation to model the kinematic geometrical engagement of grains in the material, where the forces at the individual grain are transformed into grinding forces and a heat source is calculated from the heat produced at all individual cutting edges engaging in an interval of time [111], [112]. The model ideally represents the grinding wheel motion and the interaction with the workpiece neglecting the wheel deflection and the workpiece deformation. Inasaki et al. detected the wheel topography by means of optical profilometry and simulated the grinding process to predict the ground surface roughness and the grinding force [113]. This kind of approach represent a useful way to analyse the roughness outcomes due to grinding but it is not usually adopted to estimate thermal effect of the process because it cannot take in consideration the material ploughing during the removal mechanism.

## 2.7. FEM models

Also grinding finite element models (FEM) were implemented following the two different approaches classified in micro-scale and macro-scale models [114]. As exposed before, micro-scale approaches focused on the single grain action on the workpiece and analyse the mechanical behaviour during ploughing and cutting mechanism giving information about the forces generated during the process due to material and kinematics. The finite element FE method provides the requisite numerical solutions as well as the multi-physics analysis by coupling thermo-elastoplastic solutions to consider not only the mechanical phenomenon of material removing mechanism but also the ploughing effect due to the material and the correlated thermal aspects. Doman et al. simulated, by

means of scratch tests, the action of a single abrasive, represented by a spherical body, on the material considering the rubbing and ploughing phases [115]. Chen et al. considered the grinding microscopic phenomena by varying the friction coefficient that has direct influence on grinding forces and specific energy by implementing a FE model in ABAQUS [116]. Anderson et al. investigated the effect of the grain size and depth of cut on material deformation considering the pile-up height. They developed a 3D model by representing the abrasive grain as a sphere and modeling the workpiece based on the combination of multi-material Eulerian and Lagrangian elements. They demonstrated a reduction in the material pile-up by increasing the cutting speed, together with a rise in normal forces due to material hardening and a reduction in the tangential forces due to the lower friction between the tool and the workpiece [117]. Yang et al. implemented a FE model in DEFORM-3D to study the high-speed characteristic of cylindrical grinding [118]. Also Zhang et al. implemented a model to analyse the grinding material removal mechanism by considering a virtual grinding wheel based on a random distribution of multi-grains action [119]. Chen et al. developed a model to analyse the effect of multiple scratch passes on the material by adopting a single-grit approach concluding that the grit shape has a huge influence on the grinding forces [120]. In general, the main FE model present in literature use a simplified defined geometrical shape to represent the abrasive grain, but a more thorough analysis on the grain contact area needs to be done.

FE macro-scale models consider the interaction between the whole grinding wheel and the material from the thermal point of view. They focused on forecast thermal burns considering a threshold value of temperature starting from process power measurements assuming a certain value of energy partition which represent the heat absorbed by the workpiece. As explained for the macro-scale analytical models, also FE macro-scale models aim at forecasting thermal responses in grinding, replacing the action of the grinding wheel with a moving heat source. Anderson et al. developed two models, one for shallow grinding characterized by low depths of cut without considering the effect of contact angle and one for the deep grinding with large depths of cut including the effect of the contact angle [121]. Linke et al. developed a 3D model deriving the heat source profiles from experimental tangential force signals [122]. Also Mohamed et al. dealt with grinding temperatures prediction by replacing the wheel pass on the material with a moving heat source whose shape was varied in order to optimize the model [123].

Kundrak et al. proposed a finite volume simulation adopting a realistic representation of the grinding wheel and workpiece motion calibrating it by means of experimental tests [124]. Within this approach the grinding power represents the main contribution in calculating the heat flux and it is usually measured experimentally, while greater difficulties are found in obtaining the real value of the energy partition ratio.

Current models based on force and temperature prediction have multiple limitations and use approximations that make them instruments hardly usable in the industrial field for complex processes such as gear grinding. The complexity of tool and gear geometries, the structure of the grinding wheel and its non-deterministic nature combined with the high deformation rates of the material make it very difficult to develop a material cutting model considering the grinding parameters and wheel specification. Empirical and neural network approaches could reduce the computational effort but, in the first case, the experimental extensive coefficient calculations still influence the prediction results, instead, in the second case, the lack of transparency of the knowledge stored leads to a poor acceptance in industry. Analytical model could represent a simplified first attempt analysis for the grinding process outcomes which do not take in consideration many random aspects of the process. Geometrical-kinematics models, instead, could represent an efficient solution especially for roughness prediction, but many efforts need to be done in the thermal analysis of grinding removal mechanism. At the end, molecular and FEM models could represent a suitable solution to detect thermal defects, but they require previous knowledge and substantial computational power.

The model proposed in this work is based on a combined micro-scale and macro-scale approach adopting for both aspects a FEM model and it will be widely described in the following chapters. It is composed by a mechanical model representing the action of a single grain on the material, followed by a thermal model, where the interaction between the grinding wheel and the material was represented by a moving heat source. The moving heat source was design starting from the single grain power calculated with the mechanical model and by introducing the process parameters and the grinding wheel specifications. The proposed model could predict dry grinding process temperatures avoiding time-consuming experimental tests, in general executed to measure grinding forces and power in the main approaches presented in the literature. The main computational limits have been found for the mechanical model, being the interest zone

micrometric and needing a very fine mesh. Therefore, some adjustments have been adopted to ease the simulations maintain the calculation precision and they were exposed in the following sections.

# Chapter 3

# Context and project goals description

## 3.1. Context description

Over the past 30 years the main direction taken for the development of grinding processes generation was to increase the process productivity. To dealt with this purpose a first improvement was achieved thanks to the increase in the number of wheels starts. In 1975 only 1 or 2-starts grinding wheels were used, while currently it is common to use a minimum number more than 3 or 4 starts ensuring greater productivity. Productivity has also been increased by introducing solutions to reduce the downtime during the production, such as quick clamping systems for tool changes or loading and unloading systems of workpieces. Another requirement for the grinding machine producers was to increase the cutting speed. Purpose for which machine producers and grinding wheels' manufacturers have invested a lot of resources. The results achieved were remarkable from maximum speeds of 35 m/s in 1975 to exceed the threshold of 100 m/s in today's most demanding applications. Increasing the cutting speed could be possible only if the load applied on each abrasive remains almost constant. Only under this condition the increase in cutting speed can be translated into an increase in productivity. But, an increase in the cutting speed leads to an increase in the thermal load generated in the contact area between the wheel and the material increasing the risk of grinding burns.

Beyond this process performance requirement, another challenging improvement for the grinding machines producers could be represented by the complete elimination of oil. Nowadays, grinding is the only production process still using lubricant in the gear production chain, as can be resumed from Figure 31. Lubricant's reduction or removal could lead to a substantial reduction in costs and environmental pollution. Indeed, the contact with lubricants could cause several health problems, such as dermatological and respiratory diseases. Most of them are not biodegradable and contain several dangerous substances. Moreover, the use of oil in material removal processes involves many practical difficulties to manage. Some measures must be taken in consideration related to the unavoidable losses and dispersions. Moreover, to manage the amount of lubricant

during a grinding process it is necessary to design and optimize its supply and auxiliary systems, that constitutes a significant part of the purchase cost and the space required for the installation of a grinding machine. The total amount of oil required for a gears grinding machine can vary between 2000-4000 l, of which 100-200 are lost every month and must be replenished. Oil losses are due to its dispersion in the environment by nebulization that occurs during the grinding process, by direct leakage of fluid from the machine and by residues that remain on the product component lost in transport and washing. The losses described have numerous negative effects on the health of operators and the environment. Furthermore, the waste produced by the grinding process (oil, metal chip, abrasives etc.) needs to be separated though expensive treatments. But, as explained in the previous sections, lubricants have a relevant role in reducing heat and the thermal damages risk during the process, therefore, its elimination represents a very complex requirement to accomplish.
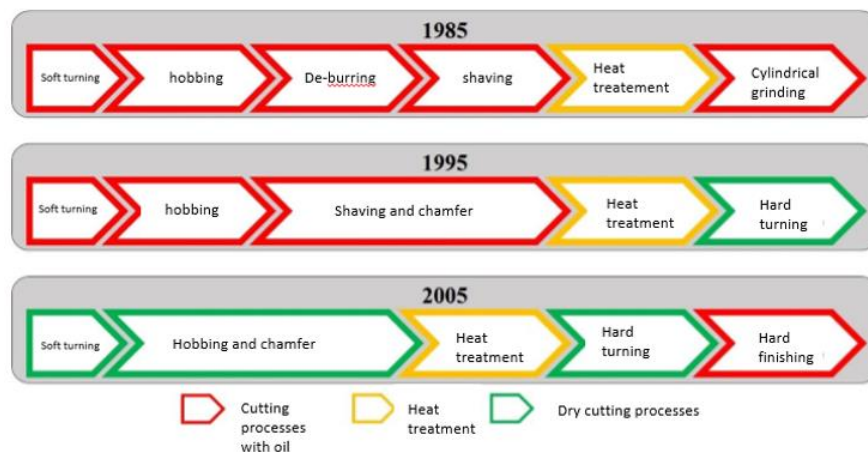


Figure 31.Gears production chain evolution through the elimination of lubricants

The company Samputensili Machines Tools accepted this challenge developing the gear dry grinding process and the dry grinding machine SG 160 SKYGRIND (Figure 32-Figure 33) in 2015, where the finishing phase is made up of two different operations: a roughing phase where a hob tool removes the main part of the material on the gear, and a finishing phase where a worm grinding wheel removes a minimum quantity of material. Considering the machine structure, it presents two spindles that move the skive-hob and the grinding wheel, respectively, in order to perfectly control position and speed of both tools at their nominal speed [19]. During the production, their motions guarantee a time

of chip-to-chip, a process time duration for one gear, less than 2 s. Indeed, the X axes is split in two linear slides X1 and X2, each of them moving a worktable with a gear (Figure 34). Moreover, being the cutting fluid, in conventional grinding process, relevant for reducing the particles dispersion, the absence of lubricant could lead difficulties, not only in the thermal defects management, but it could also cause damages at the machine axis and the ventilation system due to swarf dispersion. To overcome this problematic, the SG 160 SKY GRIND was adapted by introducing an oversized aspiration system.



Figure 32. Samputensili SG 160 SKY GRIND

Figure 33. SG 160 SKYGRIND working configuration
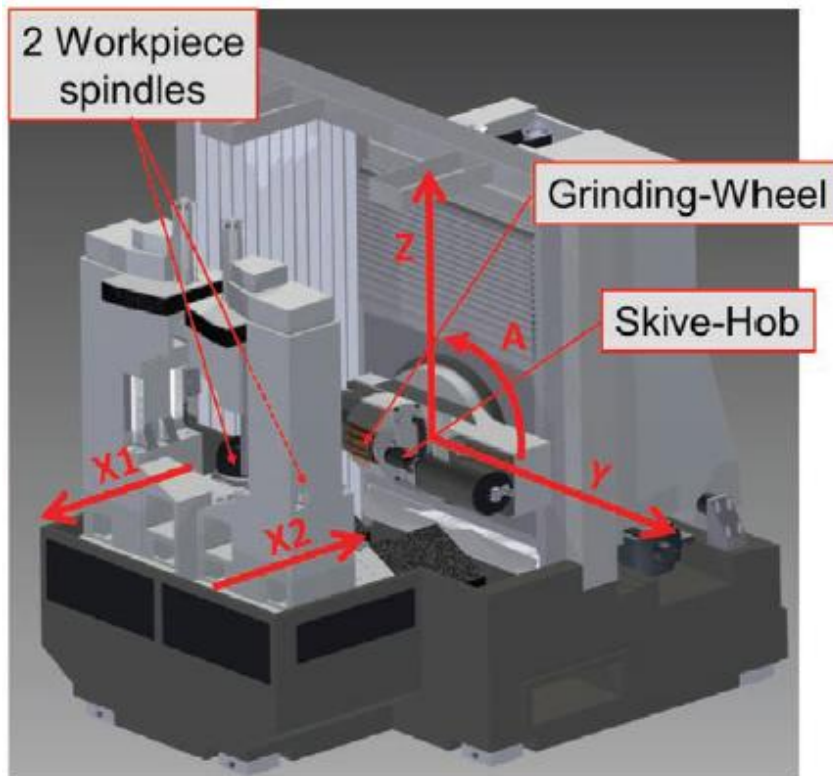


Figure 34. SKYGRIND machine structure

In Table 3 the SG 160 SKYGRIND machine technical data are reported.

Table 3. sg 160 SKYGRIND technical data

| SG 160 SKYGRIND machine | |
|---|---|
| Maximum gear diameter | 160 mm |
| Gear module | 1 – 3 |
| Maximum gear length | 300 mm |
| Maximum gear width | 180 mm |
| Helix angle | +45°/-45° |
| Wheel diameter | Max 250 mm/ Min 210 mm |
| Wheel width | 100 mm |
| Maximum wheel speed | 80 m/s |
| Machine dimensions L x W x H | 3275 x 2200 x 2285 mm |
| Control system | Siemens Sinumerik 840 D sl |

Samputensili Machines Tools has the duty to deliver not only the grinding machine, but also the optimized process parameters set, comprising the kinematics parameters and the grinding wheel specification, that makes each application feasible. To date, automotive transmission gears are ground by eliminating the 80% of material in the first roughing phase [125] and then the remaining 20% of material is removed through a finishing phase that is performed to obtain the final requirement of tooth flank roughness and geometry. The new approach developed by Samputensili Machine Tools is based on the application of a dual finishing phase. Indeed, the finishing phase is divided in two different steps: at first, a skive-hobbing tool, capable of removing hardened material without the use of oil, is employed to remove the 90% of allowance from the teeth flanks; then, a dry grinding phase is performed with the goal to remove the remaining 10% of material. In this way, the material removal rate during grinding is reduced aiming at decreasing the probability to induce grinding burns on the gears flanks. Indeed, the material removed during grinding could be identified as a combination of the grinding parameters, speed, feed rate and depth of cut. It can be deduced from conventional

grinding theory that a reduction in infeed combined with an increase in feed rate leads to a reduction in heat development for the same material removal rate [18]. Therefore, the infeed is reduced to the minimum required to remove feed marks and achieve the necessary surface integrity. Indeed, it was observed that as radial infeed is increased, damage becomes progressively more evident in terms of microstructural degradation and changes in hardness [126].

## 3.2. Activities description

The context in which this Ph.D. project has been inserted deals with the gears grinding for the automotive sector related to the mass scale production cars. With the aim at making the gears production totally green, keeping the gears quality at the same level of those ground through the conventional wet grinding, Samputensili Machines Tools decided to invest in research and development to reduce the thermal defects occurrence by modelling the process. Indeed, being the dry grinding a non-deterministic process with higher probability of incurring in grinding burns compared to the conventional process, a preliminary modelling phase that consider all the process parameters becomes essential. Therefore, the Ph.D. research activities have been focused on optimizing a model which takes in consideration, at first, the technological process parameters, such as the depth of cut, feed rate and cutting speed, and then, also the grinding wheel specifications, considering its porosity and the binder grade.

The activities were divided into experimental research and modelling research and took place between the laboratory of the University of Bologna and Samputensili Machine Tools company. As before explained, the process temperature prediction was reached by implementing a hierarchical FEM model made up of two different steps correlated with their proper validation. Therefore, considering the research timeline, the activities could be summarized in the following points:

- Analysis of the abrasives' geometries acquisition by means of computed tomography;

- Analysis of the single grain grinding tests with forces measurement by using single abrasive grain with size 60 in fused and sintered aluminium oxide. The tomography and single grain grinding tests results were extrapolated by a previous work that focused on the same topic [127], [128].

- Single grain grinding simulations with the software DEFORM 3D and results processing through MATLAB.

- Abrasives' geometry observation through the STL editor software Magics Materialize considering the main geometry characteristics, such as the rake angle, the tip radius, the grain width and length, followed by a statistical analysis of the main grains features to design an equivalent defined grain geometry representative of a grain size and material class.

- Calibration and optimization of the flow stress curve of the case-hardened depth steel adopted to represent the gear surface material by means of an inverse cutting simulation-based approach.

- Tangential dry grinding tests on prismatic samples with temperature measurements by means of embedded thermocouples using different grinding wheels' specifications.

- Grinding wheels' topography analytical study and experimental observation at the stereoscope to obtain a specific grain density value that define the grinding wheel specification.

- Tangential grinding simulations by implementing a thermal model in COMSOL MULTIPHISICS and temperature results analysis.

- Samples microstructural analysis and surface micro-hardness measurements and correlation with the temperature acquisition.

- Gear dry grinding experiments using two different grinding wheels specifications on the SG 160 Sky Grind machine developed by Samputensili Machine Tools.

- Gear dry grinding thermal simulations implemented in COMSOL MULTIPHISICS by considering the gear tooth geometry and the gear grinding kinematics. The gear grinding kinematics implementation was extrapolated from a previous work and adapted according with the optimized modelling procedure.

- Microstructural analysis of the gear tooth flanks to validate the model.

- Dimensional tolerances and roughness control and comparison with a gear ground through the conventional wet process to verify the gear dry grinding feasibility.

# Chapter 4

## Single grain grinding modelling and experimental validation

In this chapter, the first step of the proposed grinding model will be presented and the attention will be focused mainly on two phases: the definition and optimization of the abrasive grains geometry and the calibration of the material flow stress curve representing the case-depth of a case-hardened steel. A micro-scale approach which used a 3D single-grit model to predict forces during grain-workpiece interaction in dry conditions was proposed as the starting point to design a moving heat source representing the grinding wheel pass on the material.

An initial simulation was implemented based on the real grain geometry acquired by means of computed tomography, after which an equivalent defined grain geometry was designed to facilitate computational aspects. The equivalent defined grain geometry was obtained by considering the rake angle, tip radius, opening angle and width of the real grain, taking care to mantain the same grain orientation during experiments. Correspondence between the behavior of the simplified equivalent grain and the real geometry was first verified in terms of load values using the Johnson & Cook (J&C) coefficients of a reference material.

Subsequently, an optimized flow stress curve for the case-hardened depth of a typical steel employed for automotive gears was implemented. Starting from the reference material, an inverse parameter identification was performed to optimize the flow stress curve for the steel in question by replacing previous material coefficients with more accurate values, better representing the behavior of the measured hardness of the case-hardened steel. A simulation plan using the defined grain geometry was developed to check and calibrate the Johnson & Cook constitutive material coefficients.

The model also considered the real kinematics of the grinding process, which implies multiple rotations of the same abrasive grain on the workpiece surface. Model validation was performed by comparing tangential and normal loads with experimental data for two different grain geometries and size. The good agreement between the model and experimental results confirmed that the simulation with the proposed approach to simplify

the abrasive grain is a viable way to model the grinding process and the flow stress coefficient adopted is suitable to describe the behavior of the case-hardened depth of a typical automotive gear steel under cutting conditions [129].

## 4.1. Single grain grinding experimental tests

The experiments considered for the single grain grinding model optimization were elaborated from a previous work [127]. Single grain grinding experiments could be divided in two test steps. The first one used fused aluminium oxide ($Al_2O_3$) abrasives with FEPA size 16. A coarse size was adopted with a large depth of cut of 0.1 mm to magnify the material removal mechanism in grinding and ease the model computational requirement. The second test step is based on sintered aluminium oxide abrasives tests with a finer size of 60 and a depth of cut equal to 0.01 mm, a more realistic value in a grinding process. In both cases, the tests were performed on a computer numerical controlled (CNC) milling machine, as shown in Figure 35. A single-grain configuration was employed by attaching a single abrasive grain to a 150 mm diameter metallic holder with epoxy resin as shown in Figure 36.
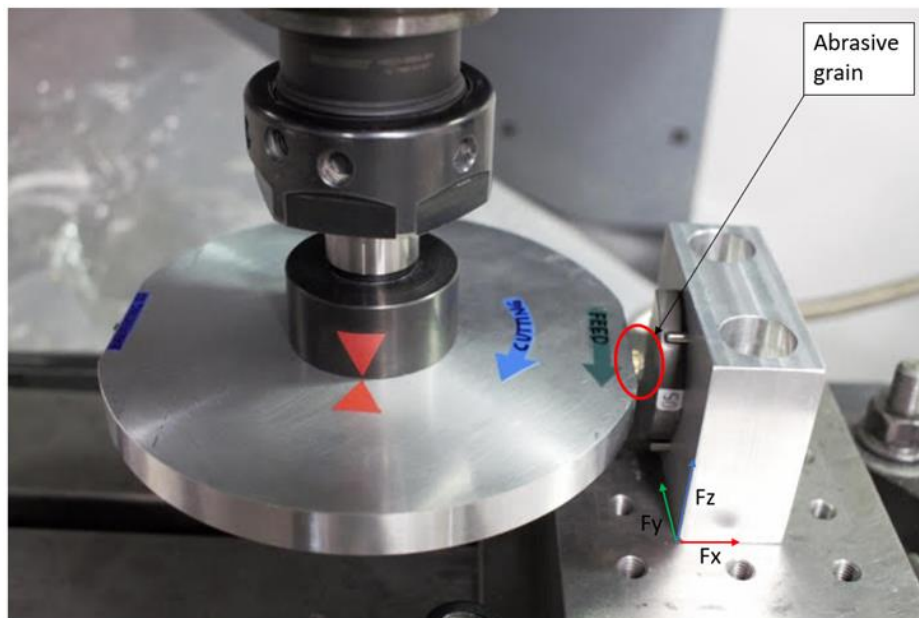


Figure 35. Single grain grinding test set-up
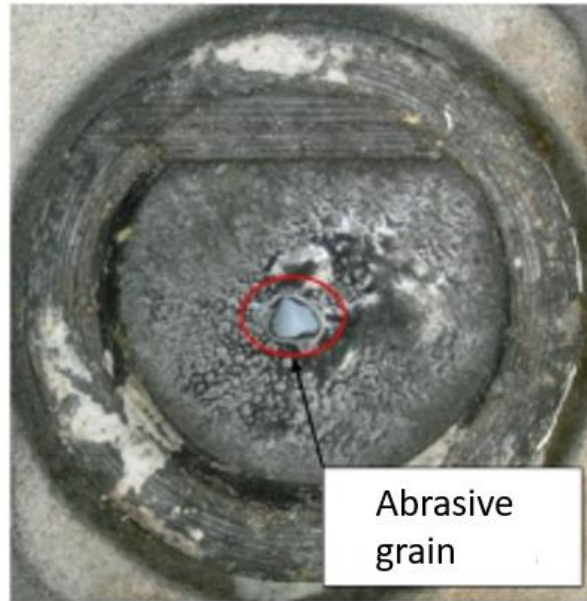
Figure 36. Single grain grinding tests abrasives configuration

Cutting force components were measured using a Kistler 9257B dynamometer with a frequency acquisition equal to 10000 Hz performing three repetitions for each test. Case-hardened 27MnCr5 steel was employed as the workpiece material. Heat treatment was first performed on the workpiece to replicate a tooth gear surface and achieve a hardness of 750 HV1 to a depth of at least 1 mm, after which the blocks were pre-ground. Tests and simulations considered in this analysis were performed using the following process parameters sets. Two different single grain grinding experiments were considered for the first test step using fused aluminium oxide abrasive with size 16. The first test was used to check the grain geometry optimization procedure and calibrate the material flow stress; the second test, which used an abrasive belonging to the same size and material class of the previous one, was characterized by a different shape and was used for the single grit model validation. For the first abrasives group with size 16, it was employed a cutting speed of 30 m/s, a feed rate of 8.6 mm/s and a depth of cut of 0.1 mm. A higher than the usual grain dimension and depth of were used at first to ease the simulation calculation in that the goal is to validate the single grinding grain model calibrating the flow stress curve and optimizing the grain tool geometry. For further validate the single grit grinding model, another experiment that used sintered aluminium oxide with size 60, was analysed. In this case, it was adopted a cutting speed of 30 m/s, a feed rate of 50 mm/s

and a depth of cut of 0.001 mm. The experimental test parameters were summarized in Table 4.

Table 4. Single grain grinding experimental parameters set

| Single grit tests | Grains material | Grain size | Depth of cut [mm] | Feed rate [mm/s] | Cutting speed [m/s] |
|---|---|---|---|---|---|
| Test step 1 | Fused aluminum oxide | 16 | 0.1 | 8.6 | 30 |
| Test step 2 | Sintered aluminum oxide | 60 | 0.001 | 50 | 30 |

Force signals acquired by the dynamometer were then processed in MATLAB to extract the load component for each full rotation of the single grit wheel. The complete processing is therefore composed of several revolutions determined by the combination of the kinematic test parameters. This kinematics allows to have a gradual engagement of the grain in the material. Indeed, in the first revolutions the grain only touches the workpiece and only when the median axis of the grinding wheel is at the edge front of the sample the total depth of cut that will be reached. Once the first revolution to "full engagement" is reached, the abrasive grain can remove material at the set depth of cut reaching the maximum cutting forces recorded. This type of kinematics is very close to the actual cutting conditions of grinding processes in which the abrasive grain works on a portion of material resulting from the passage of the previous grain and a portion of material not yet ground.

## 4.2. Single grain grinding model description

In this section the single grain grinding model will be presented. The model was first validated considering the fused aluminum oxide abrasives tests with size 16 by defining the grain geometry and optimizing the material flow stress curve. In particular, the study will show the analysis developed on two different grain geometries. Then a further validation was provided by comparing calculated and measured grinding forces within the sintered aluminum oxide abrasives experiments with size 60. At the end, a statistical

analysis on the sintered aluminum oxide grains geometries was implemented to design a grain shape enough representative of this abrasive material and size class. The optimized grain geometry will be adopted in the subsequent simulations to calculate the single grain grinding power and design the moving heat source representing the grinding wheel thermal effect.

The modeling approach employed to initially validate the single grain grinding model, shown schematically in Figure 37 is based on three simulation approaches using the same FEM input parameters such as mesh discretization, kinematics, time step, friction coefficient and fracture criterion. The first approach adopts the real grain geometry acquired through computed tomography and the flow stress curve coefficients of reference material. The second sees the replacement of the real grain with an equivalent defined grain geometry using the same material flow stress curve. Finally, the third simulation approach adopts the same equivalent defined grain but employs a new optimized material flow stress curve. Calibration of the flow stress curve was performed by means of a simulations plan based on the maximum cutting depth reached during the process varying J&C coefficients. The outcomes of each simulation approach were analyzed in detail and compared with experimental results [129].
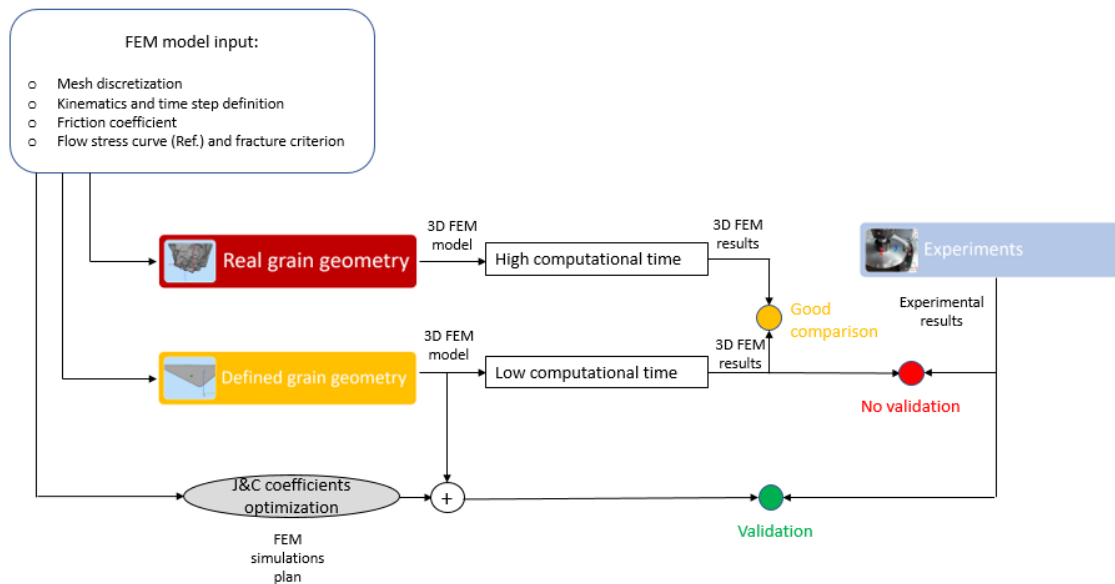


Figure 37. Flow diagram of modelling approach and experimental verification [129]

A thermomechanical FEM simulation was implemented in DEFORM-3D adopting a Lagrangian incremental formulation and both modes have been activated for the calculation of deformations and thermal aspects. To reduce file size with the results it was decided to save the simulation at intervals of 5 calculation steps. Interaction between the workpiece and grain in dry contact conditions was simulated considering a constant Coulomb friction coefficient of 0.2 [130]. Since grain hardness (2085 Vickers microhardness) is much higher than workpiece hardness (750 HV1), the former was modelled as a rigid body with real grain geometry acquired by computed tomography. The workpiece was represented as a deformable prismatic body with dimensions sufficient to achieve the minimum stroke required to reach complete grain penetration defined by the chosen depth of cut. The workpiece was modelled with tetrahedral elements distributed within windows characterized by decreasing element dimensions moving towards the interaction zone. Specifically, four mesh windows were prepared to have a decreasing mesh dimension at the contact surface with the smallest element equal to one-third of the cut depth, as shown in Figure 38. The workpiece mesh was set as an absolute mesh, while the grain mesh was set as a relative mesh with a size ratio of 20.
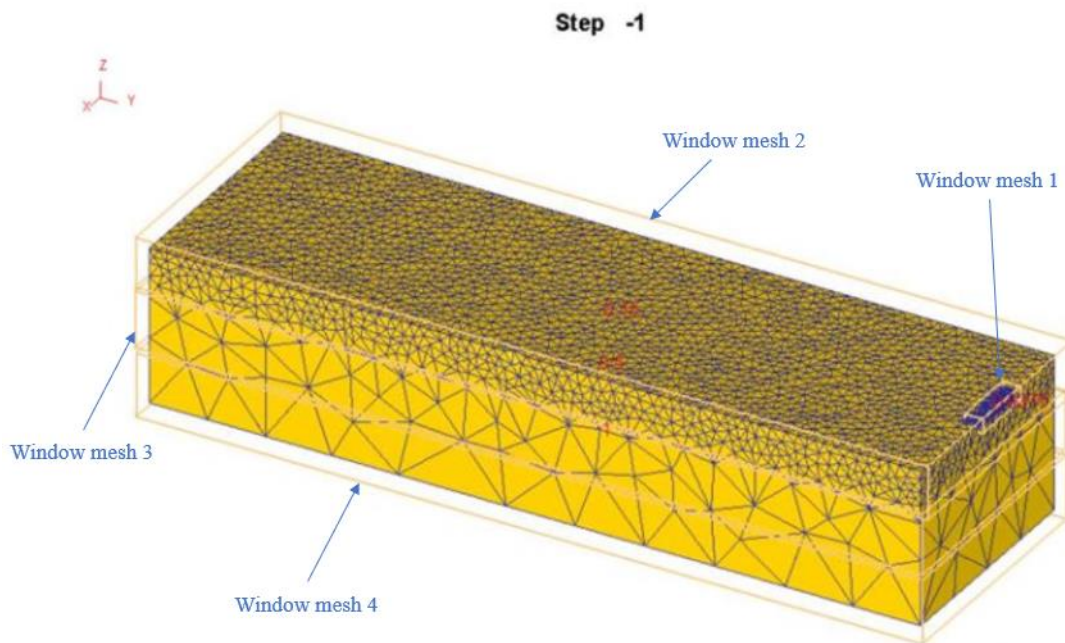


Figure 38. Workpiece mesh windows discretization

The total number of workpiece elements and nodes was 16975 and 3867 for p = 0.1 mm and 58893 and 13204 for p = 0.01 mm, respectively. Translation and rotational movements were assigned to the grain to represent the real kinematics during experiments. Up-grinding was considered, with the grain trajectory programmed such that the centre of rotation was located above the workpiece edge. The virtual grinding wheel had a diameter of 152 mm and interacted with the workpiece. Zero velocity boundary conditions were applied to the lower workpiece surface to maintain its position fixed in the space (grey zone in Figure 39).
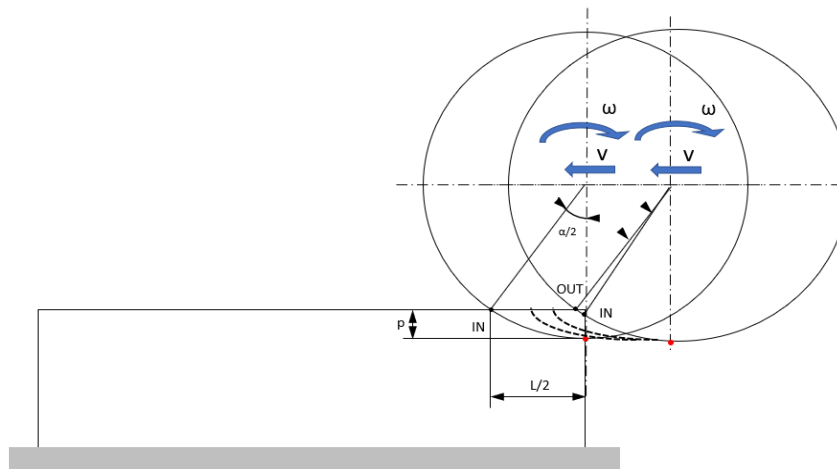


Figure 39. Single grain grinding model kinematics [128]

Variable time steps were applied to reduce calculation time, with the grain-workpiece interaction phase assigned a time step of 100 ns and the remaining rotation phase 100 µs. Due to the high degree of detail required to represent the problem in a FEM environment, many difficulties were faced due to limited computing power, especially employing real grain geometry characterized by a large number of elements.

The data provided by the simulation and the calculated quantities are displayed in the post-process environment. The simulation allows the calculation of the process forces necessary to deform the material being processed and generate the chip. In the graph reported in Figure 40, the tangential grinding forces trend was shown. It is noticed that the grinding pass forces increase progressively as the portion of processed material increases reaching the status of regime when the grain fully engages the material at the cut depth set. The abrasive grain continues processing advancing on a groove that

is to form for successive passes, working an area of the material already worked during the previous stroke until the portion of material is engaged which has not yet been deformed.
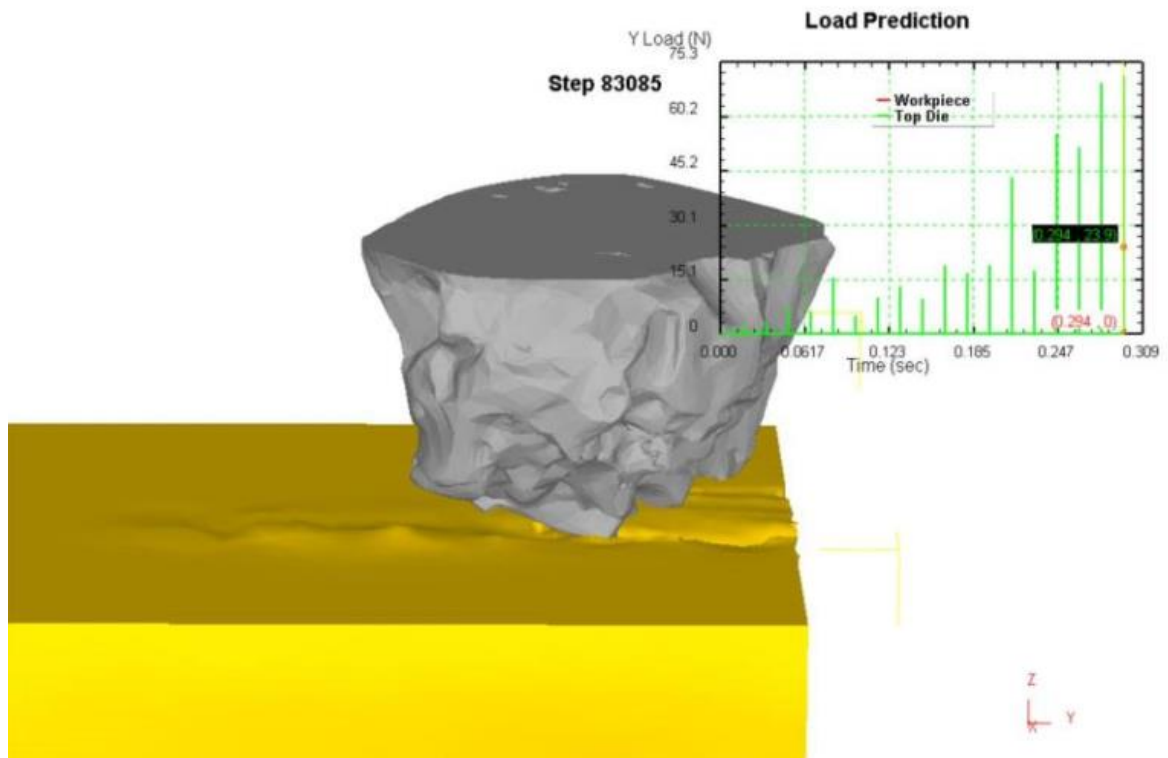


Figure 40. Single grain grinding forces DEFORM 3D calculation

The cutting process generates heat-dissipated energy at the grain-material interface. The temperatures reached are very high (Figure 41), close to the melting temperature of the steel, but develop during a very short working time, in the order of tenths of milliseconds.
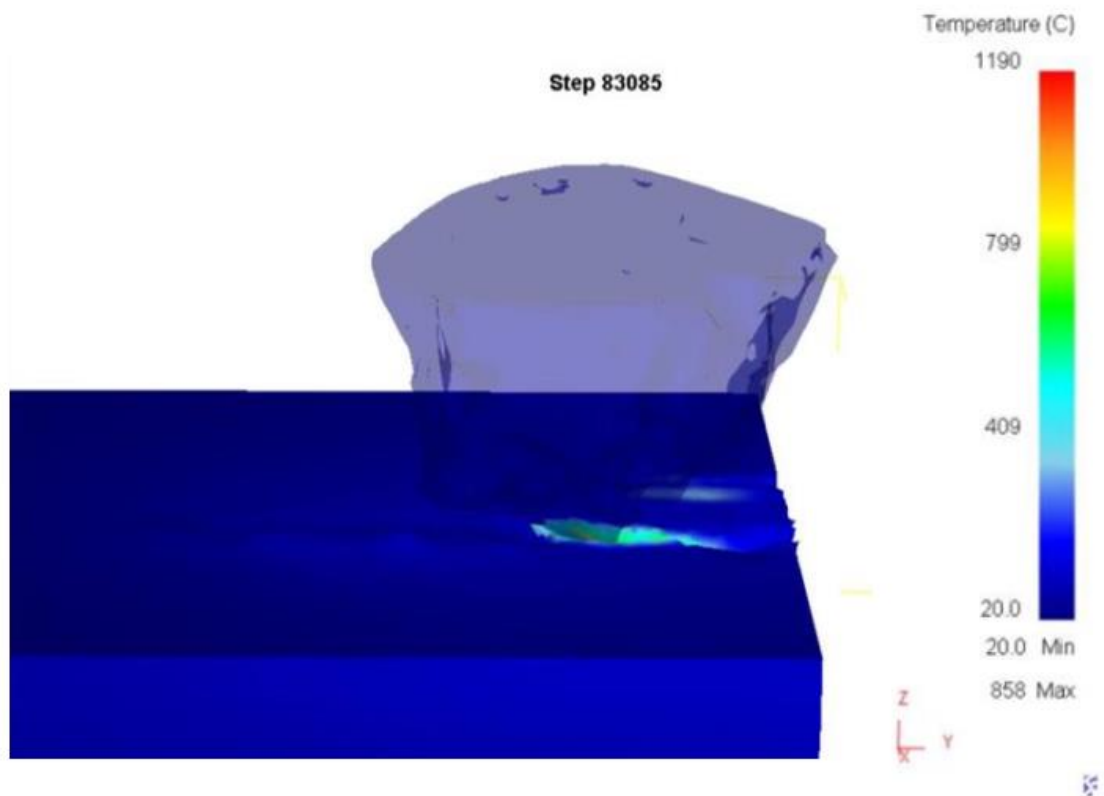
Figure 41. Single grain grinding temperatures DEFORM 3D calculation

## 4.2.1. Abrasive grains geometry analysis and definition

The first simulation approach was implemented using real grain geometry acquired by computed tomography to gather as much information as possible in relation to the real contact area (Figure 42).
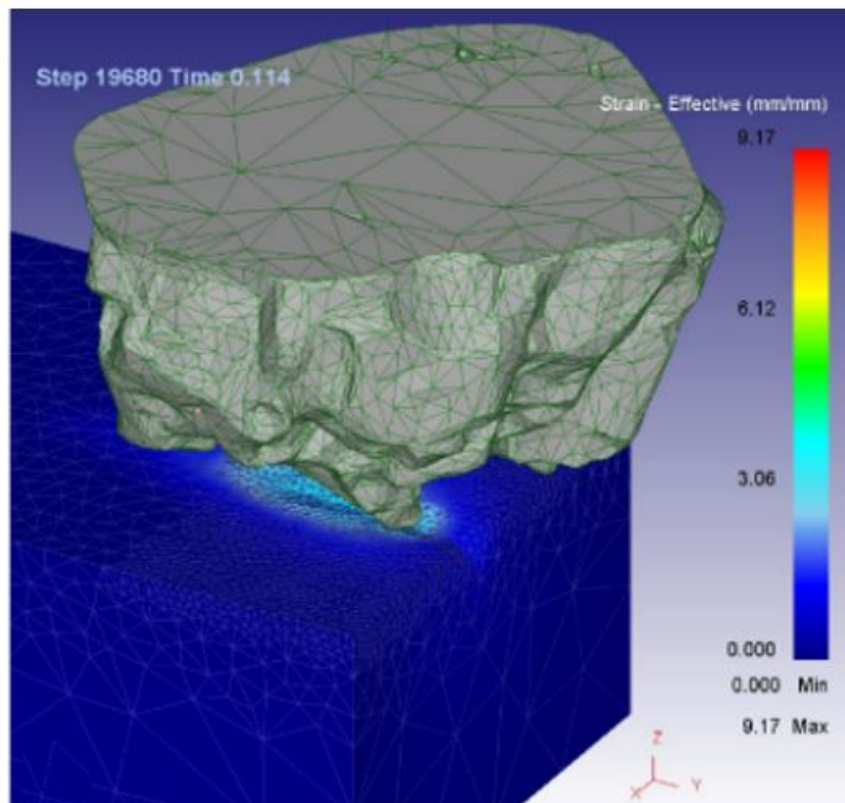
Figure 42. Real grain model simulation

Subsequently, the real grain geometry was geometrically analyzed considering the rake angle, the tip radius, opening angle and width [131]. A grain with defined geometry was implemented with characteristics comparable with that of the real grain, including a negative rake angle of 62°, a tip radius of 0.05 mm, opening angle of 9.8°, a width of 0.6 mm and the same nominal contact area. The contact area was considered as the projected chip load area on the Y-Z plane and measured with STL editor software Magics Materialize, as shown in Figure 43. The arrows represent the translational and rotational movement of the grain during the simulation and experiments. The nominal contact area between the grain and workpiece was measured in correspondence with the cutting depth $p$ by correctly identifying the grain position during experiments. The grain geometry was sectioned along the x-axis (Figure 43 b) in correspondence with the maximum grain height and along the z-axis at a height of $p$ (Figure 43 c).
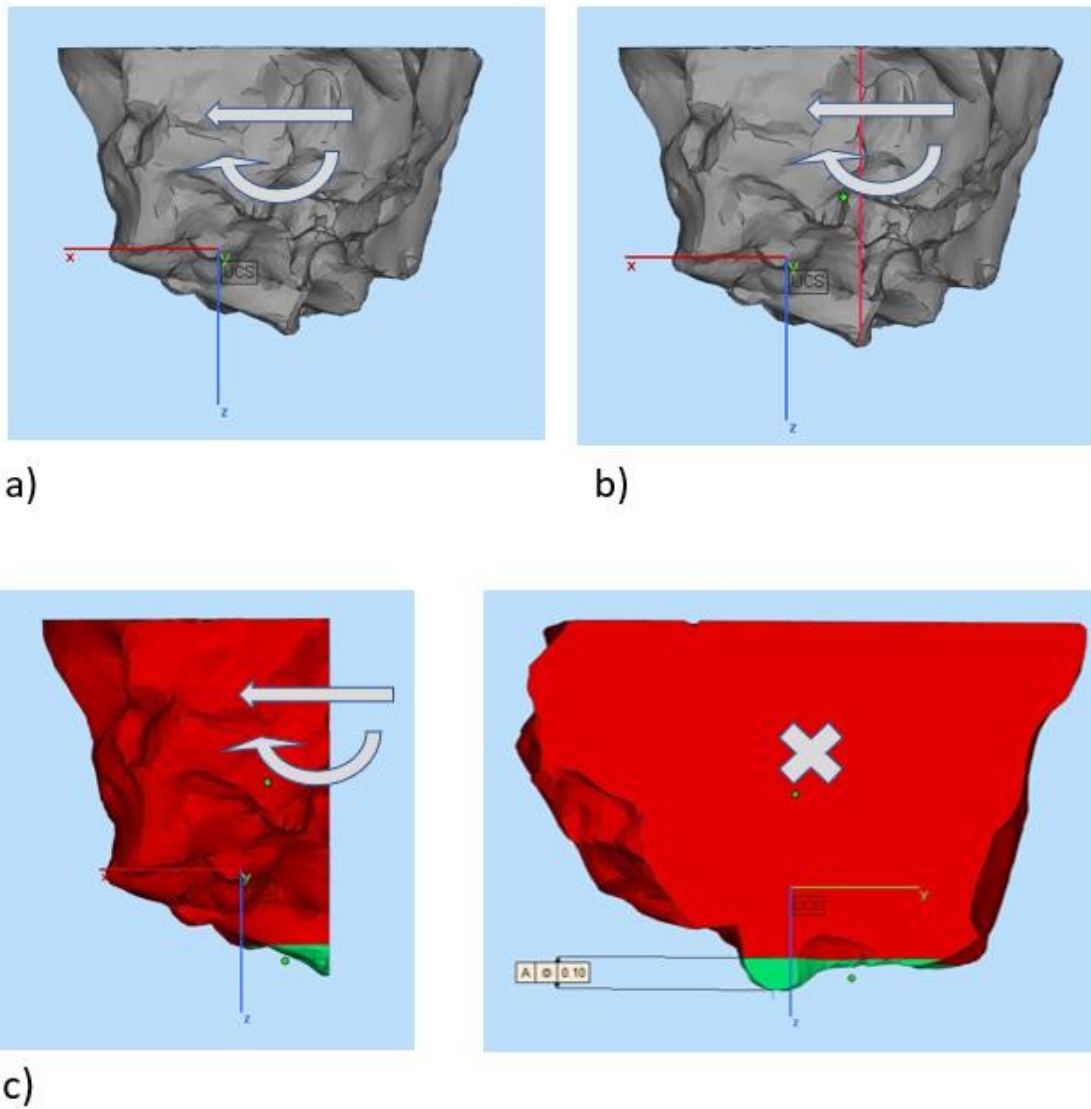
Figure 43. Grain contact area definition: a) grain positioning; b) grain section along the x-axis; c) grains section along the z-axis [129]

It can immediately be noted that a very small portion of the grain was actually involved in cutting, for which it was considered plausible to define an equivalent grain geometry and simplify the load simulation phase. The real and simplified grain, together with their principal geometric characteristics, are compared in Figure 44. The main differences between the grains with real and defined geometry related to the number of elements and nodes required to represent the body. In particular, the grain with defined geometry could be discretized with dozens of nodes and elements, while the real geometry required tens of thousands of nodes and elements, as reported in Table 5.

Table 5. Discretization of real and defined grain geometries

|  | Real grain geometry | Defined grain geometry |
|---|---|---|
| N° nodes | 10292 | 70 |
| N° elements | 46043 | 186 |
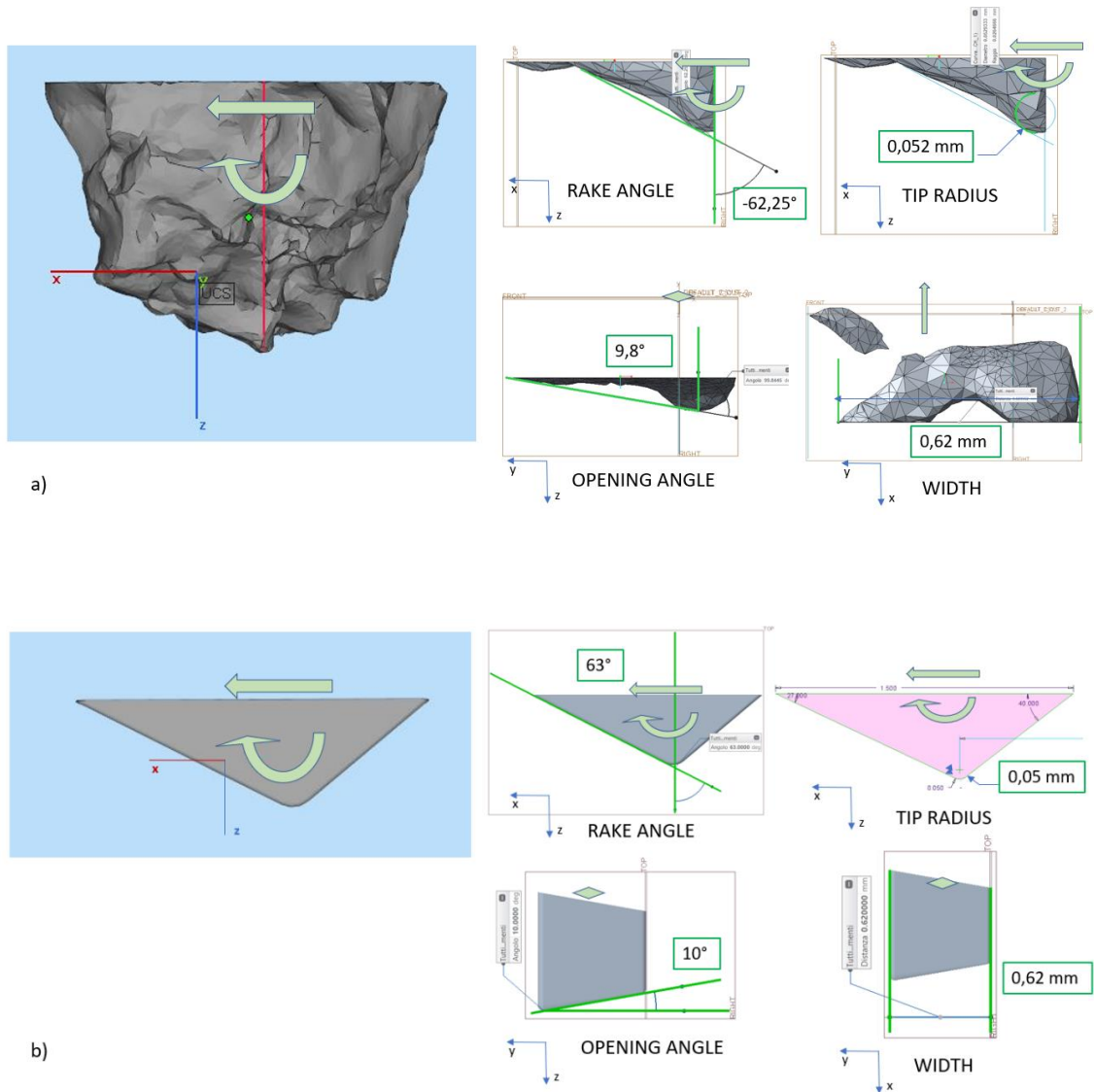


Figure 44. Grain geometry analysis: a) real grain; b) defined grain [129]

The real grain geometry, despite representing the contact area very accurately, required a large quantity of data for detailed representation and needs weeks for calculation. The equivalent defined grain geometry simulation (Figure 45) required much less data for

simulation, allowing single grit grinding forces to be extensively examined by introducing a good estimate of cutting loads with a lower calculation time of some days. For the test step 2 which adopted sintered aluminum oxide, the grain geometry analysis and definition applied was the same discussed in this section.
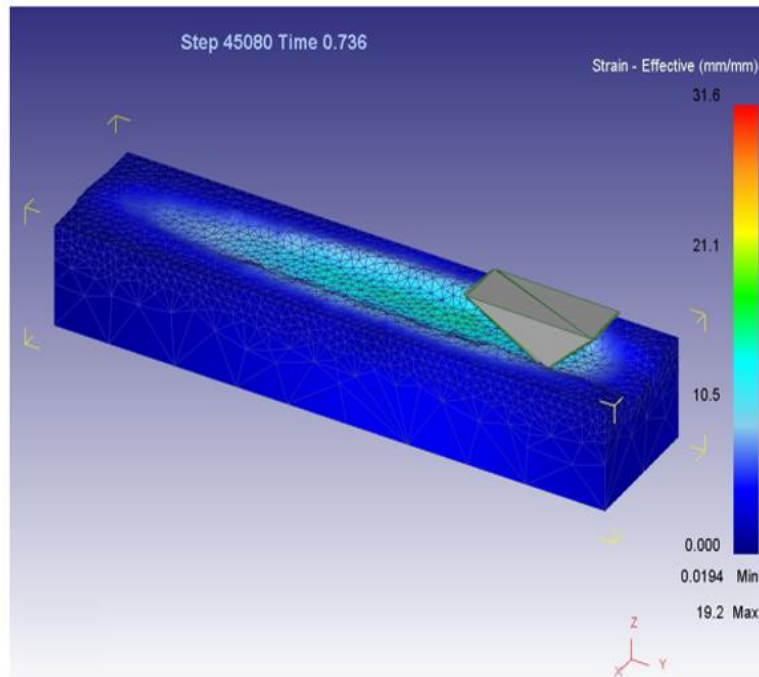


Figure 45. Equivalent defined grain model simulation

A statistical analysis of the geometrical characteristics was developed on multiple samples to identify a single defined geometry representative for the whole abrasive material and size class. More details will be discussed at the end of the chapter.

## 4.2.2. Material flow stress curve optimization

Aluminum oxide was assigned as the grain material. For the workpiece material the Johnson-Cook model, widely used to represent materials viscoplastic hardening and thermal softening with high strain-rate dependency [132], [133], was employed to describe material flow according to Eq. (16):

$$\sigma = ( A + B \cdot \varepsilon^n) \cdot (1 + C \cdot \ln \frac{\dot{\varepsilon}}{\dot{\varepsilon_o}}) \cdot [ 1 - (\frac{T - T_r}{T_m - T_r})^m] \qquad (16)$$

where the parameter A is the initial yield strength of the material at room temperature, $\dot{\varepsilon}$ is the equivalent plastic strain rate normalized with a reference strain-rate $\dot{\varepsilon}$ e, $Tr$ is the room temperature, $Tm$ is the melting temperature of the material, and *B*, *C*, *n* and *m* are model parameters. The parameters *n*, *m* and *C* are the strain-hardening exponents, thermal softening exponent and strain-rate sensitivity, respectively. An initial reference material [134] with the same surface hardness of case-hardened gear steel was considered as starting point for the flow stress curve calibration. The authors have determined its J&C coefficients through a characterization method based on split Hopkinson pressure bar (SHPB) technology, which leads to characterize the reference material properties at high strain rates and high temperatures. The SHPB system is widely used for the determination of the dynamic mechanical properties of materials. Indeed, it allows to apply mechanical testing of the material at strain-rates from $10^{-2}$ s$^{-1}$ to $10^4$ s$^{-1}$ by applying an impact load on the sample after it reaches a defined temperature. This technique could be useful to characterize material under high strain rates, such as cutting conditions where the material is subjected to severe deformation in a limited time with increase of temperature. Flow stress coefficients and material properties of the reference material are reported in Table 6.

Table 6. J&C parameters and material properties of reference material

| J&C parameters | A | B | n | $T_r$ | $T_m$ | C | m |
|---|---|---|---|---|---|---|---|
| Ref. Material | 2480 | 1440 | 0.45 | 20 | 1460 | 0.012 | 1.1 |

| | $\rho$ (kg/ m$^3$) | $c_p$ (J/kgK) | $\lambda$ (W/mK) |
|---|---|---|---|
| **Material properties** | | | |
| Workpiece | 7850 | 354-916 | 24.57-24.75 |
| Grain | 3950 | 747-1106 | 6.10-23.71 |

Having the same hardness as case-hardened steel but diverse carbon content, differences in material behaviour could be accounted, therefore, an optimization strategy based on the procedure proposed in [135] to calibrate the J&C material coefficients was introduced. Inverse procedure to determine the cutting parameter to calibrate the model is a frequently used practice. The procedure is based on varying the J&C coefficients within a predefined parameters domain and comparing the calculated results with the experimental ones choosing the coefficients set which give the minimum error percentage between simulated and measured outcomes. As *A* and *B* were the parameters of greatest influence on the flow stress curve, these constants were varied over a range of values and FEM simulations were employed to find the most suitable combination, which was subsequently used to simulate the single grit grinding process. Coefficient *A* was varied over five levels from the reference value of 2480 MPa to -20%, -25%, -30% and -35% of this value. Coefficient *B* was instead varied over three levels from the reference value of 1440 MPa to +20% and +30% of this value, as reported in Table 7.

Table 7. J&C coefficients optimization

| *Levels* | *Coefficient A* | *Coefficient B* |
|---|---|---|
| 1 | 2480 | 1440 |
| 2 | 1984 | 1728 |
| 3 | 1860 | 1872 |
| 4 | 1736 | |
| 5 | 1612 | |

The J&C coefficient combinations proposed for the flow stress optimization plan are shown in Table 8. A simulation plan using the defined grain geometry previously obtained was implemented varying the J&C coefficients A and B as reported to find the coefficients configuration with minimum change between the grinding forces calculated and measured.

Table 8. Johnson & Cook coefficient combinations

| simulation | A | B |
|:---:|:---:|:---:|
| Ref | 2480 | 1440 |
| r1 | 1984 | 1728 |
| r2 | 1984 | 1440 |
| r3 | 1984 | 1872 |
| r4 | 2480 | 1728 |
| r5 | 1736 | 1728 |
| r7 | 1736 | 1440 |
| r8 | 1736 | 1872 |
| r9 | 2480 | 1872 |
| r10 | 1612 | 1728 |
| r11 | 1612 | 1872 |
| r12 | 1612 | 1440 |
| r13 | 1860 | 1440 |
| r14 | 1860 | 1728 |
| r15 | 1860 | 1872 |

The Cockroft-Latham model was used to predict the fracture criterion for chip formation with the material critical value set to 0.22 [134].

## 4.2.3. Simulation data analysis

Calculated grinding forces output data were processed in MATLAB to remove abnormal peak values due to the remeshing phases during calculation and extract the correct values of loads for each rotation. All full grain rotations corresponded to a macroscopic peak in the load curve, while each macroscopic peak was composed of a number of micro-peaks. The resulting value was taken as the average of all micro-peaks within each macro-peak after a data smoothing phase that does not consider the values higher three time the standard variation than the average value.

A representative example is shown in Figure 46, where macroscopic peaks can be seen within the main graph, while micro-peaks can be seen on a shorter timescale within the

red frame. Each micro-peak exhibited typical grain machining behavior comprising rubbing, ploughing and cutting phases. The rubbing phase, due to elastic deformation only, is the shortest and generally results in a negligible effect in terms of contributing to material removal. The ploughing phase, involving both elastic and plastic deformation but without chip removal, plays an important role in the surface formation and energy consumption. The cutting phase, where actual chip formation takes place, involves elastic and plastic deformation as well as chip removal. Since ploughing consumes a lot of energy without directly contributing to material removal, this phase is responsible for the specific energy of grinding being much higher than other cutting processes.

The highest micro-peaks during the ploughing phase were due to the presence of piled-up material at the edges of incisions left from previous passes that the grain encountered during subsequent rotations. This interaction caused automatic remeshing during the simulation. The maximum value was not representative of the whole pass, for which data processing was required to properly analyze the forces peaks to determine the most representative value of load for each rotation.
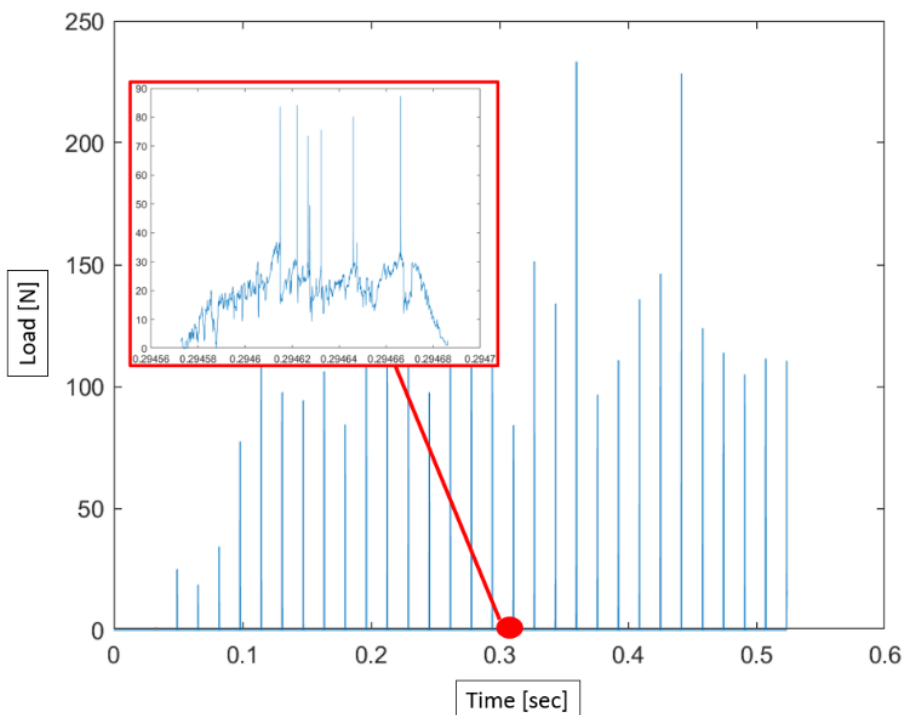


Figure 46. Example of macroscopic and microscopic (red frame) effective stress peaks

Beyond the grinding forces, DEFORM 3D is able to calculate the heat flux due to the thermo-mechanical interaction between the grain and the material during the grinding phase. The heat flux represents the thermal power generated during the process and absorbed by the workpiece. In grinding the main part of the heat generated is absorbed by the workpiece because the chip assumes a very low thickness and the abrasive grain is characterized by a very low thermal conductivity. In Figure 47 it was reported an example of the heat flux calculated in DEFORM 3D and processed in MATLAB in correspondence of the maximum cutting depth. The blue peaks are the original ones detected from DEFORM 3D, instead the orange ones represent the heat flux values considered after the smoothing data phase.
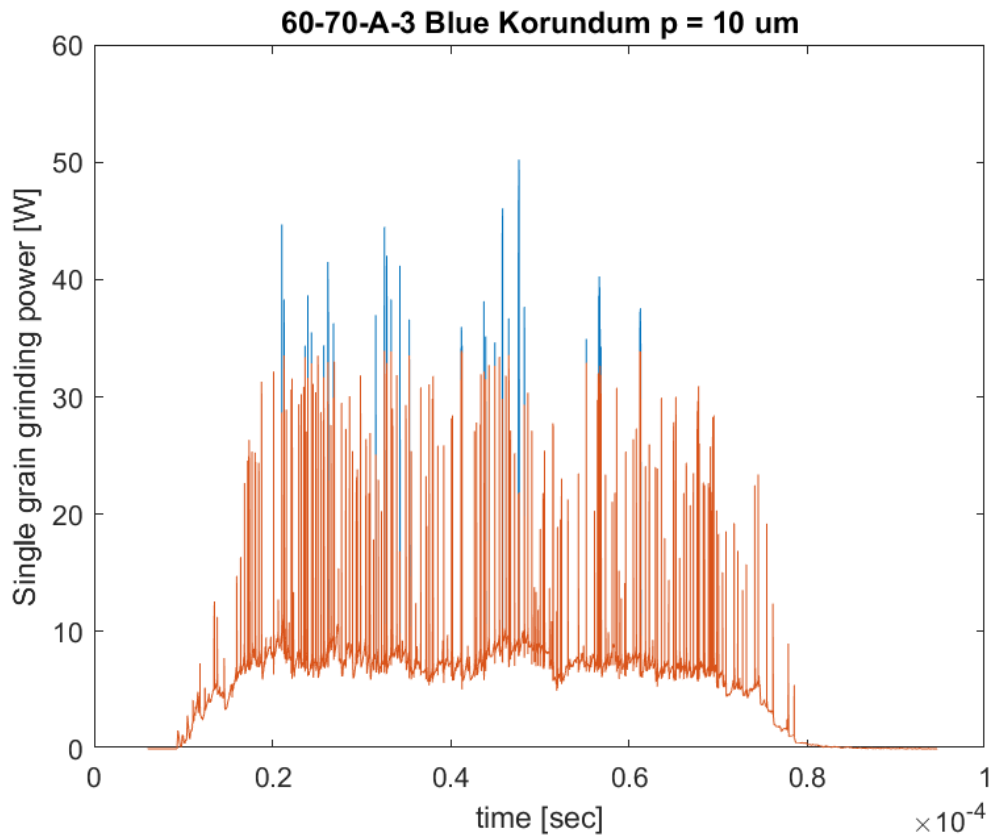


Figure 47. Example of the heat flux calculation and data smoothing

## 4.3. Single grain grinding validation results discussion

## 4.3.1. Single grain experimental results

The main objective of this step was to allow accurate prediction of cutting forces during single grit grinding to calculate the generated single grain thermal power accurately. With this in mind, experimental and simulation outcomes were compared through load calculation. Force signals acquired during experiments with a sampling rate of 10000 Hz are provided in Figure 48 a-b. Normal forces Fx was typically greater than tangential one Fy, while the transversal force Fz is not reported as it was considered negligible. Experimental grinding forces progressively increased with cutting depth during the initial transient phase. The maximum absolute grinding force was generally achieved once the instantaneous center of rotation of the virtual wheel was located above the workpiece edge and a full cut was achieved, after which forces decreased due to grain wear. For the process parameter set related to the fused aluminum oxide abrasives experiments, maximum grinding forces and maximum contact area were therefore expected to be achieved after 0.45 s, corresponding to the $27^{th}$ rotation. Maximum values were in fact achieved shortly after this point due to elastic springback of the material. To check the maximum grinding force value attained for this material and set of process parameters, the minimum required simulation time was therefore 0.5 s from the beginning of the test. Experimental results were taken from a preliminary work [127] and used to check the feasibility of using the equivalent defined grain geometry and the flow stress curve describing case-hardened depth steel.
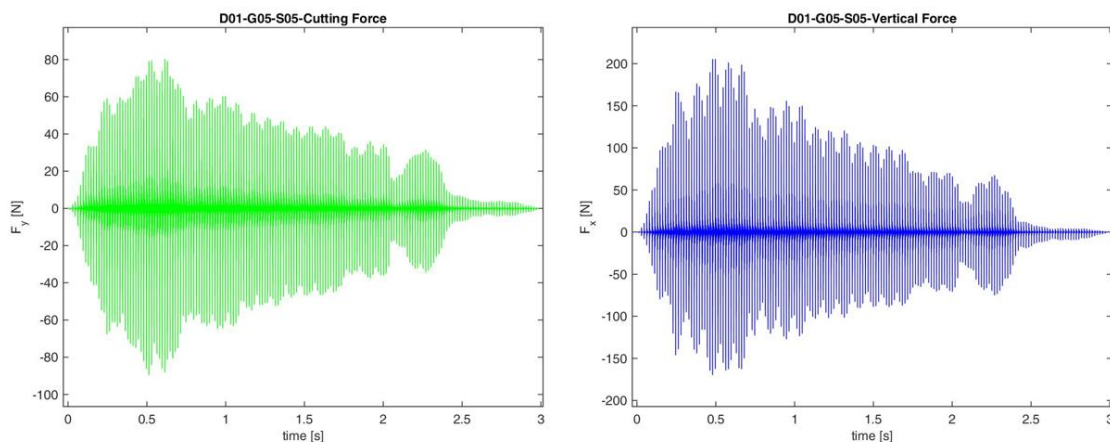


a)
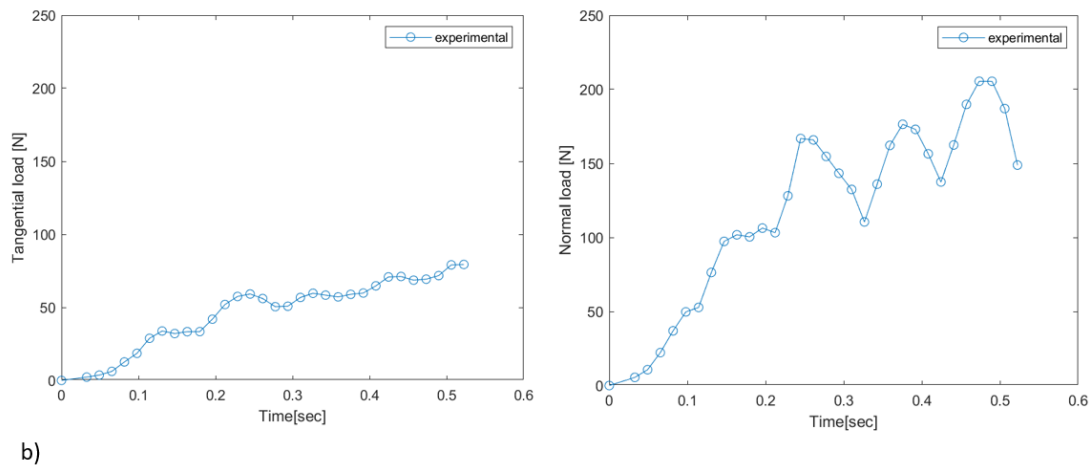
Figure 48. Acquired (a) and Fy and Fx force signals used for simulation comparison (b) for single-grain grinding experiments performed within test step 1 parameters [129]

## 4.3.2. Comparison between real and defined grain simulations

Due to the time-consuming nature of the simulation employing real grain geometry, a faster simulation adopting equivalent defined grain geometry was implemented to compare cutting behavior with the real grain geometry model and verify the calculated forces with experimental data. The nominal contact area was the same for both grain geometries, approximately 0.110 mm$^2$. In Figure 49, information regarding the contact surface is reported. Some differences can be observed in relation to the number of elements and nodes generated by the STL editor software. The real grain geometry contact surface was discretized with 436 elements and 297 nodes, while the defined equivalent grain geometry contact surface was reduced to 52 elements and 44 nodes.
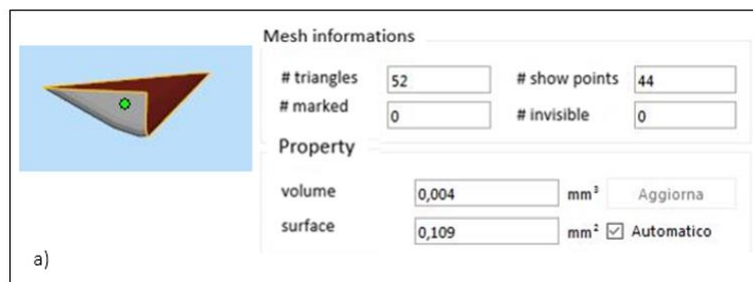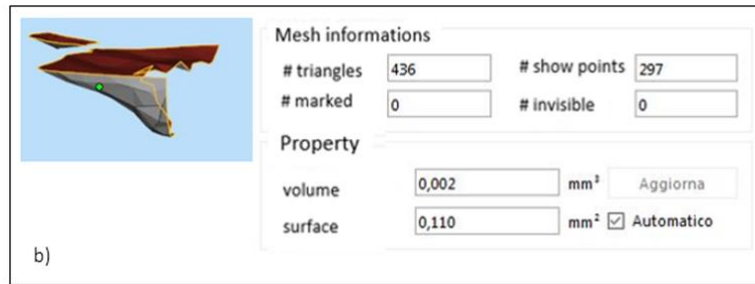
Figure 49. Nominal contact area measurements: a) defined grain geometry; b) real grain geometry [129]

Tangential and normal loads were analyzed to verify whether the cutting behavior of the workpiece was comparable while adopting different grain geometries with the same process parameters. This was confirmed to be the case, with an average percentage difference of 10% up to a processing time of 0.114 s, as shown in Figure 50.

As the grain was modeled as a rigid body with the same portion of material remaining in contact during each rotation, it was, therefore, possible to hypothesize that the trends observed with the defined grain were also achieved with real grain geometry. The equivalent defined grain geometry was therefore considered as representing a valid alternative to the real grain geometry.
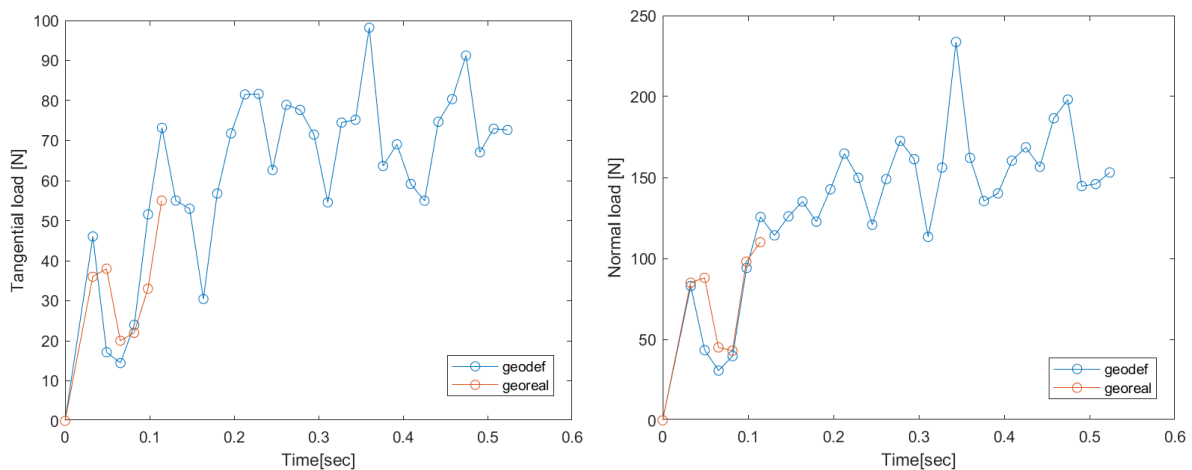


Figure 50. Simulated tangential and normal load trend comparison between real grain and equivalent defined grain geometry with reference flow stress curve

### 4.3.3. Comparison between defined grain and experimental results

Comparison of tangential and normal loads for the simulated defined grain geometry and experimental results is presented in Figure 51. It can be observed that simulated load values were generally overestimated compared to experimental outcomes. This is possibly due to the fact that a suitable constitutive material model had not yet been implemented. The average percentage difference between the calculated defined grain and experimentally determine loads was 25% for tangential forces and 10% for normal forces. Optimization of the flow stress curve was, therefore, necessary to reduce the deviation between simulated and experimental forces.
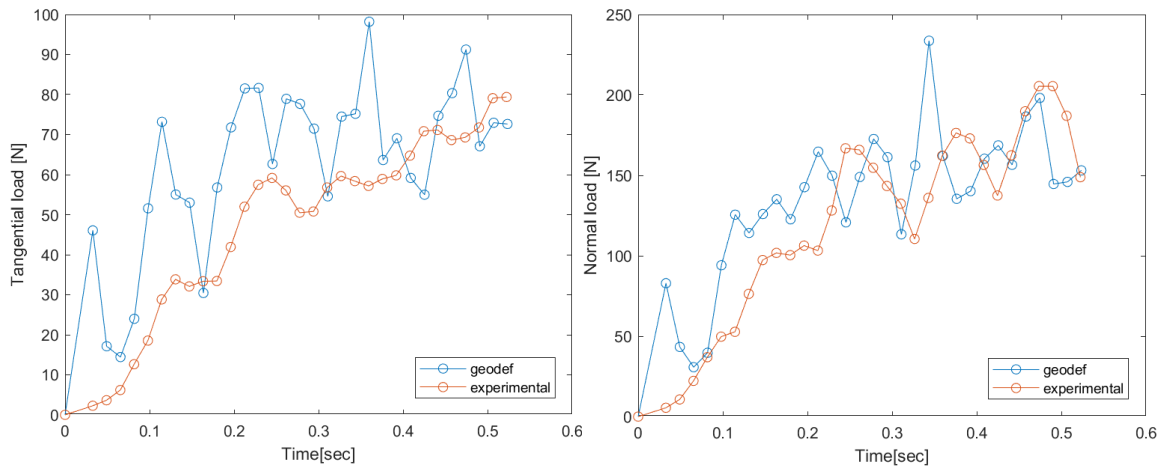


Figure 51. Comparison of tangential and normal loads for simulated equivalent defined grain geometry and experimental results utilizing reference material flow stress curve

### 4.3.4. Flow stress optimization

To deal with this challenge, optimization of the flow stress curve through inverse parameter identification was performed. For the initial set of J&C parameters, values of a reference material from the literature were adopted. Based on the simulation adopting equivalent defined grain geometry, a percentage difference between experimental and simulated outcomes of about 25% in tangential loads and 10% in normal loads was obtained. Therefore, the goal of this phase consisted of finding the J&C parameter set that would offset these percentage differences between the calculated load values and experimental data. To this end, a simulation plan consisting of five levels of parameter *A*

and three levels of parameter *B* was implemented. Comparison between the reference flow stress and proposed combinations of J&C coefficients was considered in terms of percentage differences between calculated loads with the aim at finding the J&C coefficients achieving a reduction in tangential forces of 25% and normal forces of 10%. Percentage differences between the reference simulation, adopting the flow stress of the reference material, and the different J&C coefficient sets are shown for both tangential and normal loads in Figure 52. The blue and orange dotted lines represent the percentage difference targets for tangential (25%) and normal (10%) loads, respectively. The most suitable parameter set was the r2 configuration (Table 8), with values of *A* equal to 1984 MPa and *B* equal to 1440 MPa, achieving percentage reductions of 23.84% and 9.85% compared to the values achieved with the reference coefficients for tangential and normal loads, respectively. A final simulation was therefore implemented with the new flow stress coefficient set (A =1984 MPa; B = 1440 MPa; C = 0,012; n = 0,45; m = 1,1). Good agreement between load values was reached, with average percentage differences of 13% and 3,5% observed for tangential and normal loads, respectively, as shown in Figure 53.
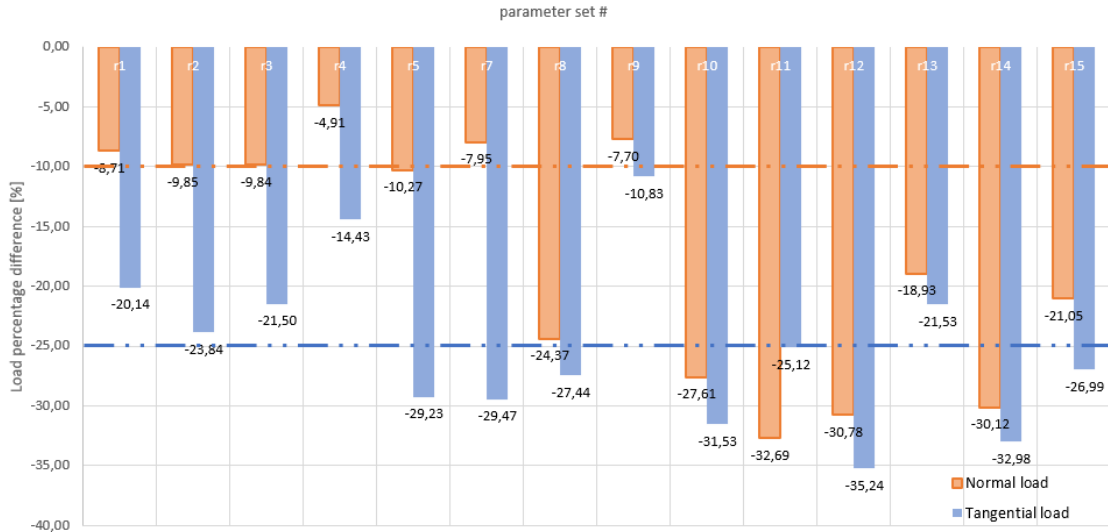


Figure 52. Percentage difference between reference flow stress curve and DoE J&C coefficient sets for tangential and normal load values
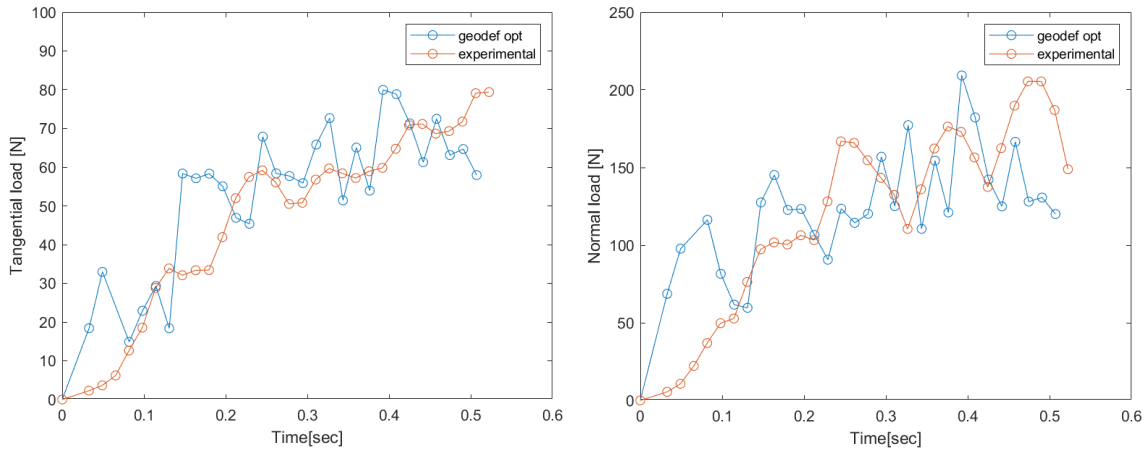
Figure 53. Tangential and normal load trend comparison between experimental and simulated equivalent defined grain geometry with optimized flow stress curve.

## 4.3.5. Single grain grinding model validation

The same procedure was applied to a second single-grit grinding test (G02) to validate the calibrated flow stress curve. The same process parameters were chosen but with another grain having different geometric characteristics and shape, characterized by a rake angle equal to 53°, a tip radius of 0.05 mm, an opening angle of 12° and a total width of 0.55 mm with a contact area of 0.211 mm$^2$. In this case, the grain geometry showed a totally different shape characterized by a double macro-asperity, which denoted a larger contact area despite the reduction of the width grain and shape. After analysis of the real grain geometry, the equivalent defined grain geometry was designed to represent the real contact area between the grain and workpiece. With reference to Figure 54, it is possible to firstly observe that the use of the same process parameters with grains characterized by slightly different geometry leads to different load behavior. Tangential and normal loads were lower than the first test due to the lower rake angle and width, which implies a reduced ploughing effect. Good agreement between experimental and calculated tangential and normal loads was confirmed achieving a maximum percentage difference of 9% and 12% respectively, thus validating the new flow stress curve.
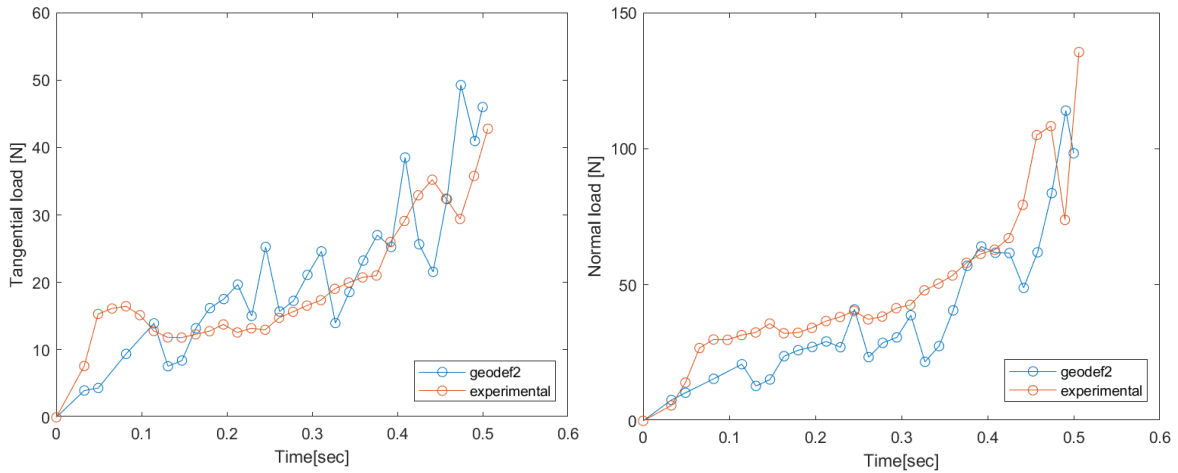
Figure 54. G02 Tangential and normal load trend comparison between experimental and equivalent defined grain geometry simulation results with optimized flow stress curve.

Subsequently, the analysis moved on sintered aluminium oxide abrasives with size 60 which were employed for the single grit grinding test adopting a depth of cut of 0.001 mm. Being the depth of cut very small, a lower variation between the grains geometrical characteristics was expected. A sample of 15 elements was considered, some of them were reported in Figure 55. Also in this case, the characteristic properties identifying an abrasive geometry, as the width, the length, the rake angle and the tip radius were detected and statistically analyzed to design an equivalent defined grain shape representative for the whole grain material and size class. In Figure 56, the frequency with which the abrasives geometrical features were verified in the statistical analysis was reported. Therefore, the equivalent defined grain geometry for the sintered aluminum oxide size 60 was modeled with a rake angle of 68°, a tip radius of 0,1 mm and a global length and width equal to 0,55 and 0,6 mm, respectively.
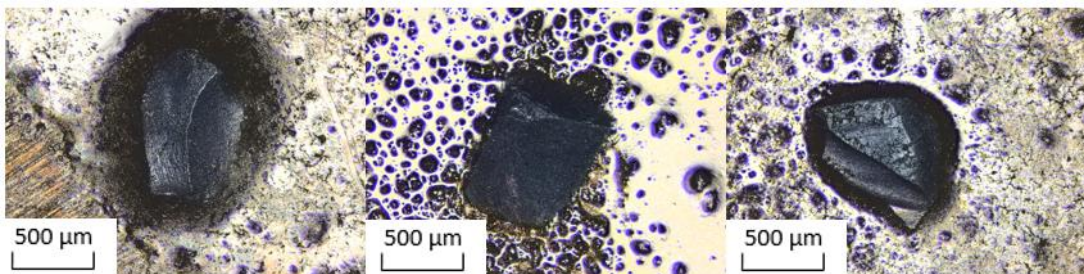


Figure 55. Fused aluminium oxide abrasives acquired
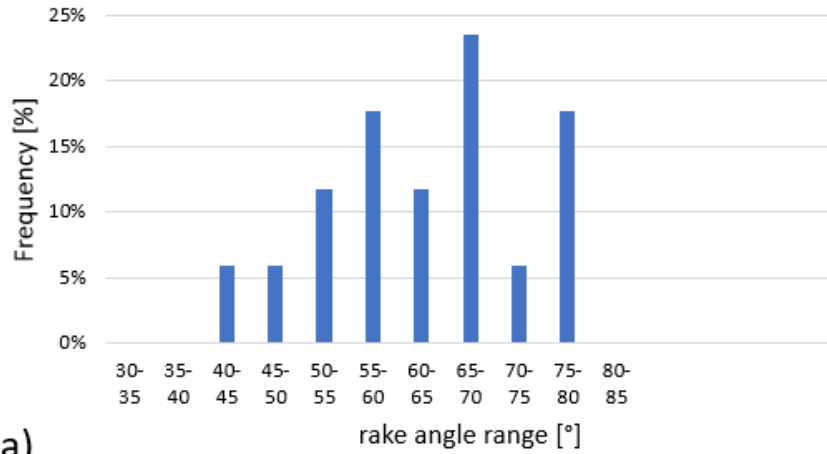
a)



b)



c)

d)
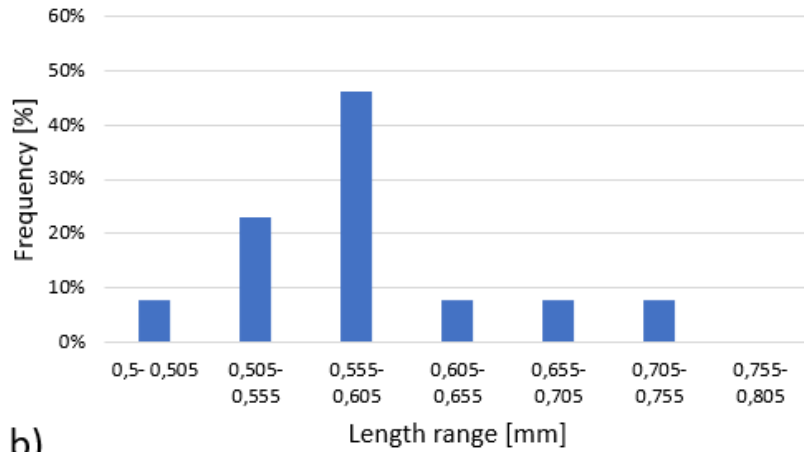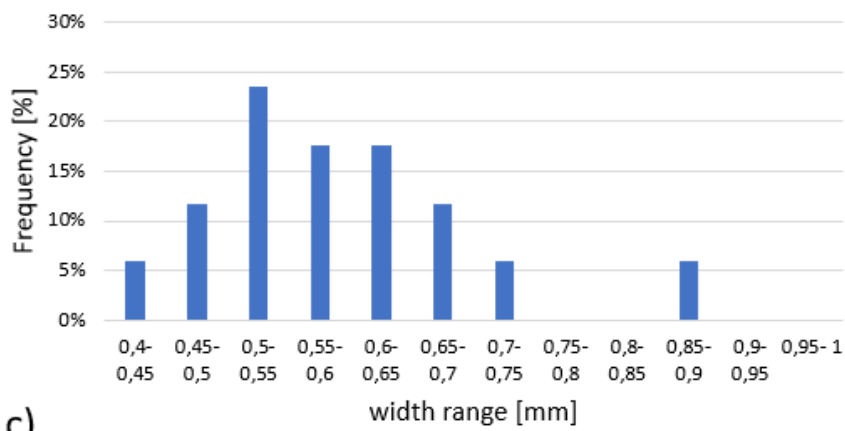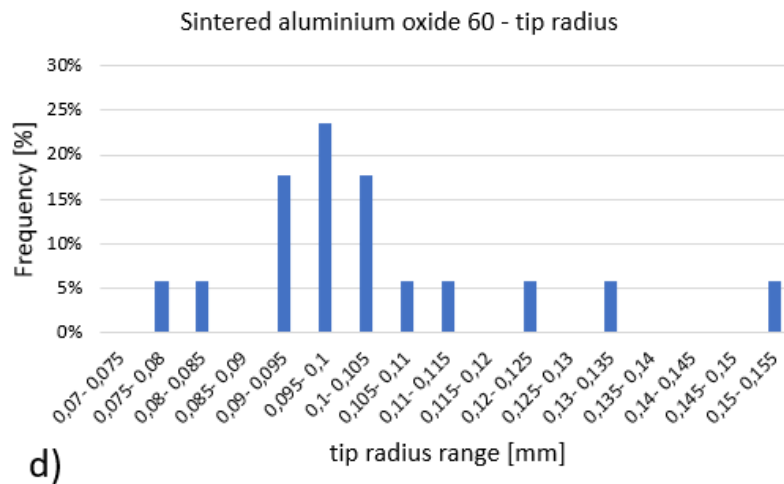
Figure 56. Equivalent defined grain geometry: a) rake angle; b) length; c) width; d) tip radius statistical analysis

A further simulation was developed using the optimized geometry for sintered aluminium oxide adopting the process parameters of the test step 2 reported in Table 4. The model was further validated by comparing the measured and calculated tangential and normal grinding forces. Good agreement was achieved again with a maximum percentage error of 8% for the tangential load, as reported in Figure 57. In this case, only the maximum forces obtained when the single grit reached the maximum depth of cut during the pass were reported in the forces' comparison.
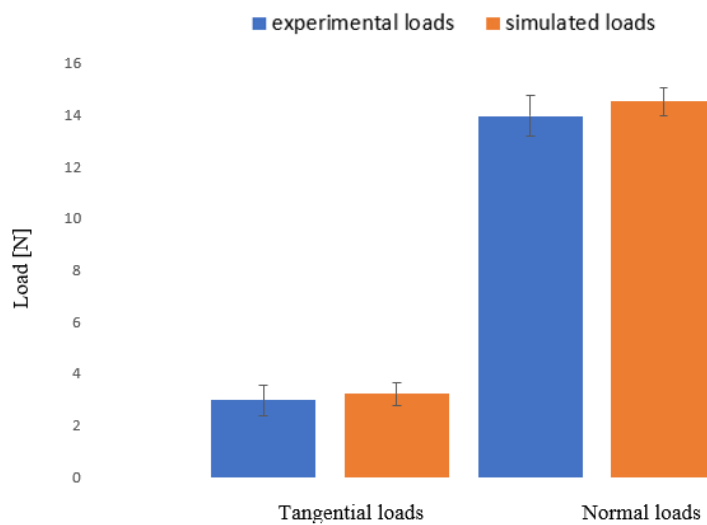


Figure 57. Single grit model validation with sintered aluminium oxide abrasive

After the single grain model validation for both fused and sintered aluminium oxide abrasives, a simulation plan varying the depth of cut ($p$ = 10 - 25 - 50 µm) and feed rate values ($f$ = 10 - 20 - 40 mm/s) was developed using a fixed value of cutting speed ($vt$ = 20 m/s) according with the following tangential grinding tests which used sintered aluminium oxide grinding wheels. The aim of the single grit model focused on the single grain grinding thermal power calculation. It contributes to the design of the moving heat source representing the grinding wheel pass on the material, as explained in the following chapter. In Figure 58 the single grain grinding thermal power calculation developed in DEFORM 3D was reported in function of the depth of cut and feed rate. The most influencing process parameter is represented by the depth of cut, indeed, a steep increase is visible increasing it. The feed rate influence is lower in terms of single grain power generation, indeed, a negligible increase was reported increasing the feed rate values.
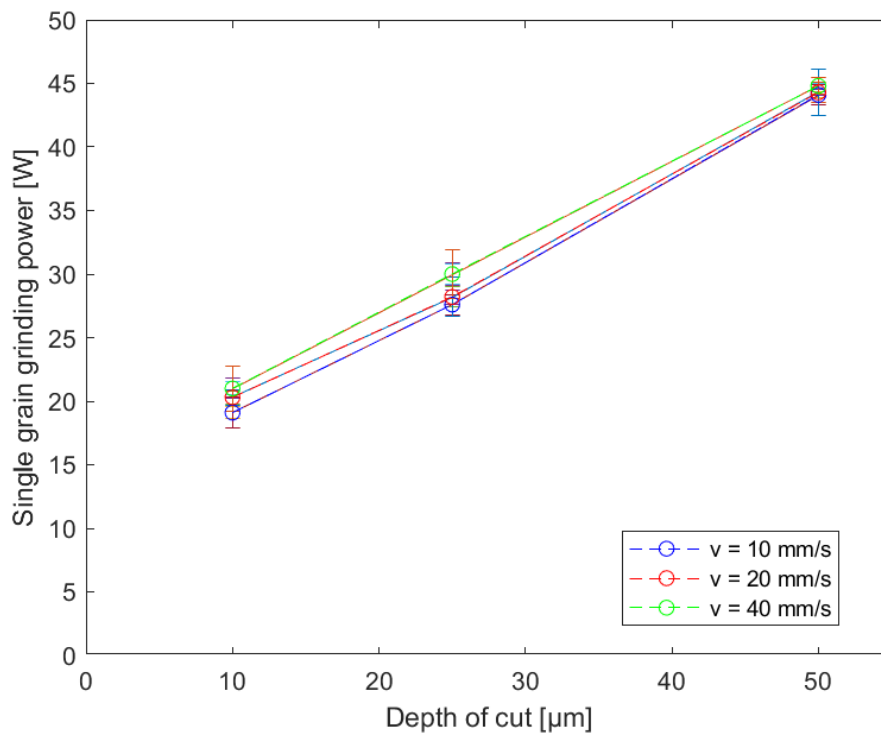


Figure 58. Single grain grinding power calculation

The following chapter will present the second part of the model. The thermal model is based on the single grain thermal power calculation of this previous step and considers the process parameters and the grinding wheel specification through an analytical and experimental approach.

# Chapter 5

## Tangential grinding thermal modelling and experimental validation

In this chapter, the second step of the proposed grinding model will be presented. Before the thermal model and experimental procedure description, the attention will be focused on the grinding wheel specification analysis. An analytical approach was correlated with an experimental observation of the actual grinding wheels to estimate the specific number of grains involved in the grinding process. The grains density was used as a direct indication of the grinding wheel propensity to generate more or less heat during dry grinding. Therefore, a new method for estimating thermal damage considering the kinematic parameters and the grinding wheels specifications without first measuring grinding power is proposed in this research and was possible thanks to the combination of the micro and macroscopic approaches.

The thermal model was described with particular attention on the moving heat source design. It represents the interaction between the grinding wheel and the workpiece and was defined starting from the grains' density and the single grain thermal power calculated by the previous step model.

To validate the first step of the model, single grain grinding tests and forces measurements were performed before and were presented in the previous chapter. Instead, the thermal model was directly validated by performing tangential grinding experiments and temperature measurements. Calculated and measured temperatures were compared to evaluate and predict the dry grinding process temperatures reached by varying the kinematic parameters and the grinding wheel specifications. Case-hardened steel, which is commonly used in automotive gears, was used as the workpiece material. Sintered aluminium oxide grinding wheels with size 60 and different porosity and binder hardness specifications were used. The wheels were experimentally analysed through image processing observations correlated with an analytical approach before the grinding tests. The main aim of the model is, indeed, to predict the influence of the kinematic parameters and also the wheels' porosity and binder hardness on the ground material in

dry conditions on a case-hardened steel. To confirm the grinding burns occurrence, microstructural and micro-hardness analyses were undertaken.

## 5.1. Tangential grinding experimental tests

### 5.1.1. Experimental set up

Tangential grinding tests were conducted using the grinding wheel specifications listed in Table 9 on a CN Linea Iron 06.3 grinding machine (Figure 59). The experiment was carried out in dry conditions, with process parameters according with the single grain grinding and thermal simulations plans. Table 10 shows the process parameters that were used.



Figure 59. Tangential grinding tests configuration

Grinding wheel diameter was equal to 300 mm with a width of 50 mm, larger than the samples ground. The comparison on the grinding tests outcomes takes place at equal other conditions between three wheels with increasing porosity (J6, J9 and J12) and two grinding wheels with two different binder hardness (J9 and H9). Prismatic case-hardened steel samples with global dimensions of 20x50x15 mm were used for the experiments.

Table 9. Grinding wheel specifications

| Grinding wheel designation | Grain material | Grain size | structure | Binder hardness | Binder material |
|---|---|---|---|---|---|
| SG60 J6 VS3 | Fused aluminum oxide | 60 | 6 (medium) | J (medium) | Vitrified |
| SG60 J9 VS3 | Fused aluminum oxide | 60 | 9 (open) | J (medium) | Vitrified |
| SG60 J12 VS3 | Fused aluminum oxide | 60 | 12 (porous) | J (medium) | Vitrified |
| SG60 H9 VS3 | Fused aluminum oxide | 60 | 9 (open) | H (soft) | Vitrified |

Table 10. Tangential grinding tests process parameters

| Cutting speed $v_t$ [m/s] | Feed rate $f$ [mm/s] | Depth of cut $p$ [mm] | Grinding mode |
|---|---|---|---|
| 20 | 10 | 0.01 | Up-grinding |
| | 20 | 0.025 | |
| | 40 | 0.05 | |

The specimens were previously case-hardened to reach a hardness of 750 HV1 in the surface layer up to 1 mm in depth as typical for gears heat treatment. On each sample 9 grooves with a width of 1 mm were obtained for the thermocouples positioning (Figure 60).
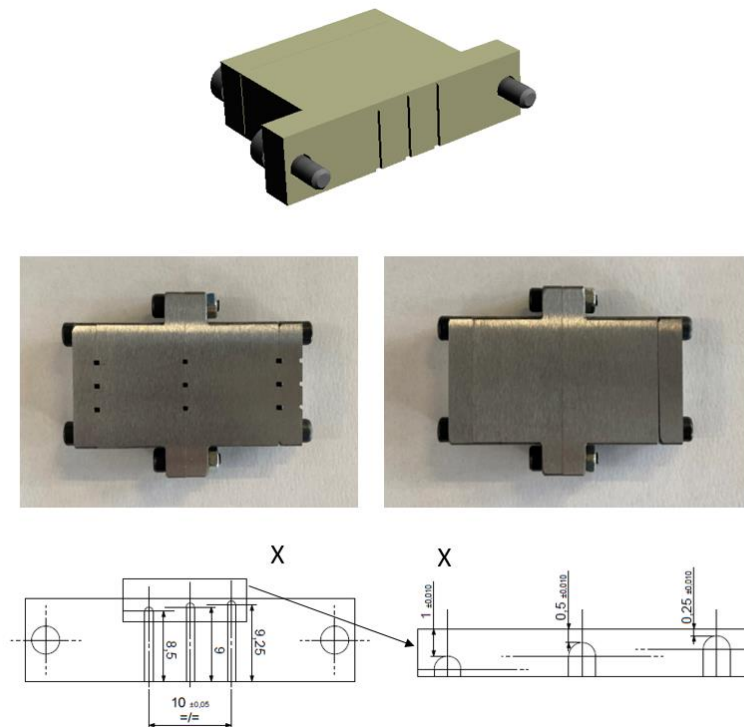


Figure 60. Tangential grinding tests sample geometry

## 5.1.2. Temperature acquisitions

In general, there are two measuring methods to measure the grinding temperature: direct contact measurement and non-contact measurement. Although grinding temperature measurements need to be further investigated, thermocouples and infrared measurements represent two reliable methods [136]–[138]. Infrared measurements present some limitations yet due to the necessity to correctly set the camera position that is not always feasible. Moreover, this kind of system record indistinctly the flash temperature given by the swarf which reach the highest temperature during the process invalidating the measure. Therefore, when the process kinematic allows it, the most reliable method involves the use of thermocouples. Also, this approach can present some limits due to the limited contact time between grinding wheel and workpiece. So, it is required a measuring system with low thermal inertia. Moreover, increasing the wheel feed rate the contact time decreases further, while the temperature gradient increases in the sublayer of the ground surface, requiring a positioning of the thermocouples very close to the surface [139], [140]. Indeed, in this case, the thermocouples were chosen with the minimum wire diameter possible and were placed in proximity of the ground surface, at a distance from the surface equal to 0.25, 0.5, and 1 mm, at three separate portions of the sample: at the beginning, middle, and end of the sample, in specifically at 5, 25, and 45 mm from the specimen's starting edge. The precision in the positioning was guaranteed by the milled grooves obtained with a CNC milling machine and the use of a thermal conductive paste that facilitated the application of the thermocouple. The entire sample was made up of four sections that were screwed together. The temperature during the grinding wheel pass was measured using thermocouples type K in Inconel with a diameter of 0.25 mm and a maximum temperature acquisition of 1100°C. Before each grinding test, each sample was ground with a total depth of cut of 0,1 mm to ensure surface planarity. Every three tests, the grinding wheel was dressed.

## 5.1.3. Microstructural and micro-hardness analysis

Microstructural analysis and micro-hardness measurements were provided to verify the effect of the grinding process on the samples and validate the model. Microstructural

analysis was carried out on each section in correspondence of the thermocouples position with an optical microscope Zeiss Axio Vert.A1M on the samples prepared according to standard metallographic techniques comprising mechanical grinding (80-2400 grit paper) and polishing with alumina in suspension down to a particle size of 1 μm. In order to reveal microstructural features, the samples were etched using Nital reagent for 3 s. Vickers micro-hardness tests were performed using a load of 1000 g for 20 s towards the hardened depth with indents spaced of 100 μm.

## 5.2. Grinding wheel specification analysis

Although a number of studies have been focused on the evaluation of grinding wheels' properties [141], [142], only a few have concentrated on the prediction of the thermal effect based on the wheel's specification. Habrat measured the tangential and normal stresses to determine the effect of the bond material in diamond wheels on cemented carbide [143]. Zhao et al. studied the effect of pore structure and distribution on the flexural strength of porous Cu-Sn-Ti alumina composites, finding that bigger pore sizes and greater pore concentrations reduce the composite strength while simultaneously providing more space for chip formation [144]. Using image processing, Gopan et al. developed a quantitative study of grinding wheel loading [145]. Other approaches consider the grinding wheel properties starting from the single grain analysis. Zahedi et al. introduced the wheel topography starting from the single grain grinding simulation amplifying its effect through a probability distribution function to calculate the process forces [146]. Denkena et al. used a single grain tool to analyse the grinding wheel manufacturing process and evaluate the mechanical interaction at the grain/bond interface [139]. Hecker et al. use a micro scale approach to deal with the stochastic nature of abrasive grains. Grinding force and power predictive modelling are frequently based on the probabilistic distribution of undeformed chip thickness as a function of kinematic conditions, material properties, and wheel microstructure [147], [148]. Force modelling was built for each grain by deducing the dynamic grain density from the static grain density and taking into account kinematic factors such as active grain shadows and dynamic effects owing to local grain deflection. Klocke et al. used a kinematic modeling approach, with a statistical analysis of the grain shape taking into account the apex angle,

rake, wedge angle, and opening angle. This was followed by the creation of a database of abrasive grains mathematically designed taking grains, bond, and pores volumetric fraction into account [149].

In this work, the grinding wheel specification was incorporated as grains density in the heat source design, and it was obtained by a combination of analytical and experimental assessment. The average number of grains per mm$^2$ was estimated by considering both the wheel porosity and the binder hardness. For the grains number calculation the considerations reported in [150], [151] were adapted and resumed as follows. The effective number of grains $n_a$ which is involved in the grinding removal mechanism could be determined as a fraction $\varphi_a$ of the approximated static grain quantity $n$.

$$n_a = \varphi_a n \quad (17)$$

The total number of static grains can be estimated starting from the volumetric concentration of abrasive grains $V_g$ in the wheel through the following Eq. (18):

$$n = 6 V_g \frac{l_c b}{\pi d_g^2} \quad (18)$$

Where $d_g$ is the abrasive mean diameter that for a FEPA size of 60 is equal to 0.25 mm, $l_c$ is the theoretical contact area and $b$ is the workpiece sample. The volumetric concentration of abrasive grains $V_g$ could be expressed through the following Eq. (19):

$$V_g = \frac{2\,(32-S)}{100} \quad (19)$$

Where $S$ is the wheel structure number. For the calculation of the active grains number, the volumetric concentration of binder $V_b$ and pores $V_p$ were introduced as:

$$V_b = 1 - (V_g + V_p) \quad (20)$$

$$V_p = \frac{1}{100}\left(45 + \frac{S-2i}{1.5}\right) \quad (21)$$

Where $i$ is an integer ($i = 1, 2, 3, 4...$) corresponding to the binder hardness letter (E, F, G, H..) respectively. The fraction of active grains $\varphi_a$ can be determined by introducing a normalizing factor $nf$ and a reference fraction coefficient $\varphi_{ref}$.

$$nf = 20{,}535\, V_b - 0{,}217 \quad (22)$$

$$\varphi_a = \varphi_{ref} \, nf \quad (23)$$

The reference fraction coefficient $\varphi_{ref}$ is normally calculated empirically based on the wheel specification and considers the actual contacting grains encountered during the pass. The reference fraction coefficient $\varphi_{ref}$ was established in this study by assessing the grinding wheel specifications using image processing [152] and MATLAB to provide an empirically verified indicator of the effective grains number that are likely in contact with the material. A stereomicroscope Zeiss Stemi 508 was used to examine the grinding wheel, with samples of 1 mm$^2$ of the entire wheel area being evaluated at a magnification of 2x. The porosity was varied between 6, 9, and 12 structure numbers, reflecting increasing porosity presence in the wheel; instead, the binder hardness chosen were J and H, so that a medium and softer wheel were tested. Ten acquisitions were made over the entire wheel. The grinding wheel specifications are listed in Table 9.

## 5.3. Tangential grinding thermal model description

A macro-scale FEM thermal model created in COMSOL MULTIPHYSICS version 5.4 was used to calculate the thermal contact between a cylindrical grinding wheel and the sample. The thermal model aimed at calculating and predicting the process temperature generated during the actual grinding process in dry conditions. The thermal interaction between the material and the wheel was modeled as a moving heat source, with a heat flux value spread in the contact region determined directly from the single grain thermal power calculation. The heat source could be described by the following features:

- Amplitude, which depends on the process parameters and the wheel specification.
- Distribution, which depends on the process thermo-mechanical action.
- Shape and dimensions, which depends on the wheel-workpiece contact area.
- Motion, depending on the process kinematics.

Considering the shape and the motion, the heat source was rectangular in shape in the x-y plane and assumed a translational speed equal to the feed rate value used during the tangential grinding tests (Figure 61).
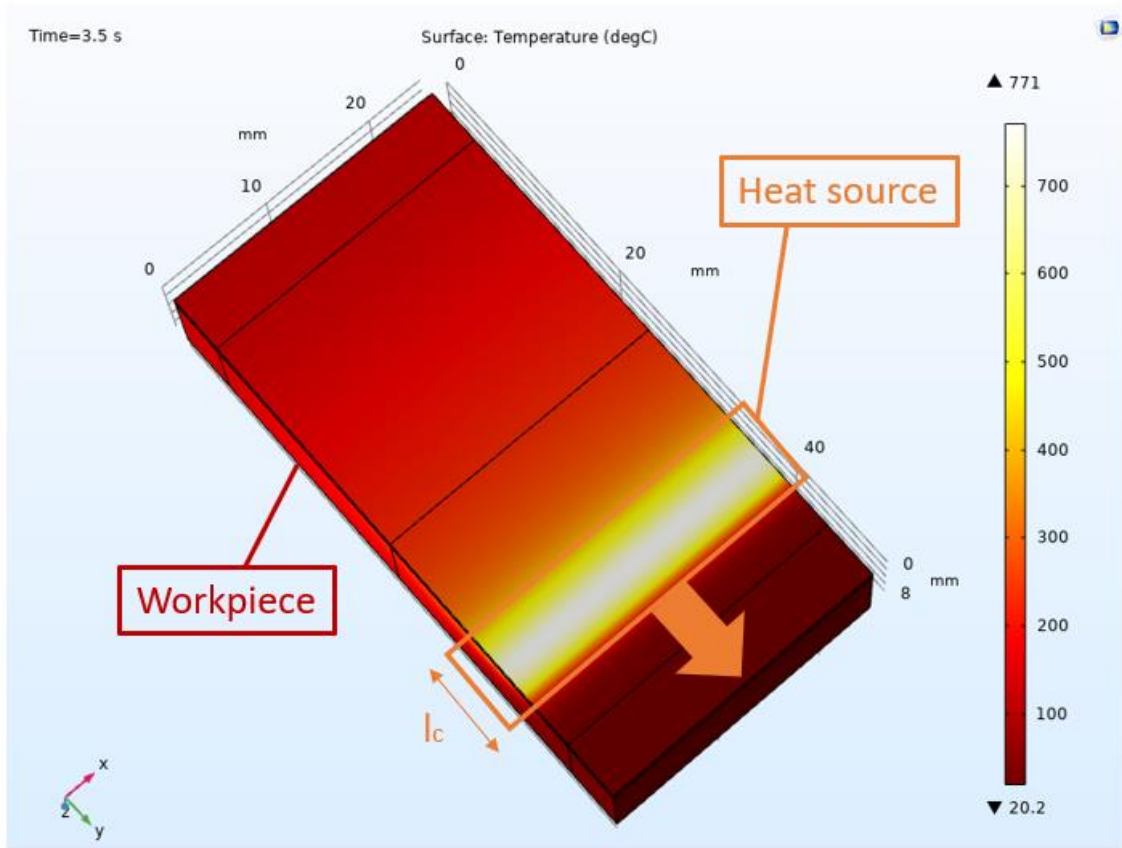
Figure 61. Grinding thermal model configuration and temperatures calculation

The heat source dimensions are equal to the sample width and the theoretical contact length $lc$ calculated through Eq. (24), where $dw$ is the grinding wheel diameter and $p$ the depth of cut.

$$lc = \sqrt{p \cdot dw} \quad (24)$$

The grinding-induced thermal cycle is a fast-heating process that could be compared to a laser hardening process. Therefore, the heat source distribution was modelled with an Erf function representing an asymmetrical top-hat intensity distribution in the y-z plane (Figure 62), as reported in Eq. (25), where A and B are the contact area dimensions and a and b define the rate of decrease in power density from the maximum value to zero [153].

$$\text{distr} = \frac{1}{4}\left[\text{Erf}\left(\frac{A-2x}{2a\sqrt{2}}\right) + \text{Erf}\left(\frac{A+2x}{2a\sqrt{2}}\right)\right] \cdot \left[\text{Erf}\left(\frac{B-2y}{2b\sqrt{2}}\right) + \text{Erf}\left(\frac{B+2y}{2b\sqrt{2}}\right)\right] \quad (25)$$

In this case, *a* and *b* were set equal to 0,1 and 0,6 respectively.
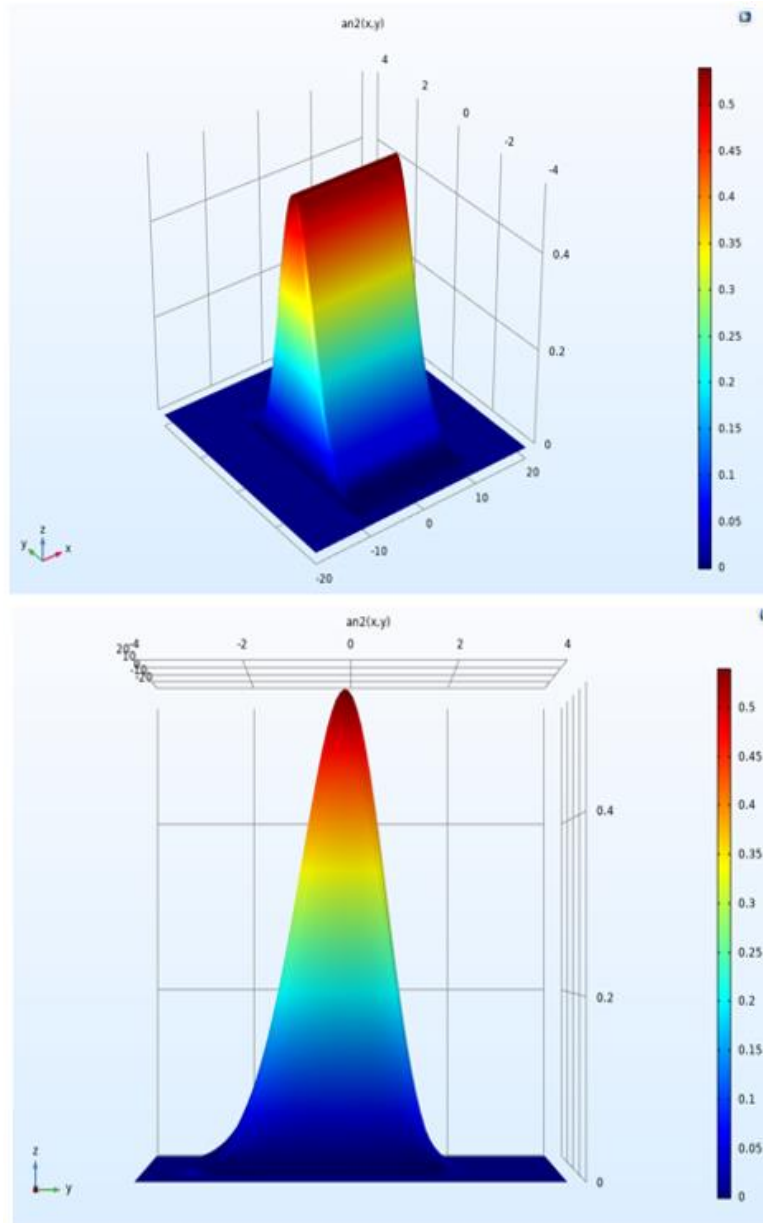


Figure 62. Moving heat source definition for the tangential grinding thermal model

The heat source amplitude was modelled considering the single grain grinding power *Psg* obtained from the previous single grain grinding model. The power per grain *P*, which represents the heat generated by a single grain during the whole pass and absorbed by the material, was calculated by multiplying the single grinding power *Psg* with the

grain–workpiece contact area *Ssgt* encountered in the motion direction and by dividing by the total contact area *Ssgn* left after an entire pass, as calculated through Eq. (26):

$$P = \frac{P_{sg} \cdot S_{sgt}}{S_{sgn}} \quad (26)$$

The grain-workpiece contact area *Ssgt* was calculated as the frontal contact area of a sphere having dimensions corresponding to the nominal mean abrasive grain size with the workpiece surface at the chosen depth of cut [127] and represents the region where the main part of the heat, as usual in a cutting process, is generated and absorbed by the workpiece. The idea that the mean grain diameter should be used derives from the fact that the mean grain size is the most common, whereas the maximum and minimum grain diameters are uncommon [154]. The total contact area *Ssgn* was determined by the kinematic process parameters set and represent the total contact area generated in a full pass on which the heat exchange takes place. In Figure 63 a representation of the before mentioned contact areas was shown.
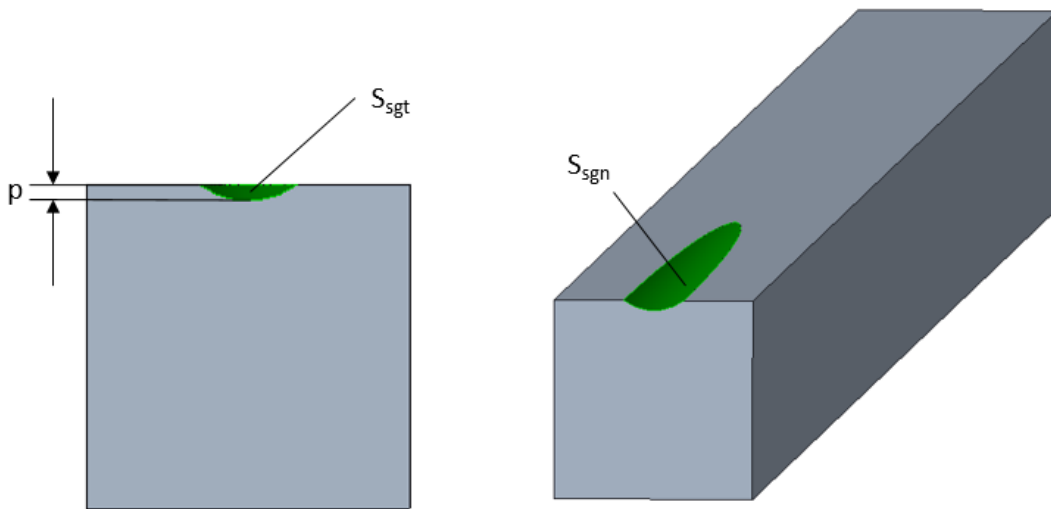


Figure 63. Single grain tangential and normal contact area during the pass with a depth of cut p

The heat source entity was then calculated using Eq. 27 by multiplying the power per grain P by the specific number of grains $n_g$ present in 1 mm². The process for calculating the number of grains was detailed in the previous section.

$$I = P \cdot n_g \quad (27)$$

The workpiece was discretized with free tetrahedral elements with a dimension of 250 μm in the surface depth and 1 mm in the bulk material. The total number of workpiece elements and nodes was 1399293 and 250228, respectively. The surface depth thickness was considered equal to 1 mm. The model used a constant time-step of 10 milliseconds. According to the single grain grinding model and tangential experiments, the simulation plan was built with the same process parameters. A convection heat transfer coefficient of 15 W/m$^2$K was introduced. In Figure 64 the moving heat source shape was reported as isothermal curve at the beginning, in the middle and at the end of the grinding pass. It was shown how the heat source is distributed on the surface in three different grinding pass moments and how the heat is conducted in the bulk material. It is visible how the temperature reaches the highest temperatures in the surface and quickly decrease over the case-hardened depth. This phenomenon is more highlighted at the beginning of the pass, instead, after reaching the regime, the workpiece begins to heat up and temperatures slightly increase.



a)
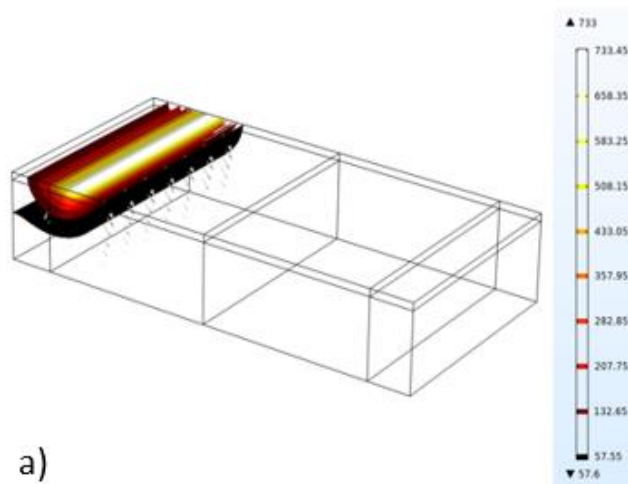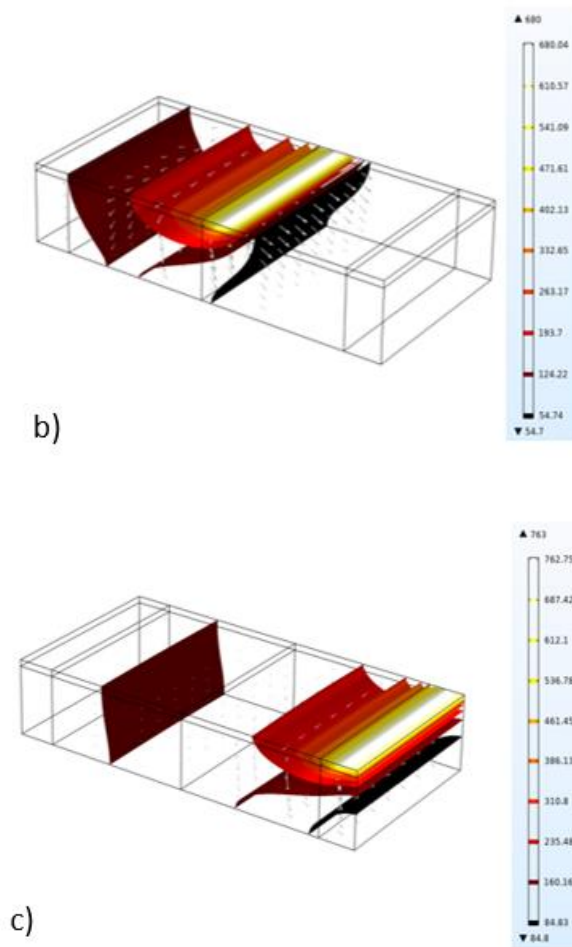
Figure 64. Isothermal curve representing the moving heat source for the tangential grinding thermal model a) at the beginning; b) in the middle and c) at the end of the wheel pass

Material assigned to the assembled sample was a case-hardened steel, with a variation in the thermal conductivity law of the surface up to 1 mm in depth because of the martensite structure. Thermal conductivity values of the surface depth were reported in the Table 11 in function of the temperature [155].

Table 11. Martensite and austenite thermal conductivity varying with the temperature

| Temperature [°C] | 0 | 300 | 600 | 800 |
|---|---|---|---|---|
| Austenite thermal conductivity k [W/m K] | 15 | 18 | 21.7 | 25.1 |
| Martensite thermal conductivity k [W/m K] | 43.1 | 36.7 | 30.1 | |

Thermal probes were introduced at the beginning, in the middle and at the end of the sample, as the real experiments, at a distance 0.25, 0.5 and 0,1 mm from the surface.

## 5.4. Tangential grinding tests validation results discussion

The single grain power calculation was correlated with the grains' density evaluation, being the heat source entity depending on this main factors. As a starting point, an analytical approximation was established to calculate the number of grains in contact with the material in a specific time step. This approach was followed by an experimental visual inspection of the grinding wheel correlated with its image processing to effectively show the percentage of grains compared with the voids. In Figure 65, an example of the wheel surface acquisition was presented and compared to the MATLAB processed picture findings. Increasing the wheel porosity of one order, an average decrease of 5.5 % in terms of grains number was detected. In the following image, the wheel acquisition and image processing of three different porosity levels was shown. In particular, the wheel represented by a porosity of 6, 9 and 12 were reported. The white region indicates the presence of grains, instead all the black parts represent the voids among the grains. It is visible an effectively increase of porosity going from a porosity of 6 to 12.
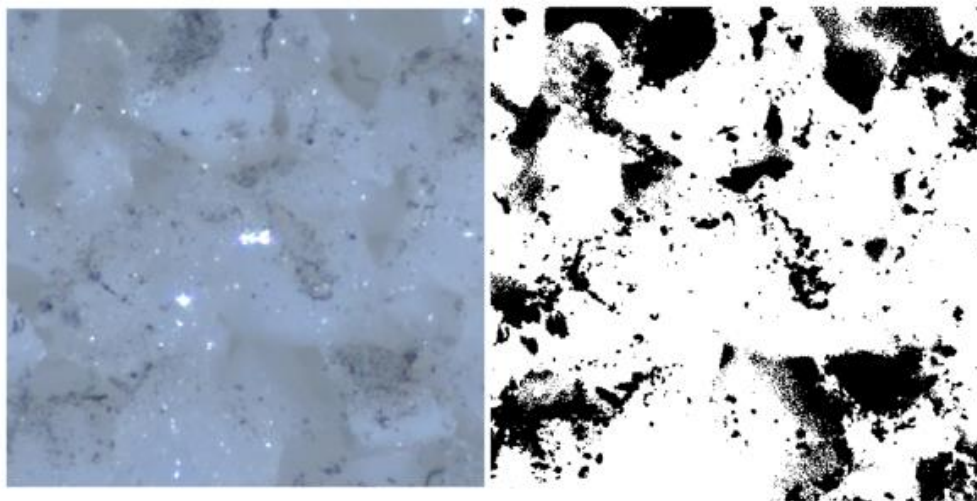


| Wheel structure | 6 |
| --- | --- |
| Effective grain percentage | 73% |

a)
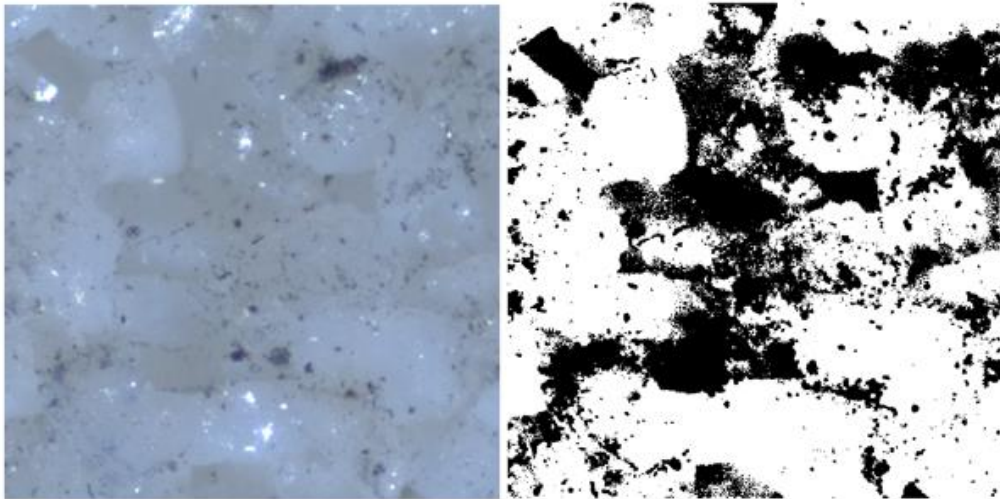
| Wheel structure | 9 |
|---|---|
| Effective grain percentage | 67% |

b)
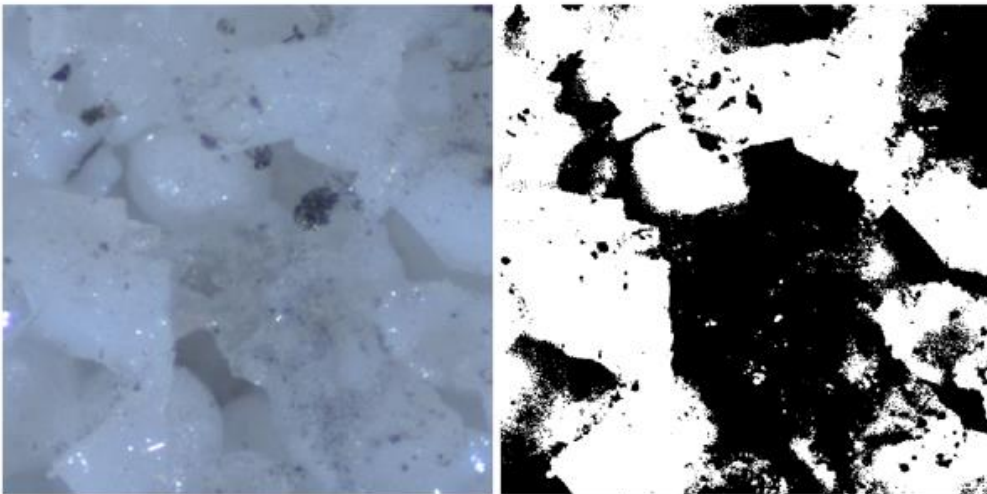


| Wheel structure | 12 |
|---|---|
| Effective grain percentage | 62% |

c)

Figure 65. Grinding wheel specifications evaluation: structure a) 6; b) 9 and c) 12

The number of grains distributed in 1 mm$^2$ decreases as porosity increases, hence an increase in porosity effectively reduces the grinding power contribution. Indeed, the higher the porosity the greater the probability of dissipating heat.

Concerning the wheel binder hardness, it was indirectly identified by the number of grains because it is known that its influence affects the grain self-sharpening and not their distribution. Anyway, through the visual inspection it was noticed that the grains density of the wheel with the softer binder (H9) was similar to that related to the grinding wheel with the same porosity (J9). In Figure 66 the grains density of the wheel with softer binder hardness was shown in comparison with its processed image.



| Wheel structure | 9 |
| Wheel binder grade | H |
| Effective grain percentage | 66% |
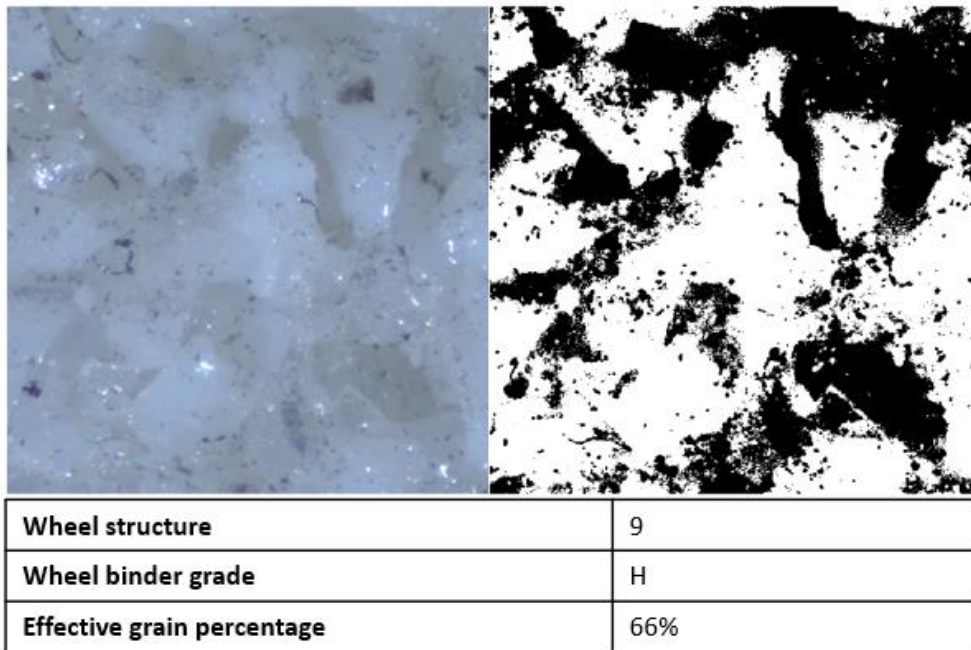
Figure 66. Grinding wheel specifications evaluation: structure 9, binder grade H

The process parameters and the number of grains per mm$^2$ on the wheel were used to determine the grinding power. Figure 67 shows the evaluation of grains per mm$^2$ as a function of wheel specification. The grains' density reported in the following graph takes in consideration both the analytical and the empirical observation, as explained before.
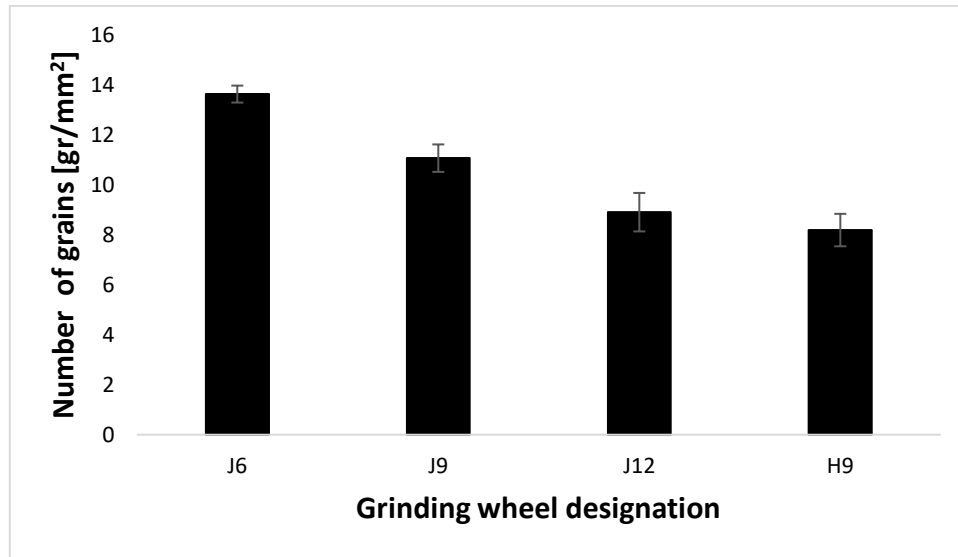
Figure 67. Grinding wheel grains density in function of the specification

Through the approach proposed in this work, at equal structure, a decrease in binder hardness led to an apparent decrease of grains distribution on the wheel surface. Indeed, a softer binder reduces the grinding action in terms of thermal effect, therefore, this effect was identified with a decrease in the grinding heat source entity.

The thermal effect of the different wheel specifications was reported in terms of temperature reached in the sample depth and surface microstructural modification. For all process parameter configurations and grinding wheel specifications, the temperature was measured and computed. Considering the experimental temperature acquisitions, for each grinding configuration the temperature was acquired at three different distances from the surface ($d$ = 250, 500 and 1000 µm) at different points during the grinding pass ($L$ = 5, 25 and 45 mm). In Figure 68 an example of temperature acquisition during a tangential grinding test was reported.
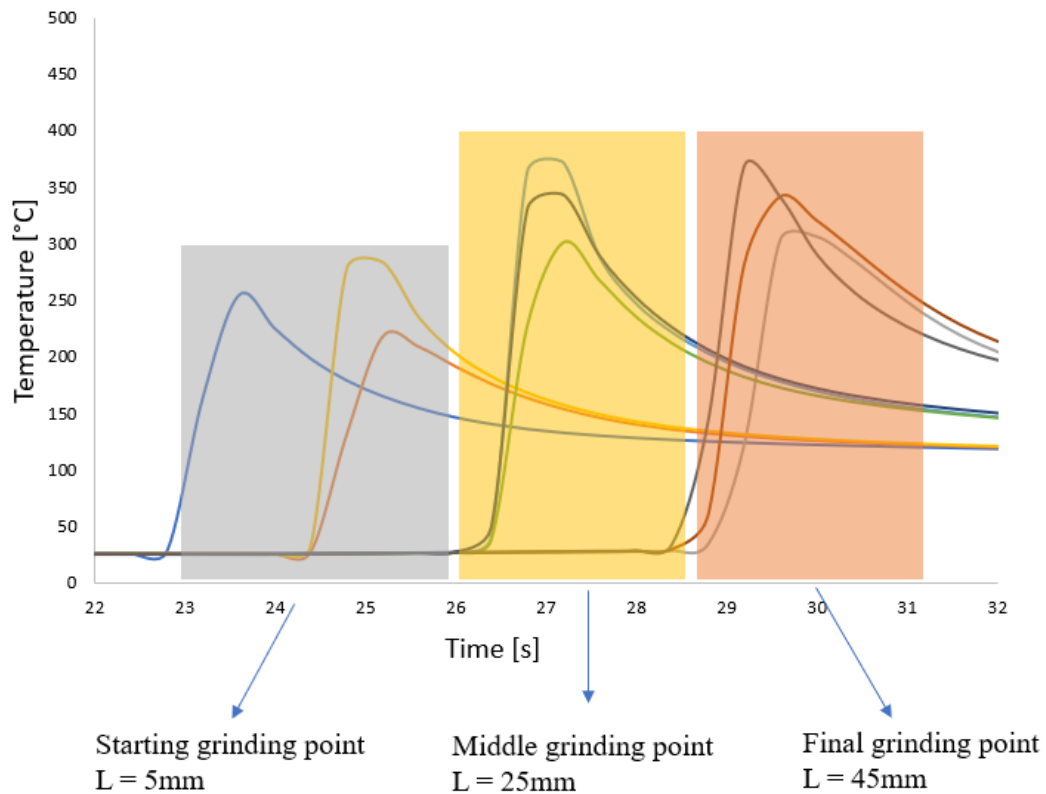
Figure 68. Example of temperature acquisition in a tangential grinding test

It is possible to observe that the initial acquisition at the grinding starting point shows lower temperature values compared to the middle and the final grinding points. This is since at the initial point the global workpiece temperature is lower, instead, when the temperature reaches the regime temperature, it slightly increases and remains constant up to the pass end. Moreover, a higher distance from the surface implies a reduction in the temperature values, being the probe further respect to the heat source.

## 5.4.1. Depth of cut effect on the tangential dry grinding process

In Figure 69Figure 70Figure 71, it was shown the comparison between calculated and measured temperatures in function of the depth of cut. Good agreement was shown between the experimental acquisition and the model reaching a maximum average percentage difference of 11%, 13.2% and 15.4 % in correspondence of the temperature

acquired at 0.25, 0.5 and 1 mm from the surface, respectively. According with theory, a substantial increase in surface temperature is visible increasing the depth of cut, being the mechanical action more severe.



Figure 69. Grinding temperatures comparison: a) calculated and b) measured temperatures at 0.25, 0.5 and 1 mm in depth in the middle of the sample with the SG60 J6 VS3 grinding wheel at vt = 20 m/s; f = 10 mm/s; p = 0,001 mm



Figure 70. Grinding temperatures comparison: a) calculated and b) measured temperatures at 0.25, 0.5 and 1 mm in depth in the middle of the sample with the SG60 J6 VS3 grinding wheel at vt = 20 m/s; f = 10 mm/s; p = 0,025 mm

Figure 71. Grinding temperatures comparison: a) calculated and b) measured temperatures at 0.25, 0.5 and 1 mm in depth in the middle of the sample with the SG60 J6 VS3 grinding wheel at vt = 20 m/s; f = 10 mm/s; p = 0,005 mm

Figure 72 shows the microstructures related to the previous temperature acquisition at the different depth of cut. Removing 0.01 mm no thermal defects appear on the material surface, instead, with a depth of cut of 0.025 mm and then 0.05 mm a white layer with an increasing thickness is visible.



Figure 72. Surface microstructural analysis comparison: SG60 J6 VS3 wheel in correspondence of the middle of the sample with vt = 20 m/s; f = 10 mm/s and a) p = 0,001 mm; b) p = 0,025 mm; c) p = 0,05 mm.

The thermal cycle due to the dry grinding process with increasing depth of cut induced a surface micro-hardness change. In Figure 73 it is shown the micro-hardness trend in function of the depth of cut compared with the reference material. According with the microstructural analysis, removing 0.01 mm micro-hardness seems not to be changed, instead, with a depth of cut of 0.025 mm and 0.05 mm a substantial increase in the surface micro-hardness is visible.
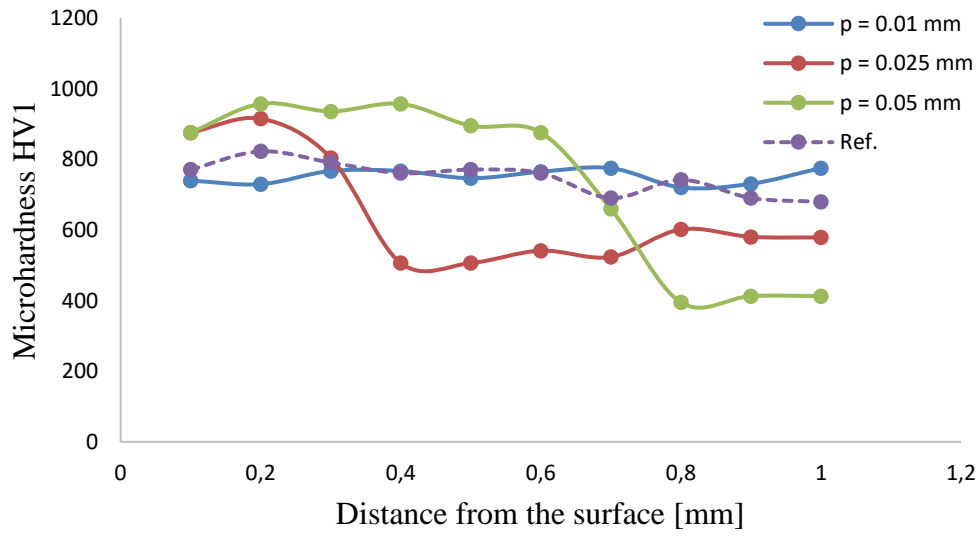


Figure 73. Micro-hardness measurements comparison in function of the depth of cut

## 5.4.2. Feed rate effect on the tangential dry grinding process

In Figure 74Figure 75Figure 76 it was shown the comparison between calculated and measured temperatures in function of the feed rate. Good agreement was shown between the experimental acquisition and the model reaching a maximum average percentage difference of 12.5%, 14.6 % and 13 % respectively at 0.25, 0.5 and 1 mm of distance from the surface. A substantial decrease in surface temperature is visible increasing the feed rate, being the interaction time between the wheel and the workpiece lower.
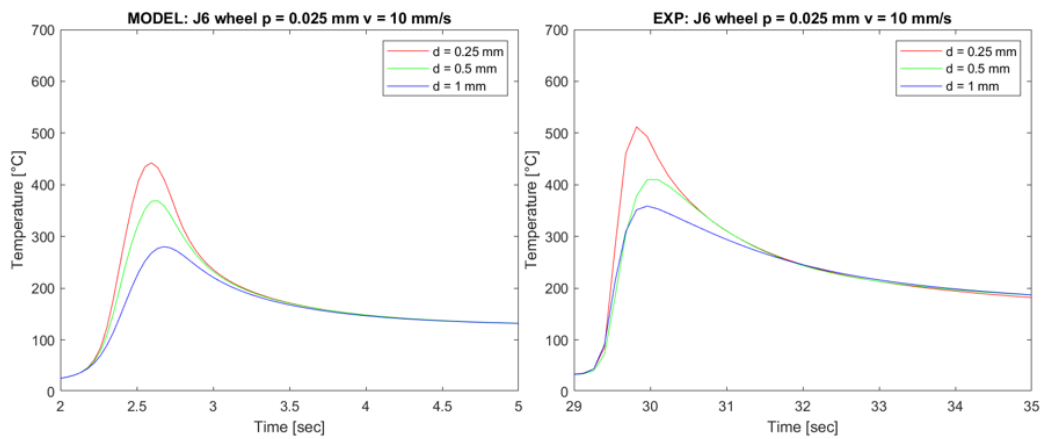
Figure 74. Grinding temperatures comparison: a) calculated and b) measured temperatures at 0.25, 0.5 and 1 mm in depth in the middle of the sample with the SG60 J6 VS3 grinding wheel at vt = 20 m/s; p = 0,025 mm and f = 10 mm/s
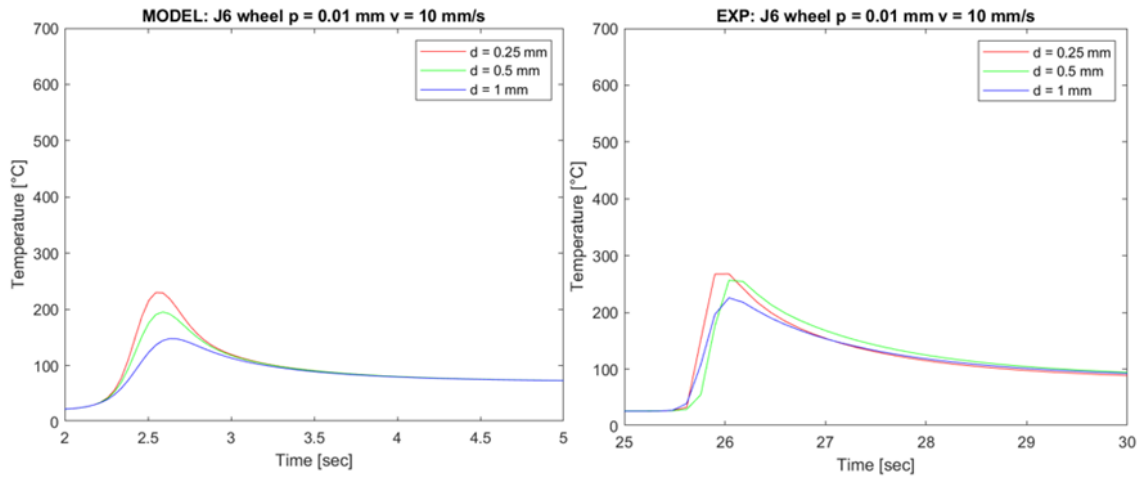


Figure 75. Grinding temperatures comparison: a) calculated and b) measured temperatures at 0.25, 0.5 and 1 mm in depth in the middle of the sample with the SG60 J6 VS3 grinding wheel at vt = 20 m/s; p = 0,025 mm and f = 20 mm/s
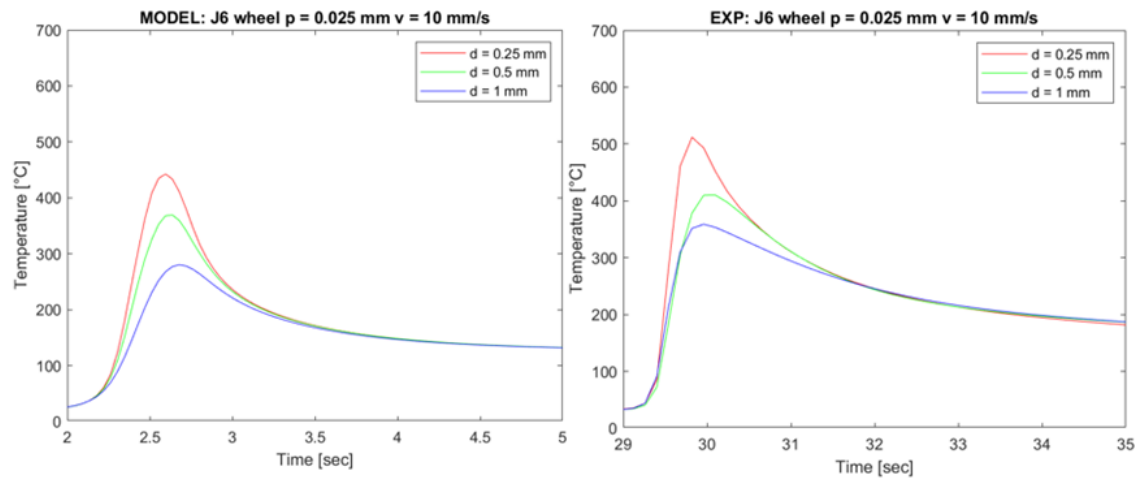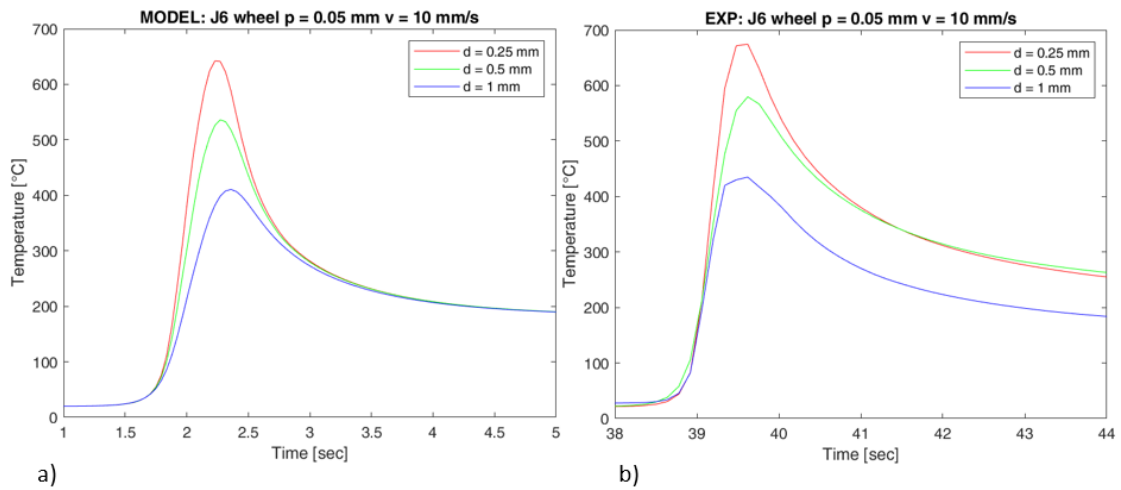


Figure 76. Grinding temperatures comparison: a) calculated and b) measured temperatures at 0.25, 0.5 and 1 mm in depth in the middle of the sample with the SG60 J6 VS3 grinding wheel at vt = 20 m/s; p = 0,025 mm and f = 40 mm/s

Figure 77 shows the microstructures related to the previous temperature acquisition at the different feed rate. Removing 0.025 mm at 10 mm/s, as shown before, induce a substantial white layer. At equal condition, with a higher feed rate of 20 mm/s a white layer appears again but its thickness is reduced. In this case, also a darkened layer was found in the subsurface. Instead, by adopting a feed rate of 40 mm/s no white layer appears, but a darkened layer seems be present on the surface.
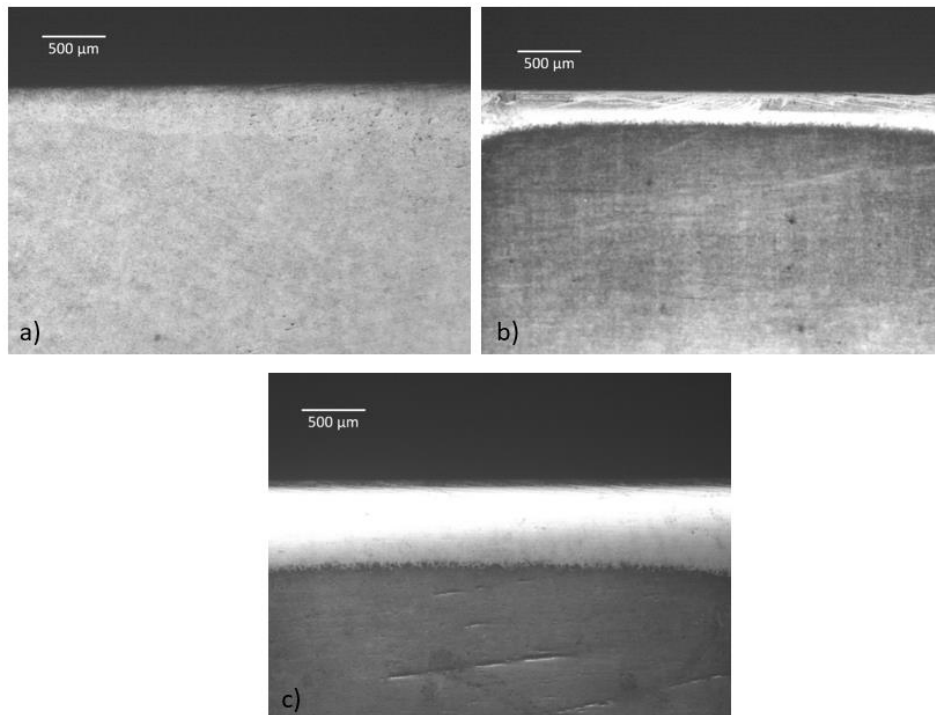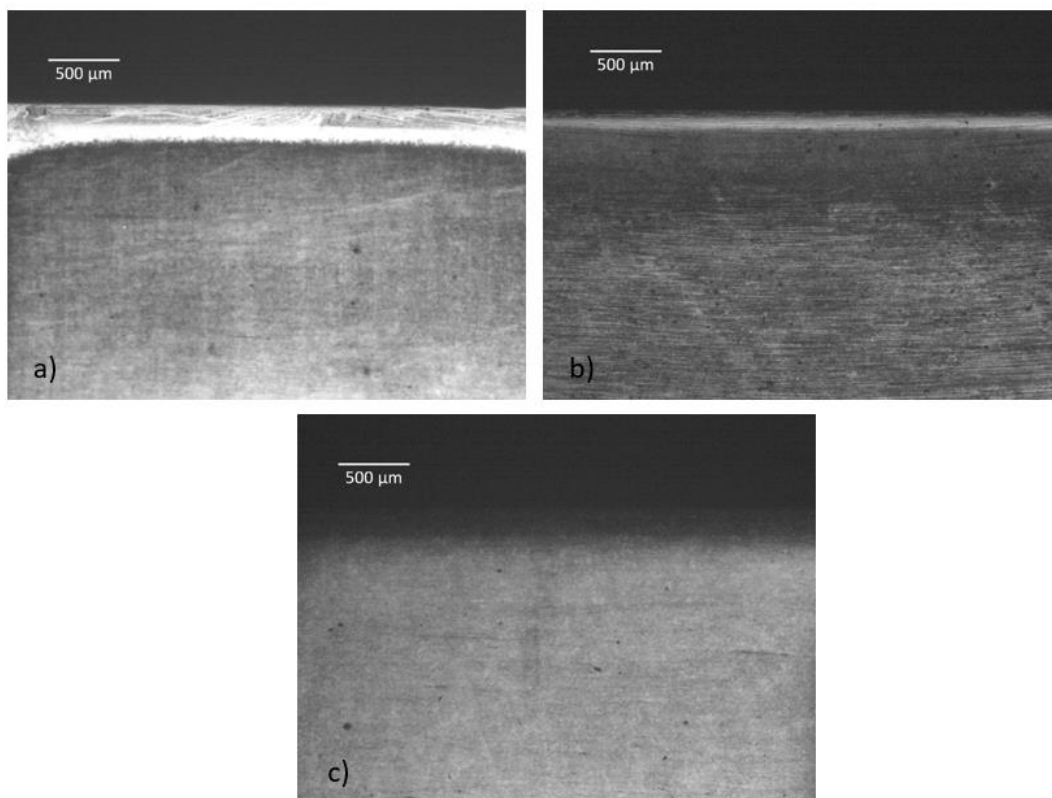


Figure 77. Surface microstructural analysis comparison: SG60 J6 VS3 wheel in correspondence of the middle of the sample with vt = 20 m/s; p = 0.025 mm and a) f = 10 mm/s; b) f = 20 mm/s; c) f = 40 mm/s

According with the microstructural analysis, the micro-hardness effectively gives a quantitative information about the thermal cycle induced by the dry grinding process by varying the feed rate, as shown in Figure 78. Indeed, the white layer found with a feed rate of 10 mm/s was correlated with an increase in the surface micro-hardness. Instead, in correspondence of a feed rate of 20 mm/s and 40 mm/s a slightly reduction in the surface micro-hardness was deduced according with occurrence of the darkened layer.
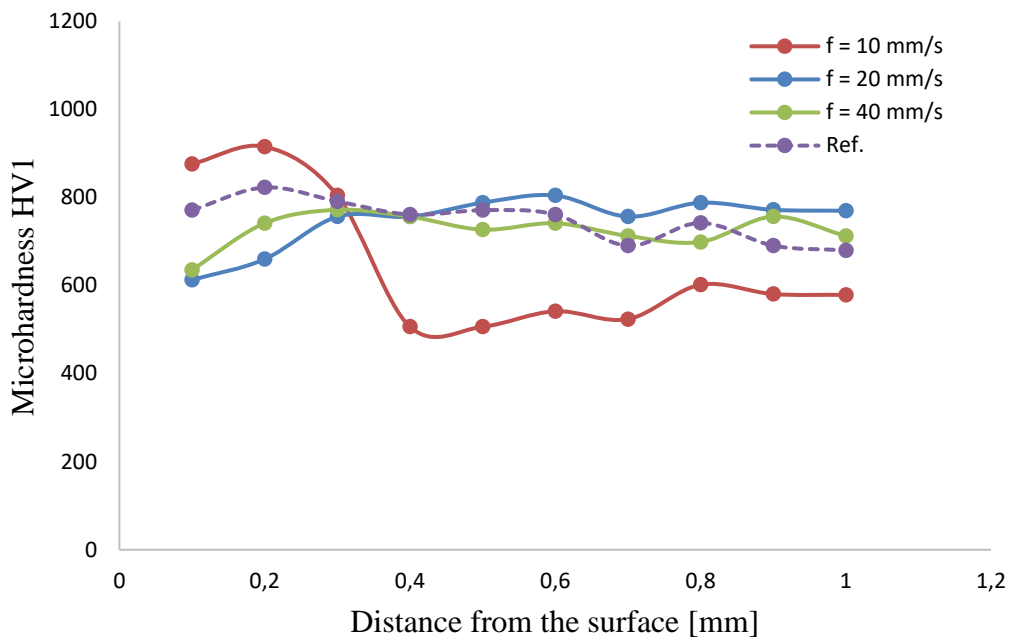
Figure 78. Micro-hardness measurements comparison in function of the feed rate

### 5.4.3. Grinding wheel specification effect on the tangential dry grinding process

In the following Figure 79Figure 80Figure 81Figure 82, the comparison between the calculated and measured temperatures acquired in the middle of the sample were reported for all the different wheel specifications. The comparison was considered in correspondence of a depth of cut of 0.05 mm and a feed rate of 10 mm/s being the thermal effect more visible. Model validation was achieved by detecting average percentage deviations between measured and computed temperatures of 4 %, 9.8 %, and 10.8 % for the thermocouples positioned at 0.25, 0.5, and 1 mm from the surface, respectively. When the different wheel structures were compared, it was noticed that an increase of the wheel structure reduces the heat effect caused by dry grinding. The comparison of estimated and measured temperature values for the wheels SG60 J6 VS3, SG60 J9 VS3, and SG60 J12 VS3 with increasing porosity was shown in Figure 79Figure 80Figure 81. Considering the temperature reached at the different surface depths, it was detected an average percentage difference in the measured temperatures of 33% between the less porous and the medium porous wheels, and a lower percentage difference between the medium porous and the more porous wheel equal to 9,5%. When the thermal effect of different wheel binder

hardness was compared, the softer wheel showed a significant reduction in dry grinding temperatures. Figure 80Figure 82 reported the temperature for the two different binder hardness results. In terms of process temperature, a reduction of 20.5 %, 5.5 %, and 4.5 % from the harder to the softer binder was observed in correspondence of 0.25, 0.5, and 1mm of distance from the surface.
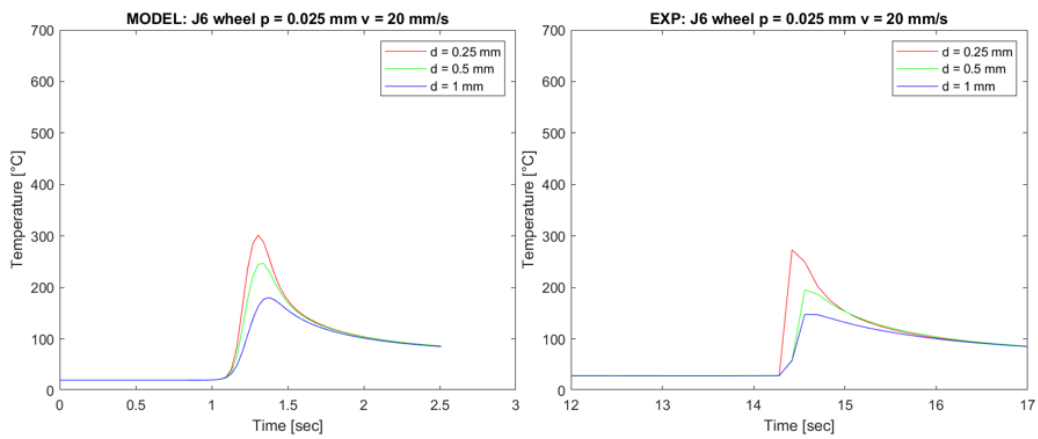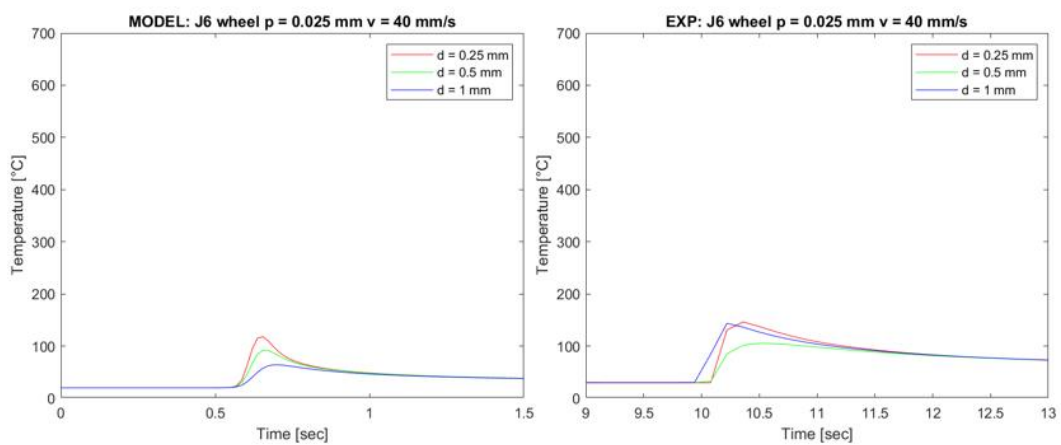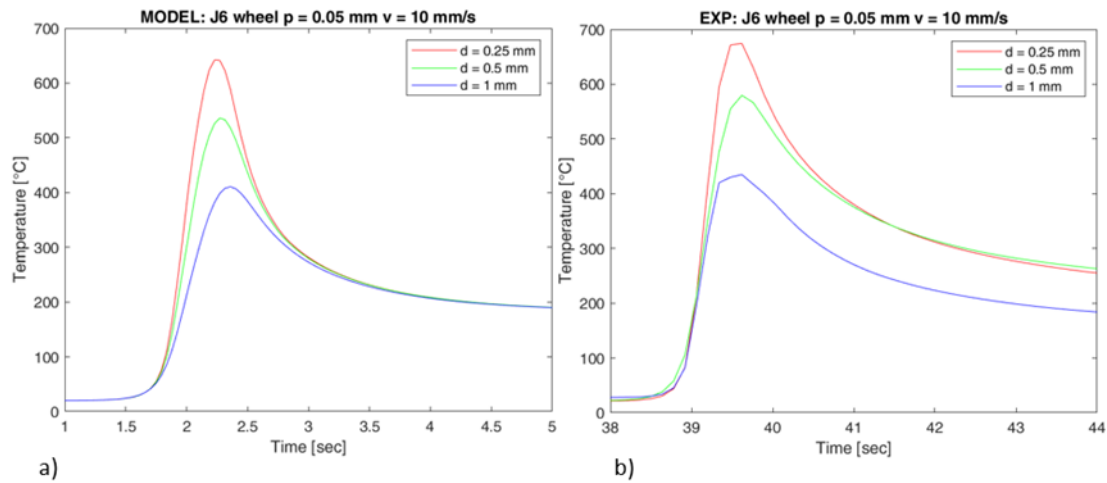


Figure 79. Grinding temperatures comparison: a) calculated and b) measured temperatures at 0.25, 0.5 and 1 mm in depth in the middle of the sample with the SG60 J6 VS3 grinding wheel at vt = 20 m/s; f = 10 mm/s; p = 0,05 mm
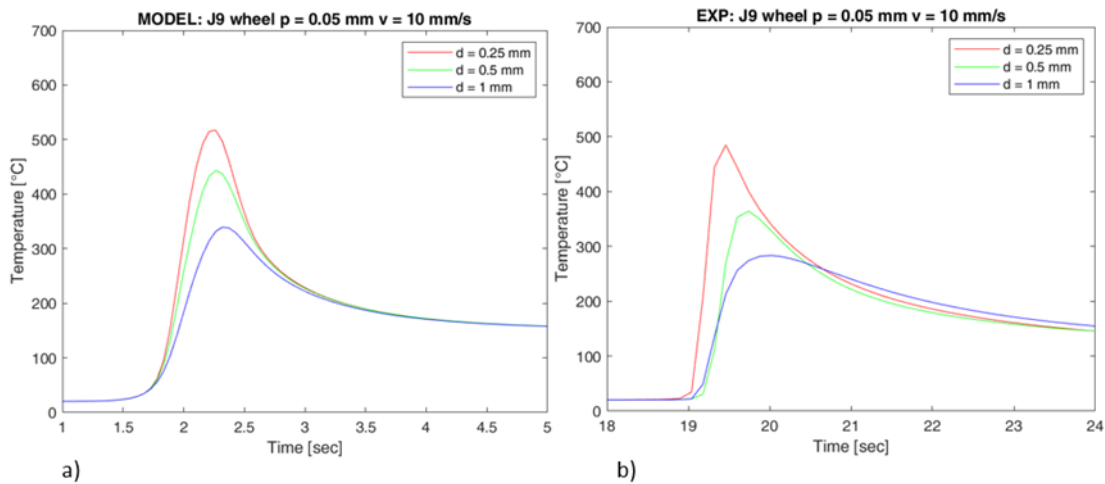


Figure 80. Grinding temperatures comparison: a) calculated and b) measured temperatures at 0.25, 0.5 and 1 mm in depth in the middle of the sample with the SG60 J9 VS3 grinding wheel at vt = 20 m/s; f = 10 mm/s; p = 0,05 mm
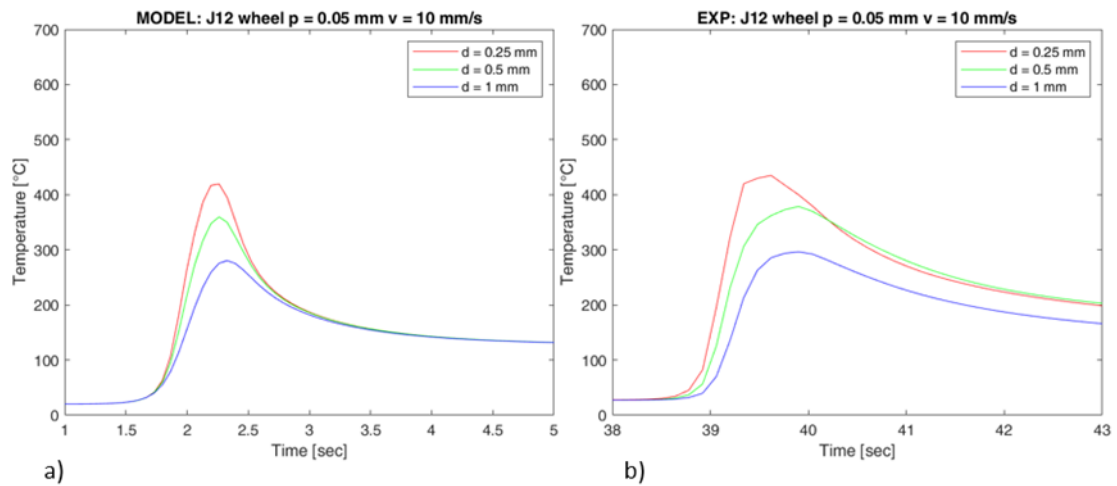
Figure 81. Grinding temperatures comparison: a) calculated and b) measured temperatures at 0.25, 0.5 and 1 mm in depth in the middle of the sample with the SG60 J12 VS3 grinding wheel at vt = 20 m/s; f = 10 mm/s; p = 0,05 mm
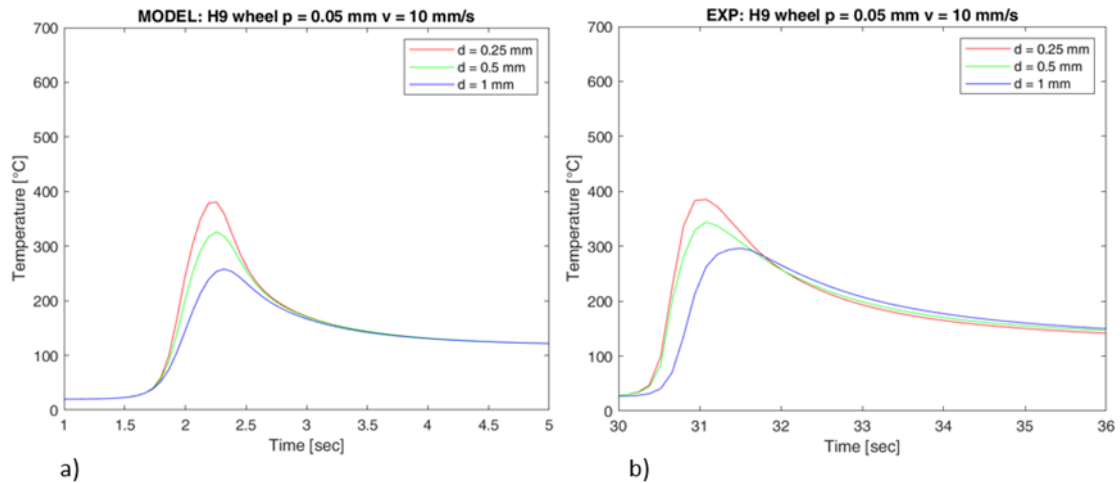


Figure 82. Grinding temperatures comparison: a) calculated and b) measured temperatures at 0.25, 0.5 and 1 mm in depth in the middle of the sample with the SG60 H9 VS3 grinding wheel at vt = 20 m/s; f = 10 mm/s; p = 0,05 mm

Maximum measured temperature was identified in correspondence of the less porous wheel SG60 J6 VS3 with a value of 675 °C. Increasing the porosity with the wheel specifications SG60 J9 VS3 and SG60 J12 VS3 the maximum temperatures measured at equal grinding conditions were 485 °C and 435 °C. When the binder hardness was reduced from grade J to H, the highest temperature measured at 0.25 mm from the surface dropped by 20% to 385 °C. According to the measured temperatures, it was verified that the heating and cooling process is very fast and overcomes the ultra-fast heating processes rates. The maximum temperatures were reached in around 1 second, with a heating rate

of around 100 °C/sec, based on the measured temperatures. This effect was traduced in a thermal cycle on the surface material. Surface microstructures correlated with temperature were reported in Figure 83 to demonstrate the influence of the grinding wheel specifications used under the same process settings. Microstructures, as well as temperature trends showed before, were detected in correspondence of a depth of cut of 0.05 mm and a feed rate of 10 mm/s. The model allows to calculate also the temperatures achieved at the surface; therefore, the validated model give an estimate of the maximum temperatures reached at the surface within a defined process parameters set. For the three distinct structures and the softer binder, maximum surface temperatures of 771 °C, 741 °C, 493 °C, and 449 °C were calculated, respectively. The calculated temperatures reflect the microstructural alteration in the dry ground material. Grinding thermal defect appear as a darker and white layer as the process temperature rises. Micro-hardness measures provided additional confirmation. The darkened layer is linked to a surface softening effect, while the white layer is correlated to a surface re-hardening.
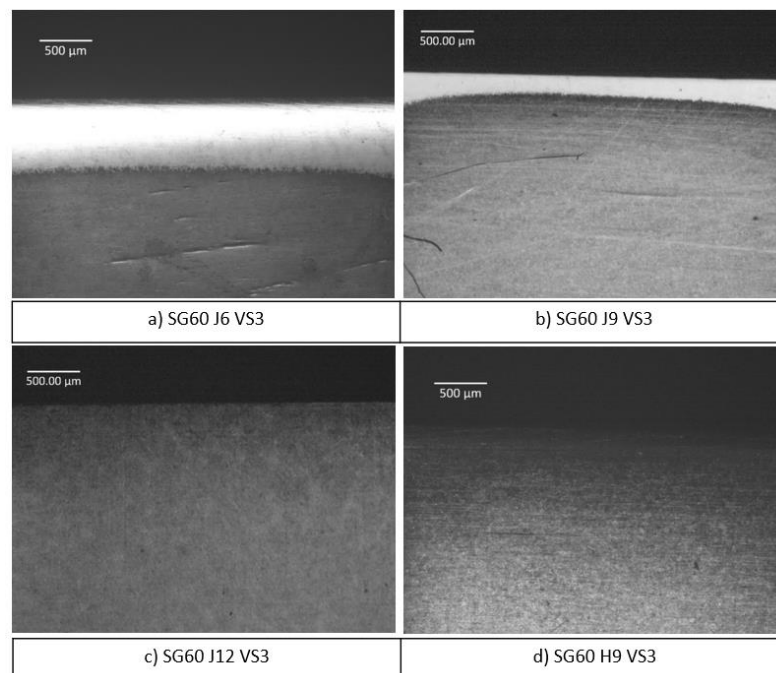


Figure 83. Surface microstructural analysis comparison: a) SG60 J6 VS3 wheel; b) SG60 J9 VS3 wheel; c) SG60 J12 VS3 wheel and d) SG60 H9 VS3 wheel in correspondence of the middle of the sample with vt = 20 m/s; f = 10 mm/s; p = 0,05 mm.

This phenomenon often leads to an abnormal increase of the mechanical strength and crack formation. The micro-hardness data associated to the microstructure reported were shown in Figure 84 in comparison with the reference not ground material. The black layer appeared when the temperature is above 400°C, while the white layer appeared when the temperature exceeded the austenitization temperature, that could be considered as the material critical temperature, as first attempt. The microstructural investigation revealed the occurrence of a white layer removing 0.05 mm at 10 mm/s with the wheel with low and medium porosity, and a darkened layer with the higher structure number and softer binder, according to the highest grinding temperature obtained. When the surface micro-hardness of the reference material was compared to the microstructure achieved in the dry grinding configurations studied, it was discovered that the low and medium porosity binder wheels had a 16 % increase in surface hardness, while the high porosity and softer binder wheel assumed a 25 % and 37 % reduction in surface hardness, respectively. Furthermore, the micro-hardness showed a thicker hardened layer in correspondence of the low porosity wheel compared to the medium porosity wheel.
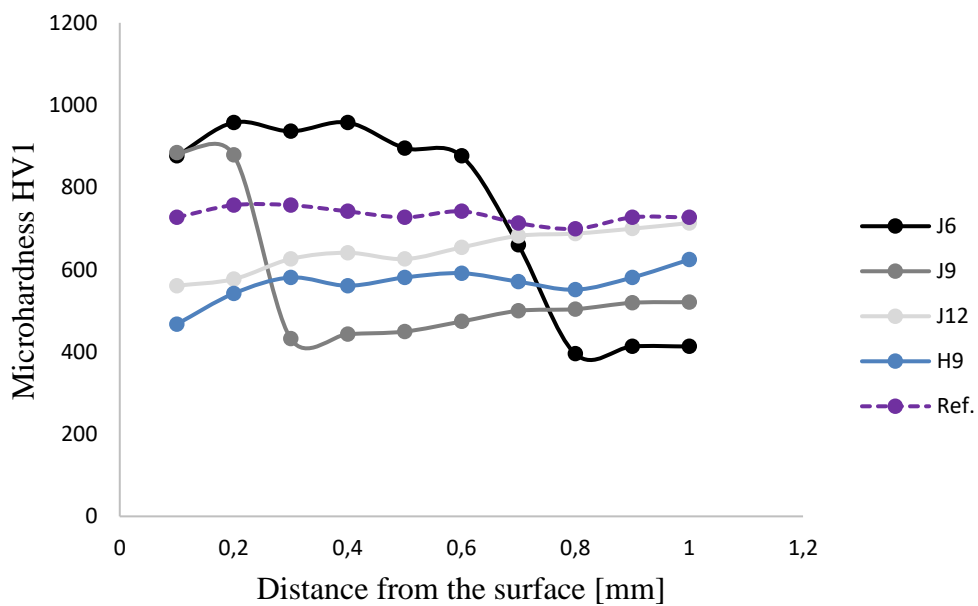


Figure 84. Micro-hardness measurements comparison between the different grinding wheel specifications

In Figure 85, the maximum temperatures calculated by the model were reported for all the dry grinding configurations and grinding wheel adopted in the experimental plan.

Increasing the depth of cut, the maximum temperatures increase because of the increase of the heat generated, instead, with an increase in feed rate the interaction time between the wheel and material decrease and the maximum process temperature decrease. Grinding burns occur at the highest process temperature and start around the material austenitization temperature. With a decrease of the grinding heat generation an area with a reduction of the hardness up to 450 HV1 was identified until 400 °C. Between 400°C and 250°C, an intermediate zone exists and it is characterized by a slightly decrease of the surface hardness up to 600 HV1. The feasibility area occurs under a maximum calculated temperature of 250 °C, where no defects were detected.
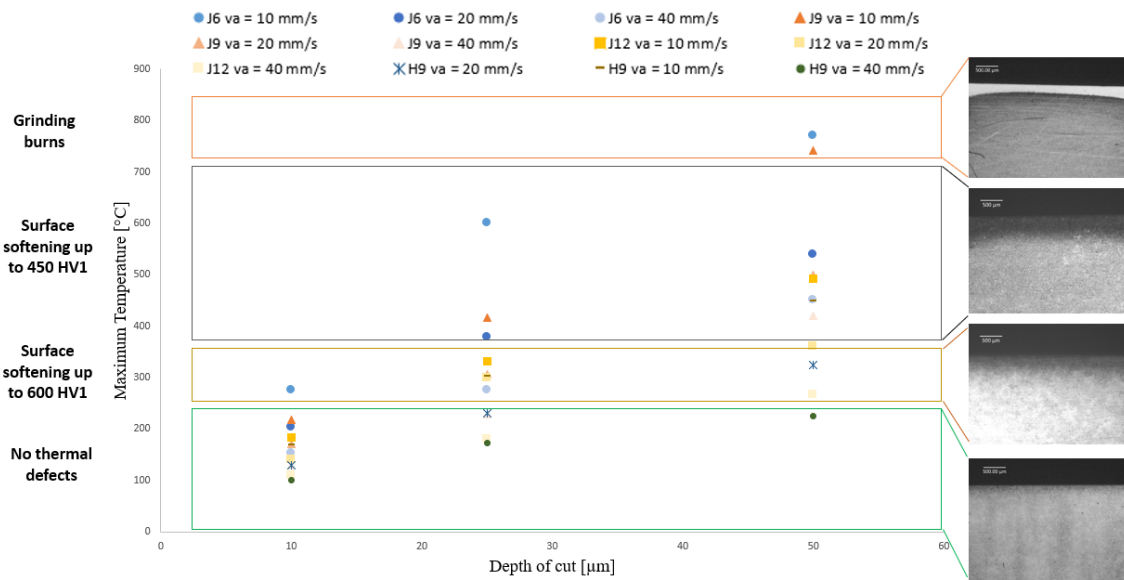


Figure 85. Dry grinding maximum calculated temperatures and feasibility areas

In conclusion, the model can predict the temperature reached at the surface of the material due to the grinding process performed in dry conditions. It is possible to predict the thermal effect of the process considering both the process parameters and the grinding wheel specification. It is important to noticed that the temperature intervals reported in the feasibility areas are correlated with the tangential grinding process. Temperature thresholds in the gear grinding process could slightly change being the heat conduction phenomenon different. Indeed, in a tangential grinding operation the heat flux is transmitted in a limited time but continuously, instead, during a grinding operation

applied on gear the contact between one tooth and the wheel is not continous because it is interspersed with cooling phases due to the contact displacement on the other teeth, therefore the interaction time becomes lower. In the following chapter, the validated model just presented will be applied to a gear tooth geometry replying the actual gear grinding process.

# Chapter 6

# Gear dry grinding modelling and experimental validation

The aim of the project is based on the prediction of thermal defects induced by the grinding process performed in dry conditions applied on automotive gears. The proposed model aims at forecasting the temperature generated during the grinding to optimize the design phase of the process. In particular, the model has the duty to give an estimate on the possible occurrence of thermal defects on the gears' flanks based on the choice of the kinematic process parameters and the grinding wheel specifications.

As stated so far, the model is composed of two main parts analysing the microscopic and the macroscopic effect of the grinding on the material. The first approach allows to estimate the thermo-mechanical power generated during the material removal action due to a single grain in function of the workpiece material physical and mechanical properties, the grains shape characteristics and the kinematic process parameters, such as the cutting speed, the feed rate and the depth of cut. The second approach allows to estimate the temperature generated during tangential dry grinding process considering the materials properties, the process parameters and also the griding wheel specification. The tangential thermal model and experimental tests were a necessary step between the single grain grinding model and the application of the final model on the gear tooth geometry, because it allowed to directly validate the thermal model through temperatures acquisitions. In this way, it was possible to proceed with greater confidence at the next step.

Therefore, after validating the tangential thermal model, its features were translated on the gear thermal model. The model structure was taken over from a previous work, of which the gear generating grinding kinematics and the contact area between the worm grinding wheel and the gear teeth will be considered. The optimization of the present model was achieved by introducing the following aspects:

- Single grain grinding thermal power calculation considering the equivalent defined grain shape and the optimized material flow stress curve.
- Heat source amplitude which took in consideration the optimized single grain grinding power.

- Heat source asymmetrical top-hat distribution.
- Case-hardened depth thermal conductivity law.
- Grinding wheel specification's introduction which allows to analyse the effect of the porosity and binder hardness.

In the following chapter, the gear dry grinding tests and the model novelties will be described and discussed.

## 6.1. Gear dry grinding experimental tests

### 6.1.1. Experimental set up

Dry grinding tests were performed on a Samputensili SG 160 Sky Grind machine, characterized by the presence of two spindles and designed for automotive mass production (Figure 86). Gear dry-hard finishing comprises two different steps. A previous skive-hobbing phase which adopts a defined-geometry tool, removes the main allowance on the gear; then a grinding pass allows to obtain the stringent dimensional requirements removing a minimum amount of material reducing the thermal defects risk. An optical sensor promotes the correct phasing of the gear which is positioned on an expansion spindle and rotates with a rotational speed according to the transmission ratio with the wheel.



Figure 86. SG 160 Sky Grind machine work area configuration

The reference helical gear represents a typical automotive gear used as the four-six speed of six-speed gearboxes and was made of 27MnCr5. Geometric data were reported in Table 12. After a green turning and the hobbing phase, the gears were heat treated through vacuum carburizing and gas quenching followed by stress relieving in order to reach a surface hardness range of 680-790 HV10.

Table 12. Characteristics of gear

| Parameter | Value |
|---|---|
| Normal module m | 1.8 mm |
| Maximum roughness $R_a$ | 0.6 µm |
| Maximum profile form error ffα | 6 µm |
| Maximum helix form error ffβ | 5.5 µm |
| Helix crowning range cβ | 4±2 µm |

Two different grinding wheels characterized by medium and high binder hardness and medium porosity in aluminum oxide were used to analyze the effect of different grinding wheel specification on the gear quality. Grinding wheel specifications were chosen based on the company experience and their characteristics were reported in Table 13.

Table 13. Characteristics of grinding wheels

| Parameter | Wheel 1 | Wheel 2 |
|---|---|---|
| Diameter $D_w$ | 250 mm | 250 mm |
| Width $b_w$ | 100 mm | 100 mm |
| No. starts | 4 | 4 |
| Abrasive grain material | Aluminum oxide | Aluminum oxide |
| Grit size | 120 | 120 |
| Binder type | Vitrified | Vitrified |
| Binder hardness | H | N |
| Structure | 11 | 13 |

In Table 14 the dry grinding cycle parameters used for all the set up were reported. Each grinding cycle was preceded by a skive-hobbing phase which adopted a cutting speed of 2.5 m/s, a stock of 0.09 mm and a feed rate of 2.27 mm/rev. Grinding tests with the different grinding wheels were performed using two different values of feed rate.

Table 14. Dry grinding process parameters

| Parameter | Set up 1 | Set up 2 | Set up 3 | Set up 4 |
|---|---|---|---|---|
| Grinding wheel | Wheel 1 | Wheel 1 | Wheel 2 | Wheel 2 |
| Cutting speed $v_t$ | 80 m/s | 80 m/s | 80 m/s | 80 m/s |
| Number of passes | 1 | 1 | 1 | 1 |
| Stock removal $p$ | 0.01 mm | 0.01 mm | 0.01 mm | 0.01 mm |
| Feed rate $f$ | 0.34 mm/rev | 0.54 mm/rev | 0.34 mm/rev | 0.54 mm/rev |
| Shifting $sh$ | 0.03 mm/mm | 0.03 mm/mm | 0.03 mm/mm | 0.03 mm/mm |

## 6.1.2. Gear surface integrity analysis

Gear macro and micro-geometric accuracy addressed the deviations in tooth spacing, profile and helix slope, and tooth surface profile and helix roughness and form deviation, respectively. Macro geometry depends on process kinematics and wheel dressing. Meanwhile, micro geometry is determined by the process parameters. The accuracy of a produced gear, in terms of dimensional tolerances, is identified by comparing the real and the designed geometry. The dimensional tolerances measurements were performed according to AGMA915-1-A02 [156] on the flank profile and the flank lead on four diametral distanced teeth on both right and left flank. Dimensional tolerances analysis takes place in a Klingenberg measuring system with the gear placed on a shaft and the contours of the teeth was acquired via a touching probe along the profile and lead directions. In particular, the characteristics considered can be summarized as follows:

1. ffα is the profile form deviation and represents the deviation between two lines parallel to the average profile intercepting the highest and the lowest point on the profile in the evaluation field (Figure 87 a).

2. ffβ is the helix form deviation and represents the deviation between two lines parallel to the average helix intercepting the highest and the lowest point on the profile in the evaluation field (Figure 87 b).

3. cβ is the helix crowning and represents the chordal thickness of the tooth along its axis (Figure 87 c).

Measurement of these parameters was carried out on both the right and left flanks and the arithmetic average was calculated to obtain one single value for each parameter and gear.



a)



b)

c)
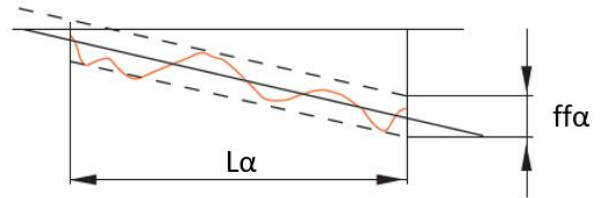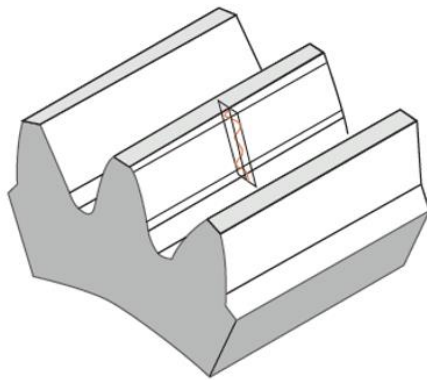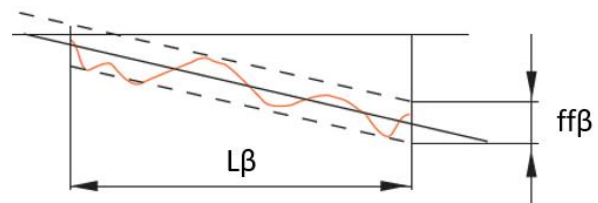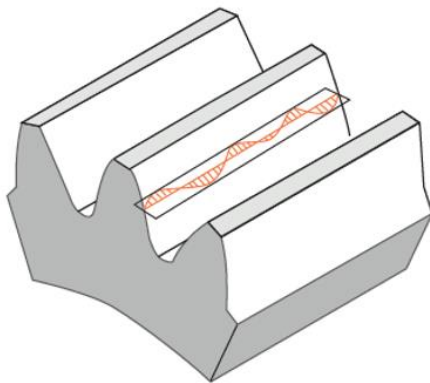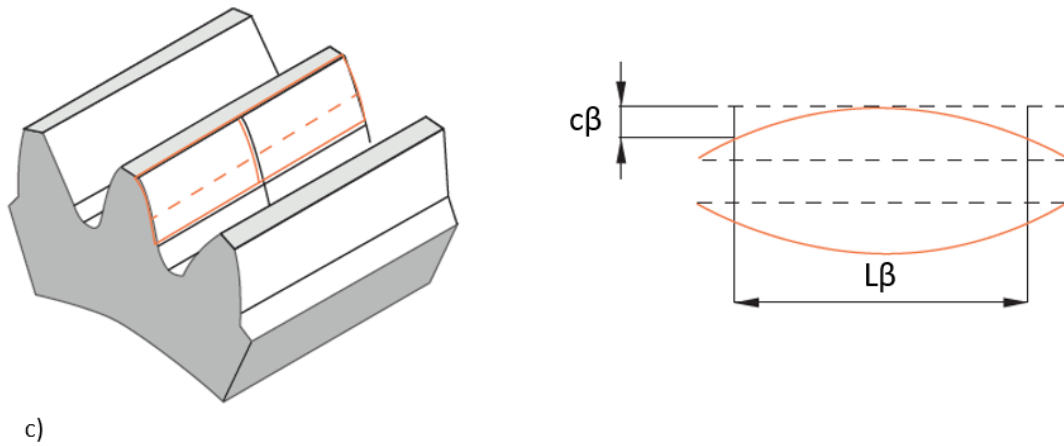
Figure 87. Definition of profile form deviation ffα (a); helix form deviation ffβ (b); helix crowning (c)

Tooth profile and helix arithmetical mean roughness Ra measurements were performed on three teeth for each configuration using a Klingenberg P65 measuring system (Figure 88). Roughness values were detected on both right and left flank. Microstructural analysis was carried out with an optical microscope Zeiss Axio Vert.A1M with magnification 20x on the samples prepared according to standard metallographic techniques comprising mechanical grinding (80-2400 grit paper) and polishing with alumina in suspension down to a particle size of 6 to 1 μm. To reveal microstructural features, the samples were etched using Nital reagent for 3 s. Microstructural analysis was performed to verify the presence of thermal defects on both right and left flank.

Figure 88. Klingenberg P65 measuring system

## 6.2.  Gear dry grinding model description

Despite its simplification, the model must be able to replicate the specific kinematics of the helical gear grinding process with worm wheel. The motion determined the shape, the dimensions and movement of the contact area between the wheel and the gear. Even the geometry of the gear (module and number of teeth) and the grinding wheel (diameter and number of principles) have an impact on these features. During the gear grinding, the number of contact regions is not constant, but the grinding wheel and workpiece mesh together at various points, with several contact areas ranging from 1 to 4. Figure 89 reported the gear's contact lines during the meshing.
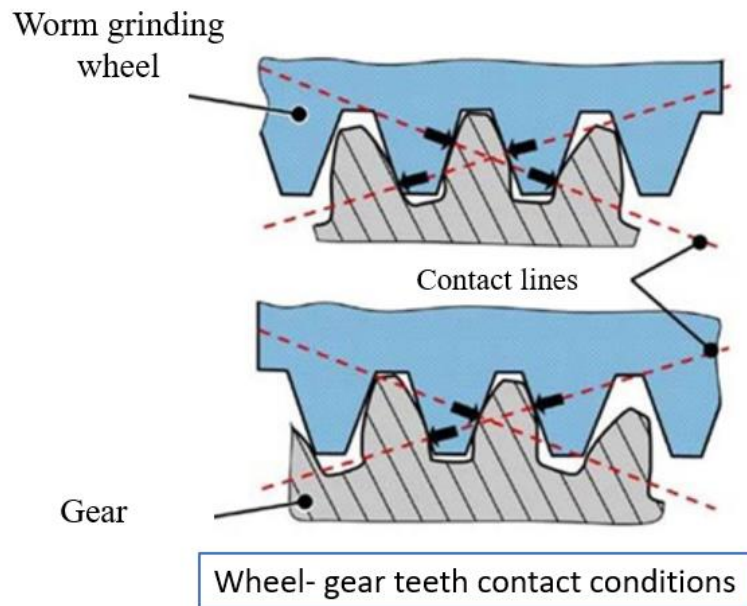
Figure 89. Gear generating grinding kinematics and wheel-gear contact conditions

Combine the thermal aspects with a correct kinematic representation and considering the whole wheel and gear geometries would require significant computing powers making the model unusable for the industrial use. Therefore, to overcome this problematic, the model introduced a series of hypotheses to represent the process in a reliable way but reaching a fast and exploitable simulation when optimizing process. The following information related to the contact area description and the gear grinding kinematics were taken from a previous work [127], [128]. It is known that the area of contact between the wheel and gear is characterized by an irregular geometry that could vary during the grinding pass in shape and size [157]. This area has an average approximate shape of a semi-ellipse that moves on the side of the tooth thanks to the relative motion of gear and grinding wheel. Being the heat source variable in dimensions, the geometry of the contact area was designed with a rectangle whose dimensions are equal to the minor axis and the semi-major axis of the ellipse. Moreover, to reduce the computational effort of the simulation, the model was developed considering only a single gear tooth. The gear tooth was represented with a simplified trapezoidal geometry and a further rectangular block of material was added below it to simulate the presence of the gear body material ranging from the base of the tooth to central hole in the shaft. The complex paths of the grinding

wheel– tooth contact areas were simplified within the thermal model as shown in Figure 90. On one side the contact begins at the head and ends at the foot, the opposite occurs on the other side. The speed with which the area is moves on the side is not constant but, as for its size varies along the diameter, being minimum to the foot and maximum on the head. The height, width, and velocity of the heat sources varies linearly along diagonal paths across each tooth flank from minimum values at the root to maximum values at the tip, which were calculated from process kinematics and gear geometry.
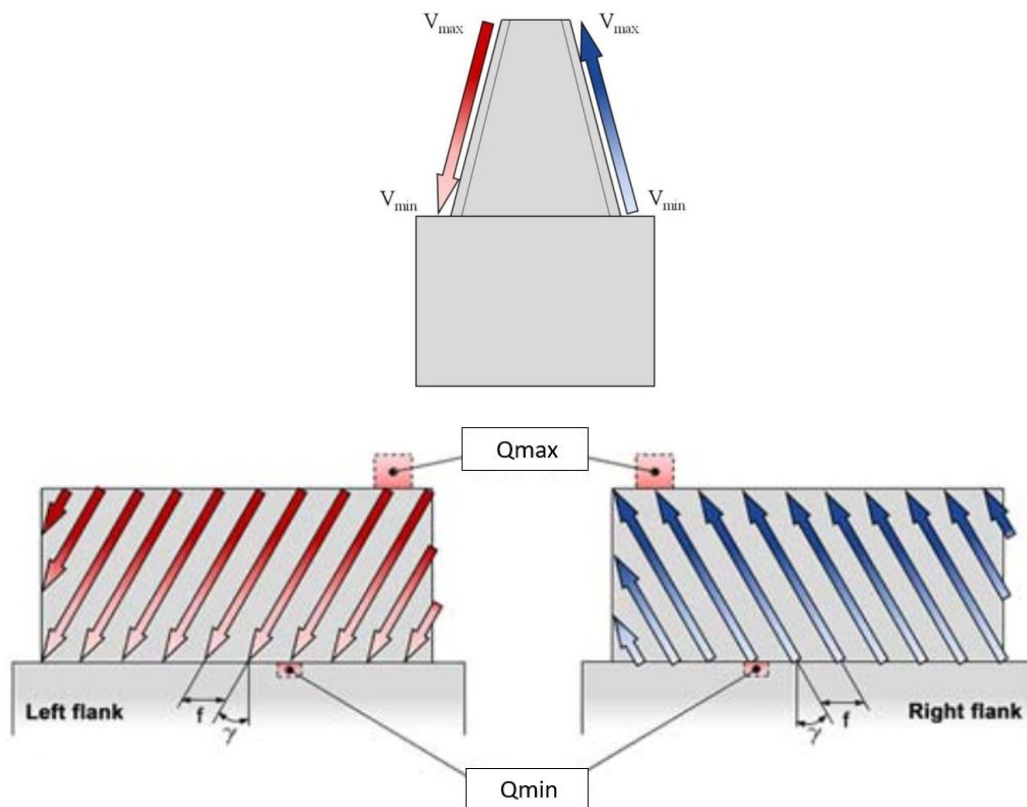


Figure 90. Kinematics of wheel–workpiece contact area: simplified heat source motion within the thermal model

Figure 91 show the moving heat source at the same time on the left and right gear flank. The temperature field generated by the grinding process was analysed in correspondence of the middle cross section of the gear tooth when the temperature reached there assume the maximum values to compare the results with the microstructural analysis. Temperatures were considered in correspondence of the surface respectively at the flank tip, in centre and at the flank root for both the flanks by inserting

probes, as shown in Figure 92. The total number of workpiece elements and nodes was 91180 and 18118, respectively.
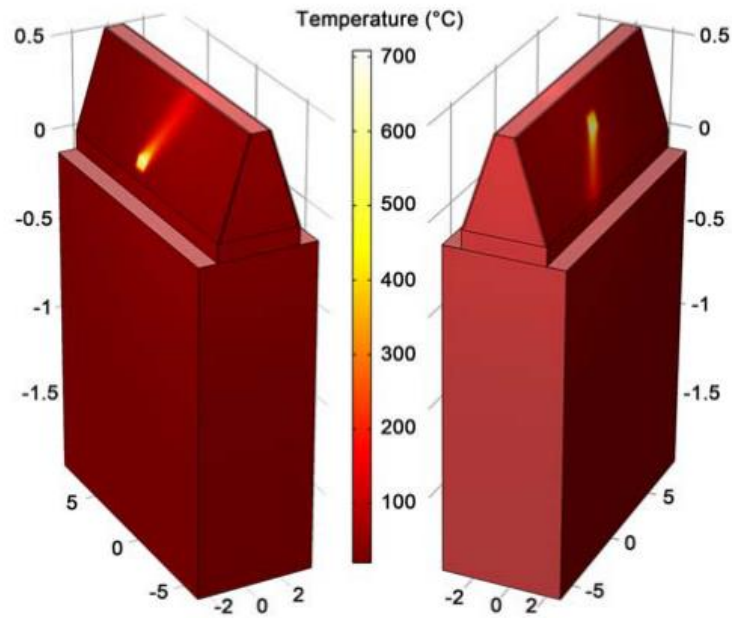


Figure 91. Simulated temperature distribution on left and right gear flanks
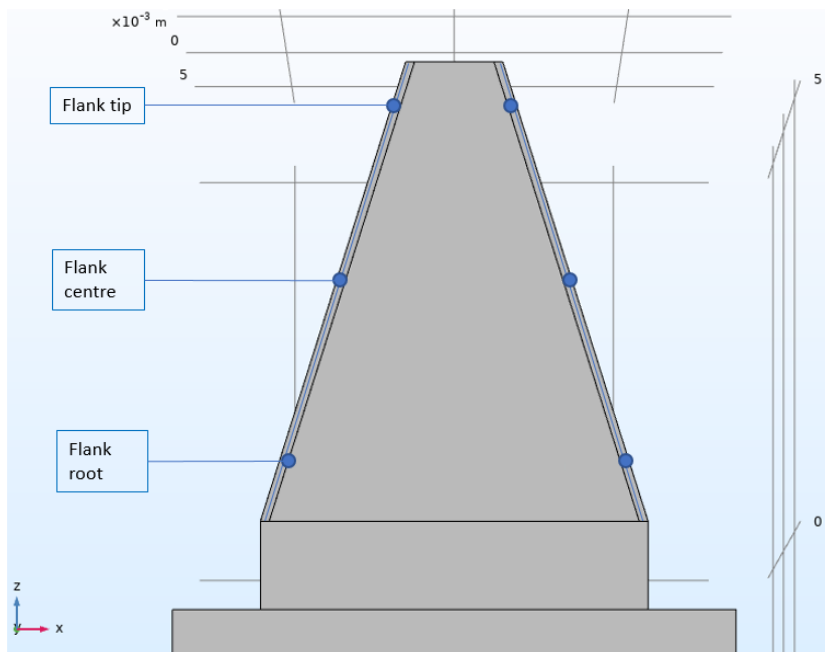


Figure 92. Gear dry grinding model thermocouples positioning

## 6.3. Gear dry grinding validation results discussion

The present study aimed at forecasting grinding thermal defects to ensure the surface integrity on dry ground gears through the application of different grinding wheels and process parameters in a real industrial environment. Dry grinding tests were performed removing 0.01 mm of depth of cut with a wheel cutting speed of 80 m/s using two different feed rate values equal to 0,34 mm/rev and 0,54 mm/rev. The single grain grinding model procedure described before was applied to the new process parameter set. Since simulating a cutting speed of 80 m/s in DEFORM 3D was not feasible, the single grain grinding thermal power was extrapolated by regression by simulating an increasing cutting speed. Two different wheel specifications were adopted. In both cases, aluminum oxide with size 120 was adopted as grain material and dimensions, but porosity and binder hardness were, respectively, 11 and I for the softer wheel and 13 and N for the harder one, resulting in a grain density respectively equal to 67 grain/mm$^2$ and 114 grains/mm$^2$.

Model results were presented to show the comparison between the maximum temperatures reached at the surface of the gear tooth calculated in the peak temperature instant with the microstructures. The comparison was considered for two different grinding wheels and two different feed rate values in correspondence of the middle cross section where the microstructural analysis was performed. At first, the temperature's outcomes were presented as temperature field within the gear tooth geometry and temperature trend in function of the process time in correspondence of the applied probes. Figure 93Figure 94Figure 95Figure 96 reported the comparison between the temperature calculated through the gear grinding model and the cross-section microstructures. In particular, Figure 93 is correlated to the experiments adopting a feed rate of 0,34 mm/rev, so the temperatures were considered in correspondence of a process time of 3.35 s. In the first case, the use of the softer wheel characterized by a medium porosity of 11 and a medium binder hardness of I led to a maximum calculated grinding temperature around 550°C that effectively reflects an initiation of the darkened layer and consequently a softening phenomenon.
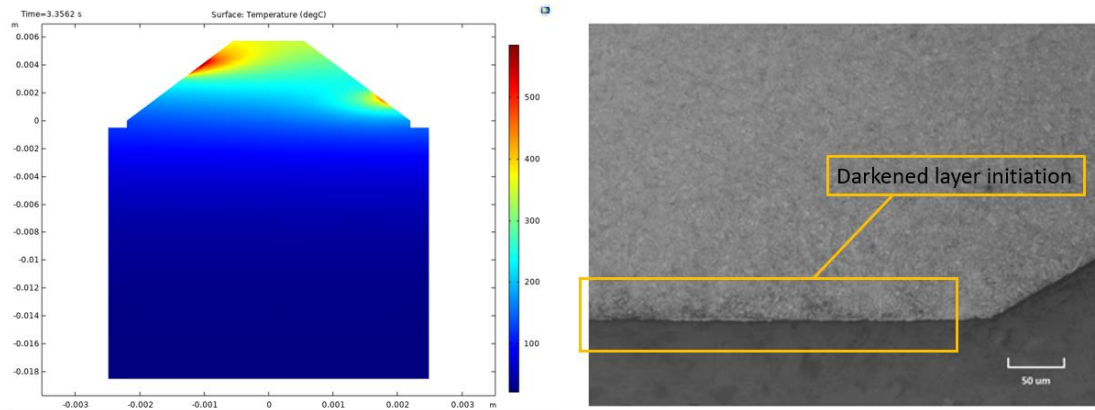
Figure 93. Gear dry grinding model temperatures and microstructural analysis using the softer I11 wheel at $f = 0,34$ mm/rev

Figure 94 shows the results related to the application of the harder wheel with a medium porosity of 13 and a hard binder hardness defined with the letter N at 0,34 mm/rev. The model calculated a temperature value higher than the austenitization temperature with a maximum value over 900°C, accordingly with the microstructure that showed a clear darkened and white layer formation. The model was further validated by comparing the effect of the adopted grinding wheel at a different feed rate of 0,54 mm/rev. In this case, the time frame was considered at a lower time equal to 2.19 s being the feed rate higher. Figure 95 showed that using the softer wheel with a higher feed rate of 0,54 mm/rev a lower temperature around 350 °C was reached. Good agreement was achieved by comparing the model temperature with the microstructure that did not reveal any remarkable thermal defects.
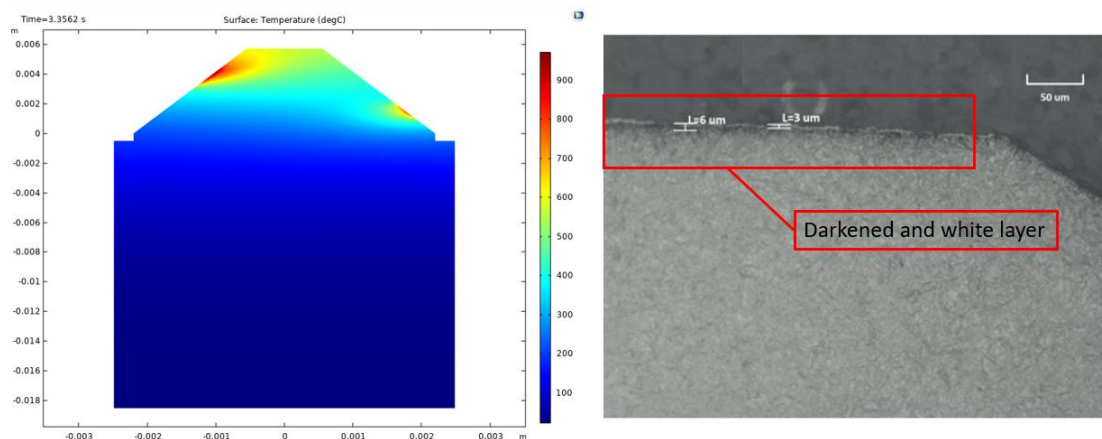


Figure 94. Gear dry grinding model temperatures and microstructural analysis using the harder N13 wheel at f = 0,34 mm/rev
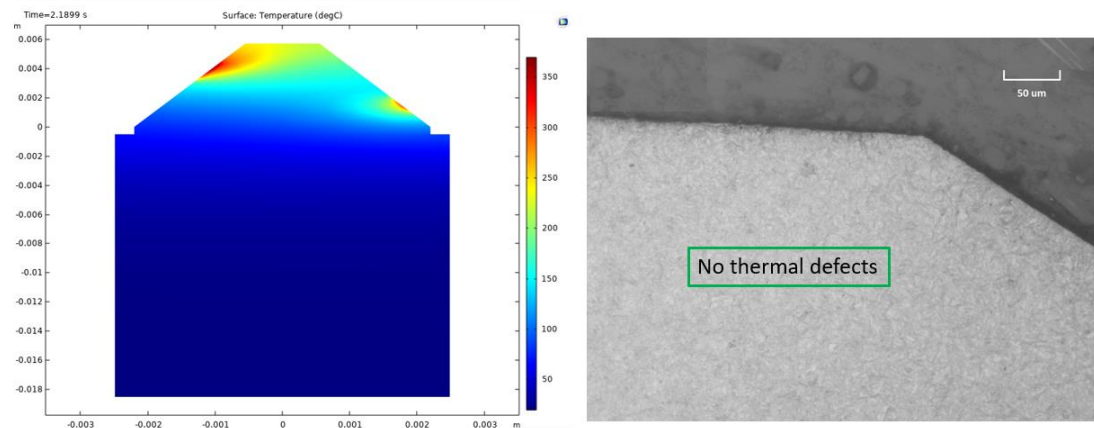
Figure 95. Gear dry grinding model temperatures and microstructural analysis using the softer I11 wheel at f = 0,54 mm/rev

Instead, Figure 96 showed the model and microstructure outcome related to the harder wheel at 0,54 mm/rev. The model was further validated, since the maximum temperature calculated overcome the austenitization temperature reaching a temperature higher than 800 °C and the microstructural analysis showed the occurrence of a darkened and white layer demonstrating the thermal effect induced.
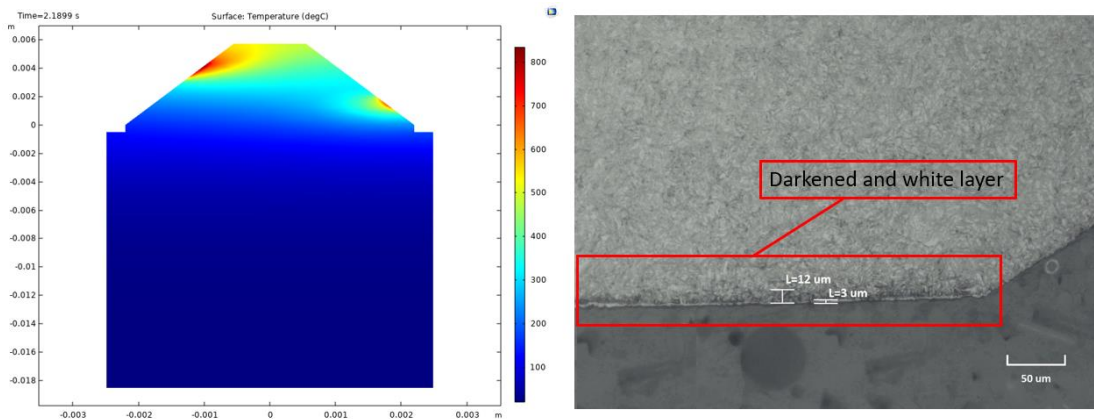


Figure 96. Gear dry grinding model temperatures and microstructural analysis using the harder N13 wheel at f = 0,54 mm/rev

To effectively verify the thermal cycle induced by the different grinding process parameters set, Figure 97Figure 98Figure 99Figure 100 showed the temperatures calculated by the model in function of the time in correspondence of the tip, the middle and the bottom of the right and left flanks, respectively using the softer and harder wheel with a feed rate of 0,34 mm/rev and 0,54 mm/rev. First of all, it is possible to noticed that

the temperature peak is reached in a lower time with the higher feed rate. Indeed, the time when the maximum temperature is reached was considered around 3.35 s and 2.19 s, respectively, for the lower and the higher feed rate value, as mentioned before. The maximum temperature was detected at the tip of the flank, instead, the lower one was calculated at the bottom for each grinding cases. The temperature trends reported in the graphs represent the temperature calculated for each grinding pass along all the tooth width. Each curve sees its values increase with an oscillating trend that represents the multiple pass of the wheel on the gear tooth until the end of the operation with intervals of cooling due to the contact displacement on the other teeth. It is possible to notice that the temperature peak occurs in a very limited time. Maximum temperatures calculated agree with the microstructure reported before and allows to compare the grinding thermal effect in function of the feed rate and the grinding wheel specification.
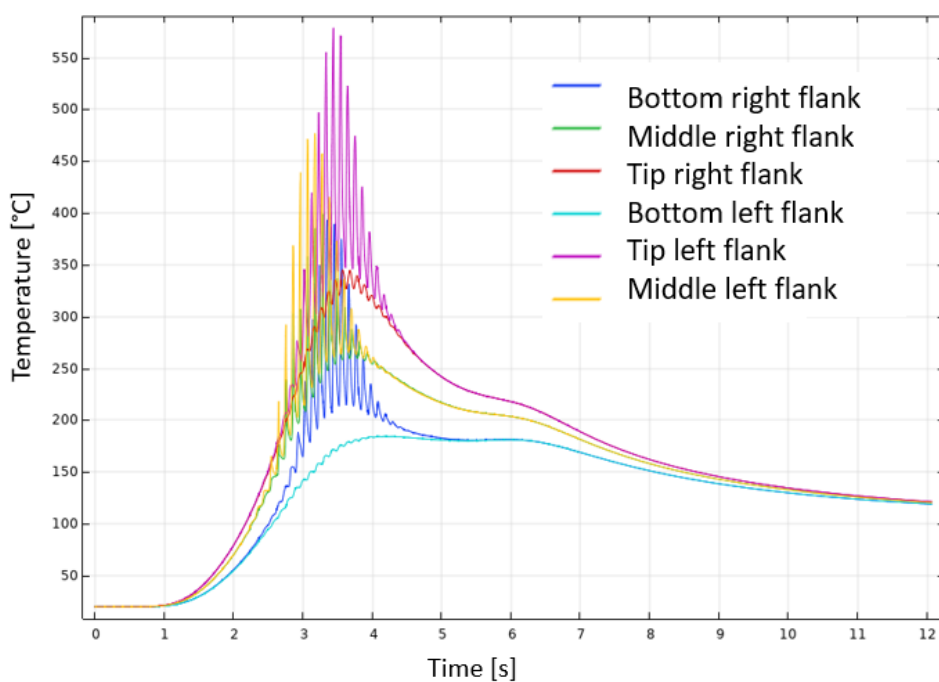


Figure 97. Calculated temperatures in function of the time in correspondence of the tip, the middle and the bottom of the right and left flanks using the softer wheel I11 with $f$ =0,34 mm/rev
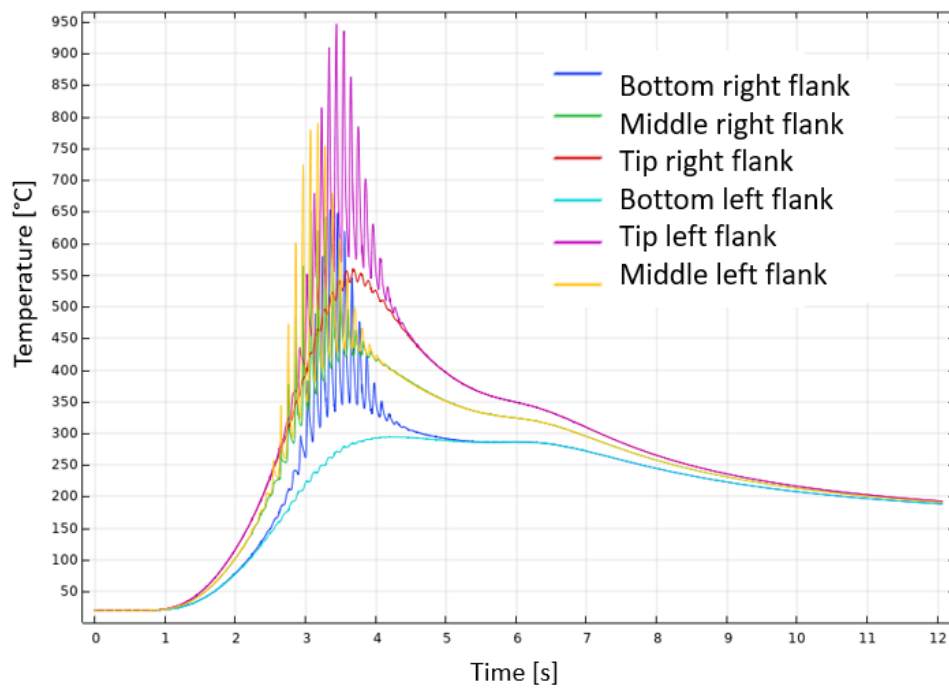
Figure 98. Calculated temperatures in function of the time in correspondence of the tip, middle and bottom flank using the harder wheel N13 with f =0,34 mm/rev
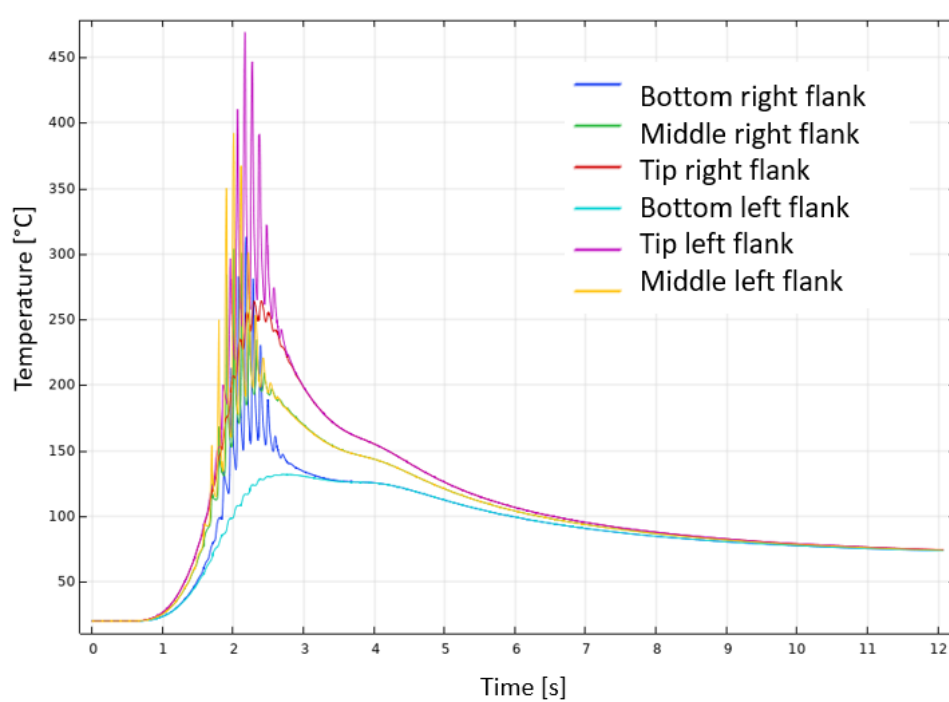


Figure 99. Calculated temperatures in function of the time in correspondence of the tip, middle and bottom flank using the softer wheel I11 with f =0,54 mm/rev
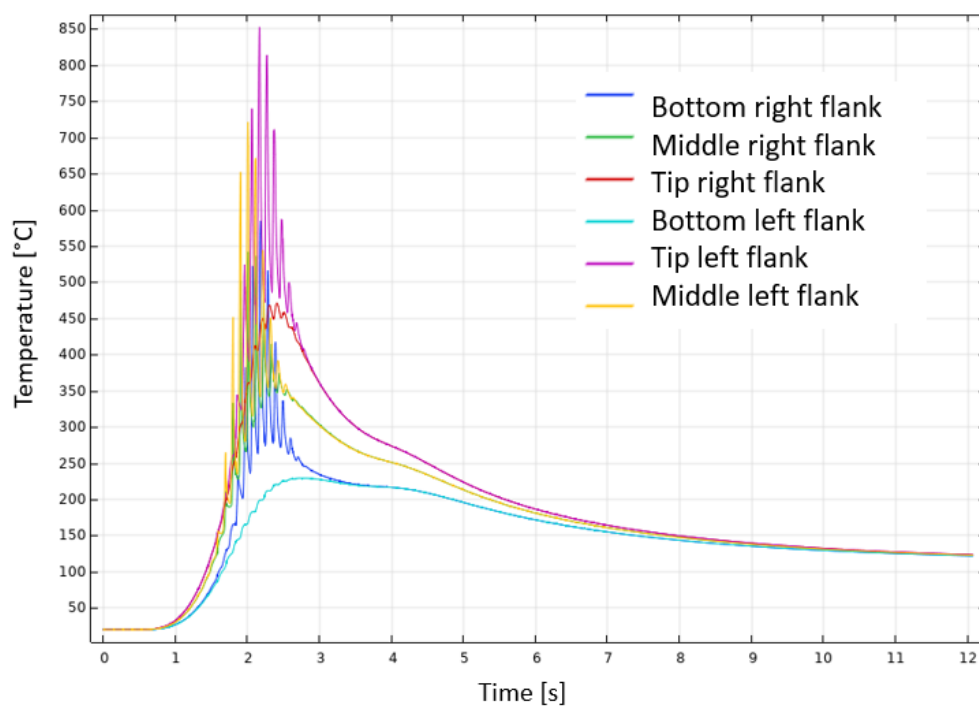
Figure 100. Calculated temperatures in function of the time in correspondence of the tip, middle and bottom flank using the harder wheel N13 with f =0,54 mm/rev

At equal other grinding conditions, the harder grinding wheel showed the most remarkable thermal defect, because for each feed rate levels the white layer occurred. Indeed, the maximum temperatures calculated were 950°C and 850 °C, respectively. While, with the softer grinding wheel, maximum temperature reached was equal to 570 °C with a feed rate of 0,34 mm/rev causing the occurrence of a darkened layer, instead, increasing the feed rate to 0,54 mm/rev no thermal defect seems appear at the flank surface, being the maximum temperature reached equal to 460°C.

It is important to notice that, compared to the tangential grinding process, within the grinding process applied on gears the initiation of the darkened layer at the surface starts at higher temperature values, around 550 °C, instead at 450°C no thermal defects seem appear yet. This could be due to the fact that, in the gear grinding process, the interaction time for each grinding pass lasts ten times less, therefore, according with the ultra-fast heating process theory, to reach the microstructural change it would need a higher temperature threshold. This is confirmed also to the fact that when the white and darkened layer appear, they affect a very lower surface thickness on the tooth flank compared to the tangential grinding tests.

Gears dry grinding feasibility was also evaluated by analyzing teeth flanks dimensional tolerances and roughness and compared with the reference wet grinding process performed on the same gear. Measurements were detected by using a standard gear inspection instrument which was set up with the gear geometric requirements reported in the technical drawing. In Figure 101Figure 102Figure 103Figure 104, the shape of the tooth along the profile and the helix as ground were reported for each dry grinding configurations, instead Figure 105 showed the reference wet grinding process outcomes. Dimensional measurements showed the shape obtained after grinding on four different teeth equally spaced on both left and right flank. Overall, the graphs showed a smooth and regular shape for all grinding configurations comparable to a reference wet grinding process suggesting a correct finishing phase for each set up from the geometrical point of view.
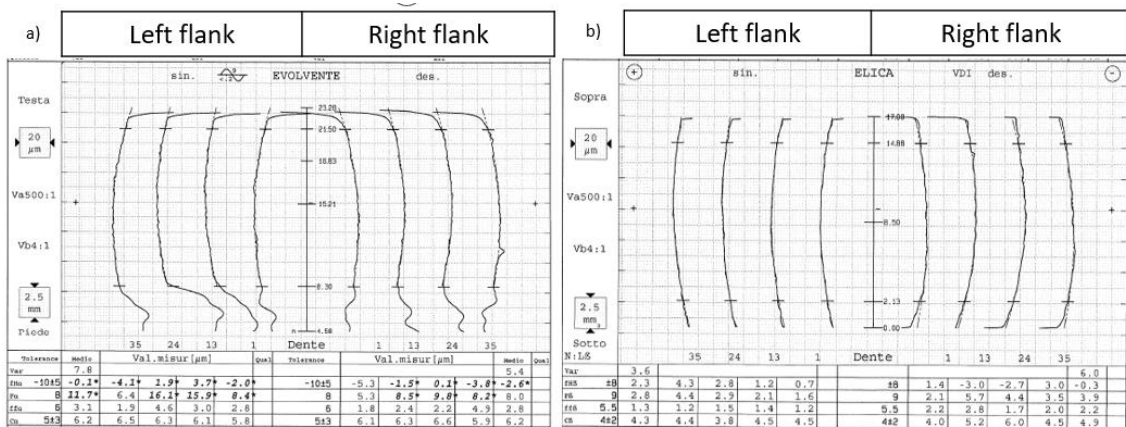
Figure 101. Dimensional tolerances measurement for the dry-hard finishing process using the I11 wheel with $f$ = 0,34 mm/rev: a) tooth profile; b) tooth lead
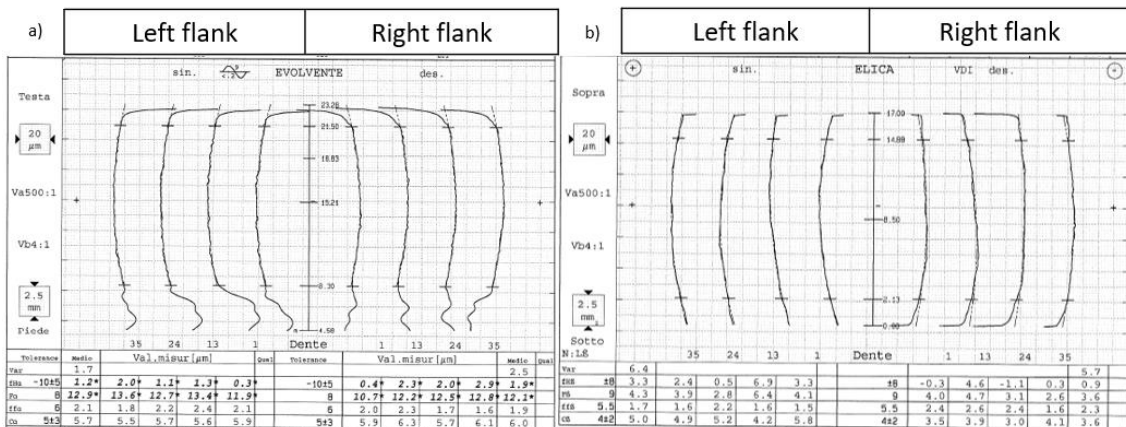
Figure 102. Dimensional tolerances measurement for the dry-hard finishing process using the I11 wheel with f = 0,54 mm/rev: a) tooth profile; b) tooth lead
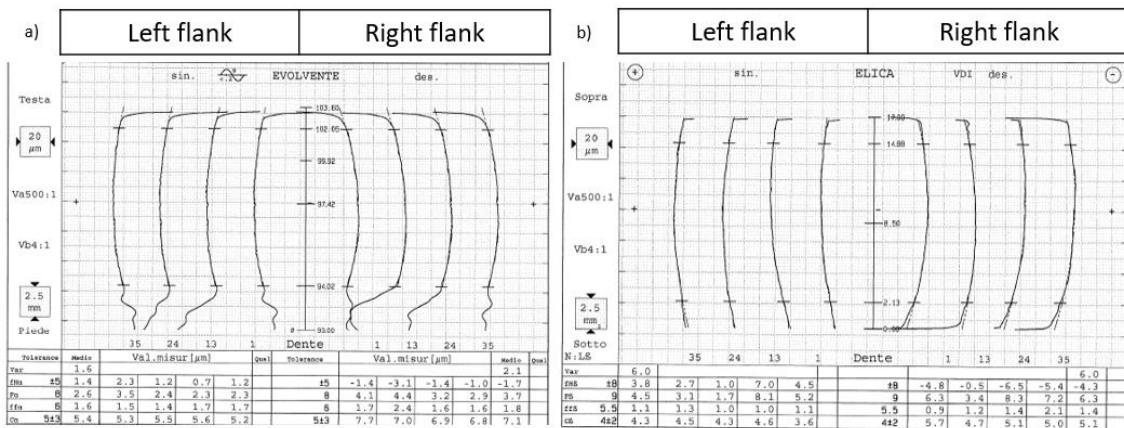
Figure 103. Dimensional tolerances measurement for the dry-hard finishing process using the N13 wheel with f = 0,34 mm/rev: a) tooth profile; b) tooth lead
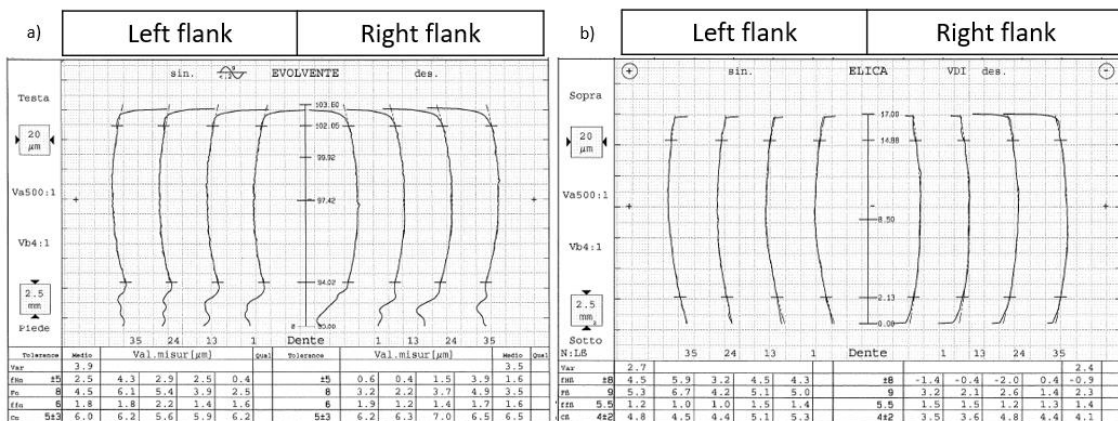


Figure 104. Dimensional tolerances measurement for the dry-hard finishing process using the N13 wheel with f = 0,54 mm/rev: a) tooth profile; b) tooth lead
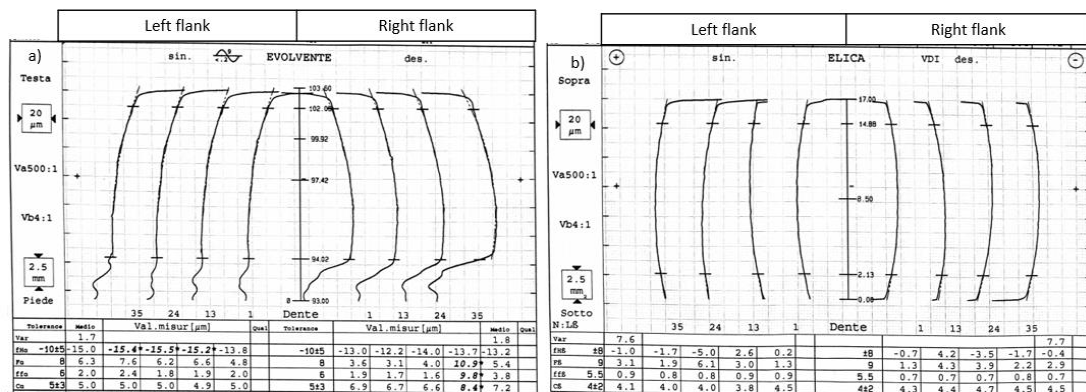


Figure 105. Dimensional tolerances measurement for the reference conventional wet grinding process: a) tooth profile; b) tooth lead

In Figure 106Figure 107Figure 108 the comparison on the profile and helix form error and the helix crowning between the different grinding wheel in function of the feed rate was reported. The graphs reported the measurements for both right and left flank. According with the dimensional range reported in Table 12 all the set up respected the tolerances requirements. Considering the comparison between the softer and harder wheels, the harder one tends to reach lower values compared to the softer one indicating a reduced shape error, instead no remarkable differences were detected considering the feed rate.
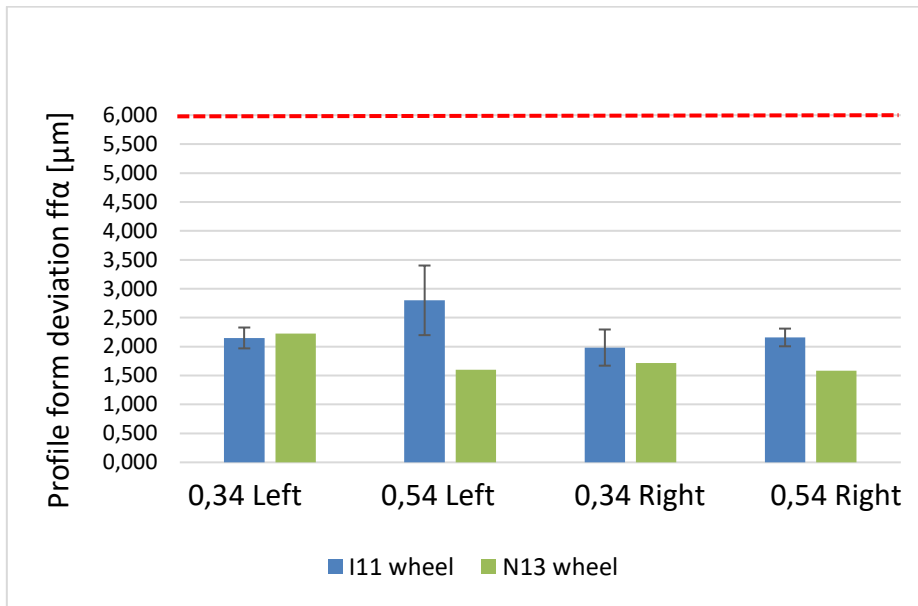


Figure 106. Profile form deviation comparison between I11 and N13 wheels in function of the feed rate
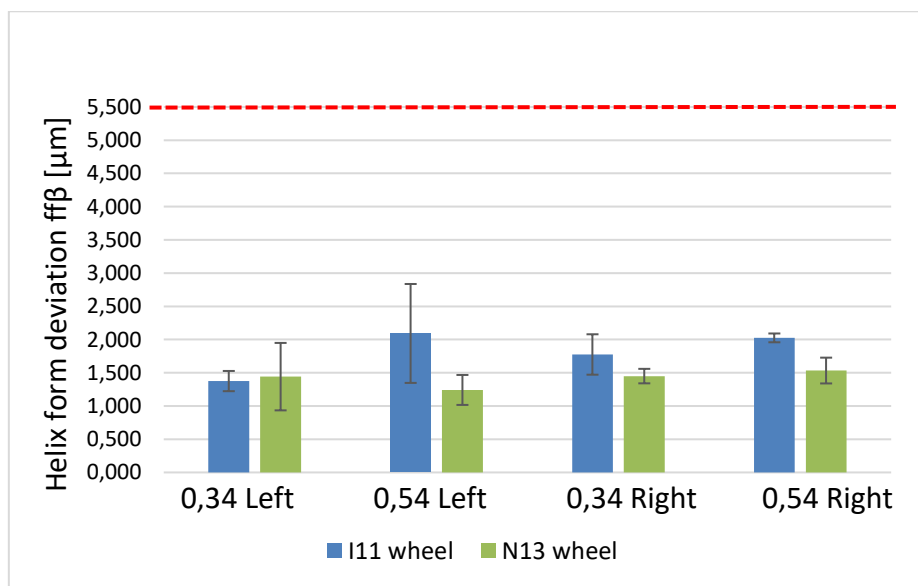


Figure 107. Helix form deviation comparison between I11 and N13 wheels in function of the feed rate
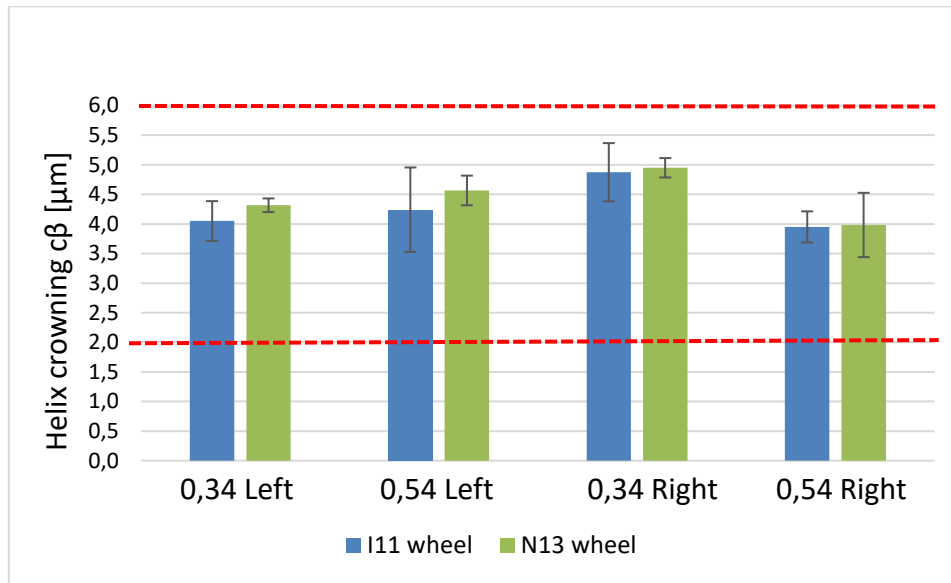
Figure 108. Helix crowning comparison between I11 and N13 wheels in function of the feed rate

Figure 109Figure 110 showed the roughness results by comparing the effect of the grinding wheel specifications and the feed rate on the profile and on the helix. First, it is possible to notice that the left flank showed a slightly higher roughness value, probably due to the previous dressing procedure. Same dressing parameters were adopted for the grinding wheels. Considering the profile roughness, the values detected are comparable with the reference obtained through the conventional wet grinding process that is around 0.4 µm. But with the grinding wheel characterized with the harder binder, the roughness reaches a lower value with an average of 0.25 µm. Moreover, increasing the feed rate the roughness increases. Analysing the helix roughness and considering the standard deviation, the same trend is visible, especially on the left flank. In this case, the roughness obtained with the harder wheel is comparable with the reference that is around 0.2 µm, instead, the value reached with the softer wheel is higher and around 0.3 µm. Roughness values measured respected the requirements reported in Table 12 in all cases. The harder grinding wheel tend to maintain a more stable trace on the gear teeth compared to the softer one, but the thermal effect on the microstructures does not allow to choose it as the best solution.
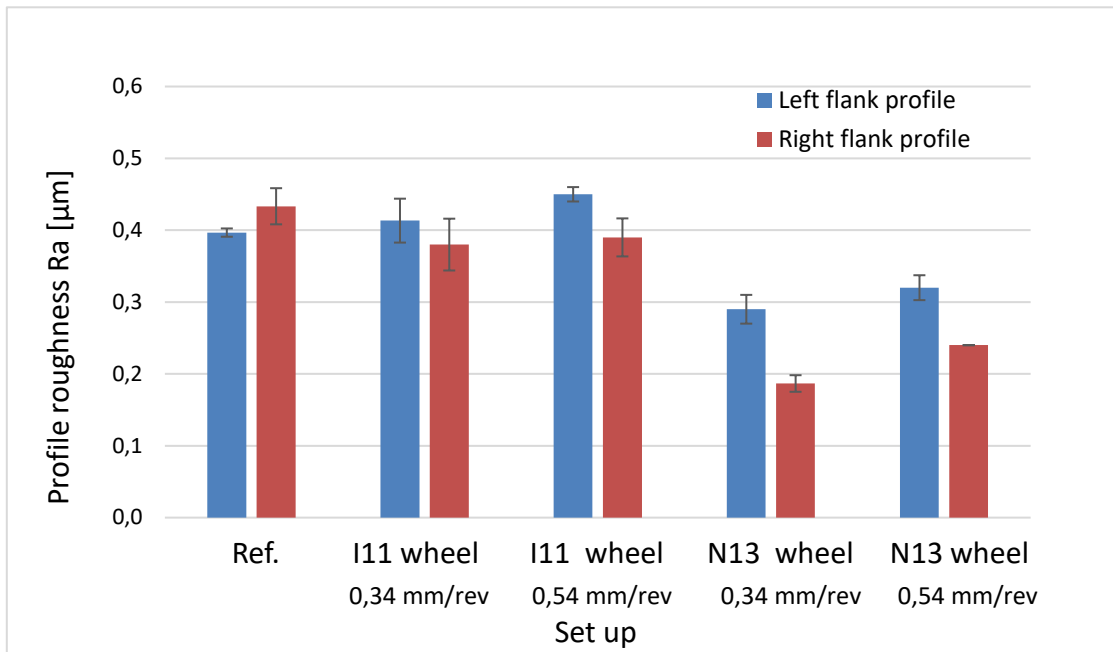
Figure 109. Profile roughness Ra comparison
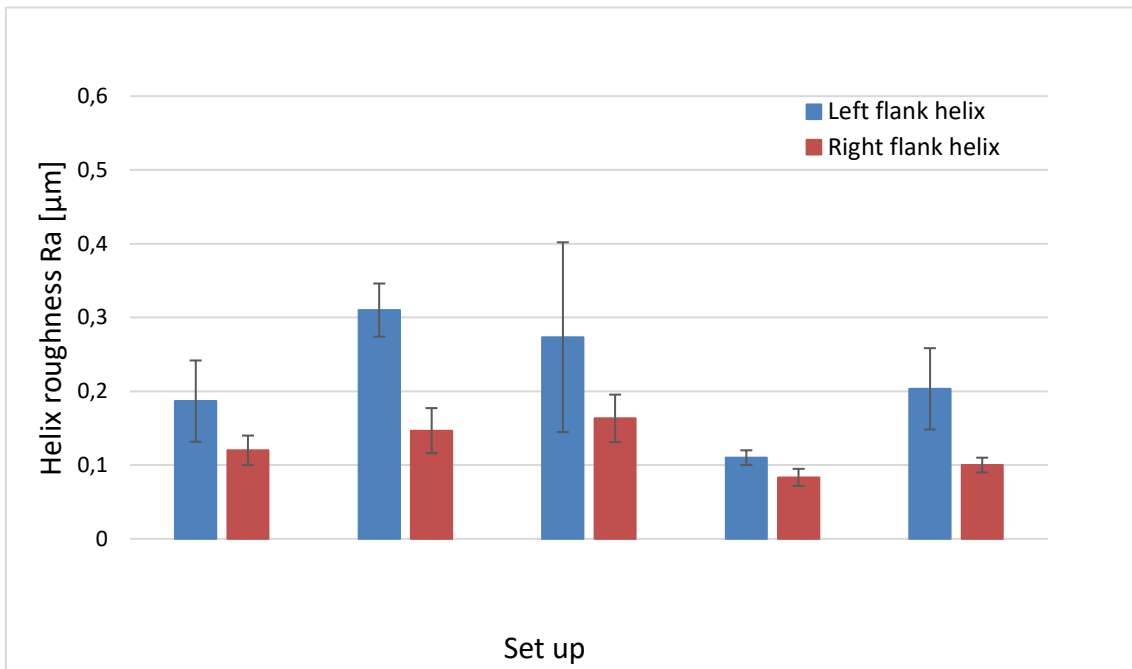


Figure 110. Helix roughness Ra comparison

# Conclusions

The PhD activities aimed at creating and optimizing a model able to predict the thermal effects and the wheel specification influence in a dry grinding process on case-hardened material typically used in gears manufacturing. A hierarchical FEM model avoiding several time-consuming experimental power measurements was presented. A single grain grinding model was developed to analyze the interaction between a single abrasive grain and the material and was validated through forces measurements allowing to calculate specific grinding power. The main results related to the single grain grinding model can be summarized as follows:

- as the simulation of real grain geometry was time-consuming, an equivalent defined grain geometry was implemented by considering the principal abrasives characteristics. Good alignment between real and equivalent defined geometry was observed, implying that real grain geometry can be simplified and replaced with defined grain geometry.

- an inverse simulation-based method was applied to identify the most suitable Johnson & Cook material coefficients for the hardened depth of an automotive gear case-hardened steel. Different combinations of J&C coefficients were analyzed with the aim at achieving target reductions in tangential and normal forces. With the most suitable set of flow stress coefficients defined, the single grit grinding process was simulated with the previously defined grain geometry to check the calibration of the material flow stress model. Good agreement was observed between calculated and measured tangential and normal forces with a maximum percentage difference of 13%.

- A further test and simulation were implemented adopting the same process parameters to validate the model and new flow stress curve for a different grain geometry, confirming good alignment with the experimental results achieving a maximum percentage difference of 12%.

- The single grain grinding power was then calculated considering an equivalent defined abrasive shape representative for the sintered aluminum oxide size 60 and it was shown that it is directly dependent by the depth of cut and feed rate, but the

166

cutting depth was detected being the most influencing kinematic grinding parameter.

A correlated following thermal model was proposed to consider the interaction between the entire grinding wheel and the material in a tangential grinding process. A moving heat source was developed considering the contact area between the wheel and the material and the wheel specifications in terms of abrasive grains density. Three grinding wheel structures and two binder hardness levels were compared at equal grinding conditions to validate the model and show the different grinding wheel specification influence on the material. Thermal defects were forecasted analyzing the maximum temperature reached during the process and the model was validated, at first, by means of tangential grinding experiments and temperature measurements by adopting embedded thermocouples and then through microstructural and micro-hardness analysis on prismatic samples. The thermal effect of the grinding process is correlated to the moving heat source amplitude which was designed in function of the grain grinding power, the contact surfaces and the abrasive grains density. The main results related to the tangential grinding model can be summarized in the following points:

- From a combined analytical and experimental evaluation of the grinding wheel specification it was identified a reducing grains density considering an increasing structure and a softer hardness binder.
- The model was validated considering that the average percentage differences between the measured and calculated temperatures was detected equal to 4%, 9.8% and 10.8% respectively for the thermocouples positioned at 0.25, 0.5 and 1 mm from the surface considering all the wheel specifications.
- Considering the grinding wheel specification effect, it was shown a reduction of the grinding temperature by increasing the porosity and using a softer binder. A decrease of 33% and 9.5% was detected between the low-medium porous wheels and medium-high porous wheels respectively. Instead, a maximum reduction of 20.5% was achieved by introducing a one grade softer binder hardness.
- Microstructural and micro-hardness measurements were compared with the maximum temperatures calculated. It was verified that in a tangential grinding process a darkened layer occurs when a temperature about 400 °C was reached,

instead, the white layer occurrence was detected overcoming the austenitization temperature of 723 °C.

- Comparing the surface micro-hardness of the reference material with the microstructure reached in the dry grinding tests, it was shown an increase of 16% of surface hardness with the low and medium porosity and a reduction of 25% and 37 % respectively with the high porosity and softer binder wheel.

Subsequently, the model was applied to the gear tooth geometry introducing the gear generating grinding kinematics and the model temperature outcomes were compared with the thermal effect detected on the gear flank microstructures resulting from the use of two different grinding wheels in the industrial gear dry grinding process. The main results related to the gear grinding model can be summarized in the following points:

- A white and darkened layer occurs removing 0.01 mm of depth of cut using the harder grinding wheel for each feed rate levels. Good agreement was achieved by implementing the model, indeed, the maximum temperatures calculated overcome the austenitization temperature reaching 950°C and 850 °C, respectively. While, with the softer grinding wheel, maximum temperature reached was equal to 570 °C with a feed rate of 0,34 mm/rev causing the initiation of a darkened layer, instead, increasing the feed rate to 0,54 mm/rev no thermal defect seems appear at the flank surface and the maximum temperature calculated was equal to 460°C.

- Compared to the tangential grinding process, the grinding process applied on the gear's geometry led to the initiation of the darkened layer occurrence at higher temperature values, around 550 °C, instead at 450°C no thermal defects seem appear yet. Indeed, according with the ultra-fast heating process theory, since the interaction time between the wheel and the material for each grinding pass is lower than the tangential grinding process, to reach the microstructural change it would need a higher temperature threshold.

- Within the grinding conditions analyzed, although the harder wheel showed the best roughness values and presents a slightly higher porosity is not able to avoid grinding burns. Indeed, at equal grinding parameters set, the softer binder allows to reduce the thermal effect due to the dry grinding process, especially increasing the feed rate, being the interaction time between the wheel and the material lower.

The proposed model has yielded encouraging results in forecasting the thermal defects induced by the gear dry grinding process taking in consideration all the technological process parameters. However, the model reliability could be increased by performing further grinding tests and investigating on new grinding burns detection methods. Anyway, the proposed approach provides a good starting point for the dry-hard finishing process assessment which has been shown to be able to achieve comparable surface quality results with the conventional wet process in terms of microstructure, dimensional tolerances and roughness.

# References

[1]     J. W. McAuley, "Global Sustainability and Key Needs in Future Automotive Design," *Environ. Sci. Technol.*, vol. 37, no. 23, pp. 5414–5416, 2003, doi: 10.1021/es030521x.

[2]     A. Mayyas, A. Qattawi, M. Omar, and D. Shan, "Design for sustainability in automotive industry: A comprehensive review," *Renew. Sustain. Energy Rev.*, vol. 16, no. 4, pp. 1845–1862, 2012, doi: 10.1016/j.rser.2012.01.012.

[3]     R. J. Orsato and P. Wells, "The Automobile Industry & Sustainability," *J. Clean. Prod.*, vol. 15, no. 11–12, pp. 989–993, 2007, doi: 10.1016/j.jclepro.2006.05.035.

[4]     J. C. González Palencia, T. Sakamaki, M. Araki, and S. Shiga, "Impact of powertrain electrification, vehicle size reduction and lightweight materials substitution on energy use, CO2 emissions and cost of a passenger light-duty vehicle fleet," *Energy*, vol. 93, pp. 1489–1504, 2015, doi: 10.1016/j.energy.2015.10.017.

[5]     E. Pallaro, N. Subramanian, M. D. Abdulrahman, and C. Liu, "Sustainable production and consumption in the automotive sector: Integrated review framework and research directions," *Sustain. Prod. Consum.*, vol. 4, no. April, pp. 47–61, 2015, doi: 10.1016/j.spc.2015.07.002.

[6]     G. Kotthoff, "NVH Potential of PM Gears for Electrified Drivetrains," *Gear Technol.*, no. October, p. 4, 2018.

[7]     G. Lechner and N. Harald, "Automotive transmissions." p. 469, 1999.

[8]     IHS Markit, "Global Light Vehicle Production Summary," *IHS Markit*, no. January 2019, p. 1, 2019.

[9]     G. Hyatt, M. Piber, N. Chaphalkar, O. Kleinhenz, and M. Mori, "A review of new strategies for gear production," *Procedia CIRP*, vol. 14, pp. 72–76, 2014, doi: 10.1016/j.procir.2014.03.034.

[10]    R. Singh, "Progress of environment friendly cutting fluids/solid lubricants in turning-A review," *Mater. Today Proc.*, vol. 37, no. Part 2, pp. 3577–3580, 2020, doi: 10.1016/j.matpr.2020.09.585.

[11]    M. Li *et al.*, "Experimental evaluation of an eco-friendly grinding process combining minimum quantity lubrication and graphene-enhanced plant-oil-based cutting fluid," *J. Clean. Prod.*, no. xxxx, p. 118747, 2019, doi: 10.1016/j.jclepro.2019.118747.

[12]    L. O. B. De Sampaio Alves *et al.*, "Performance evaluation of the minimum quantity of lubricant technique with auxiliary cleaning of the grinding wheel in cylindrical grinding of N2711 Steel," *J. Manuf. Sci. Eng. Trans. ASME*, vol. 139, no. 12, pp. 1–8, 2017, doi: 10.1115/1.4037041.

[13]    K. Gupta, R. F. Laubscher, J. P. Davim, and N. K. Jain, "Recent developments in sustainable manufacturing of gears: A review," *J. Clean. Prod.*, vol. 112, pp.

3320–3330, 2016, doi: 10.1016/j.jclepro.2015.09.133.

[14]  G. S. Goindi and P. Sarkar, "Dry machining: A step towards sustainable machining – Challenges and future directions," *J. Clean. Prod.*, vol. 165, pp. 1557–1571, 2017, doi: 10.1016/j.jclepro.2017.07.235.

[15]  C. Kobialka, "Complete machining of gear blank and gear teeth," *Am. Gear Manuf. Assoc. Fall Tech. Meet. 2010*, pp. 1–8, 2010.

[16]  J. F. G. Oliveira, E. J. Silva, C. Guo, and F. Hashimoto, "Industrial challenges in grinding," *CIRP Ann. - Manuf. Technol.*, vol. 58, no. 2, pp. 663–680, 2009, doi: 10.1016/j.cirp.2009.09.006.

[17]  E. Brinksmeier, C. Heinzel, and M. Wittmann, "Friction, cooling and lubrication in grinding," *CIRP Ann. - Manuf. Technol.*, vol. 48, no. 2, pp. 581–598, 1999, doi: 10.1016/S0007-8506(07)63236-3.

[18]  G. Guerrini, E. Landi, K. Peiffer, and A. Fortunato, "Dry grinding of gears for sustainable automotive transmission production," *J. Clean. Prod.*, vol. 176, pp. 76–88, 2018, doi: 10.1016/j.jclepro.2017.12.127.

[19]  E. Landi, "Changing the Game with an Innovative Machine Concept : Dry Hard-Gear Finishing," *Gear Solut.*, pp. 48–51, 2016.

[20]  K. Gupta, N. K. Jain, and R. Laubscher, *Introduction to Gear Engineering*. 2017.

[21]  E. Fortunato, A. Ascari, A. Liverani, "Introduzione alle macchine utensili."

[22]  K. D. Bouzakis, E. Lili, N. Michailidis, and O. Friderikos, "Manufacturing of cylindrical gears by generating cutting processes: A critical synthesis of analysis methods," *CIRP Ann. - Manuf. Technol.*, vol. 57, no. 2, pp. 676–696, 2008, doi: 10.1016/j.cirp.2008.09.001.

[23]  B. Karpuschewski, H. J. Knoche, and M. Hipke, "Gear finishing by abrasive processes," *CIRP Ann. - Manuf. Technol.*, vol. 57, no. 2, pp. 621–640, 2008, doi: 10.1016/j.cirp.2008.09.002.

[24]  W. Zhou, J. Tang, and W. Shao, "Study on surface generation mechanism and roughness distribution in gear profile grinding," *Int. J. Mech. Sci.*, vol. 187, no. June, p. 105921, 2020, doi: 10.1016/j.ijmecsci.2020.105921.

[25]  F. Klocke, M. Brumm, and J. Reimann, "Modeling of surface zone influences in generating gear grinding," *Procedia CIRP*, vol. 8, pp. 21–26, 2013, doi: 10.1016/j.procir.2013.06.059.

[26]  C. Brecher, F. Klocke, C. Löpenhaus, and F. Hübner, "Analysis of Abrasive Grit Cutting for Generating Gear Grinding," *Procedia CIRP*, vol. 62, pp. 299–304, 2017, doi: 10.1016/j.procir.2016.06.042.

[27]  T. R. Weir, "Manufacturing of gears," vol. 1:1,837,44, no. Manitoba, p. pate 34, 1960.

[28]  K. Wegener, F. Bleicher, P. Krajnik, H. W. Hoffmeister, and C. Brecher, "Recent developments in grinding machines," *CIRP Ann. - Manuf. Technol.*, vol. 66, no.

2, pp. 779–802, 2017, doi: 10.1016/j.cirp.2017.05.006.

[29]  H. K. Tönshoff, T. Friemuth, and J. C. Becker, "Process monitoring in grinding," *CIRP Ann. - Manuf. Technol.*, vol. 51, no. 2, pp. 551–571, 2002, doi: 10.1016/S0007-8506(07)61700-4.

[30]  J. P. D. M. J. Jackson, *Machining with abrasives*. 1967.

[31]  S. Malkin, *Theory and Applications*. 2008.

[32]  J. C. Aurich *et al.*, "Abrasive processes for micro parts and structures," *CIRP Ann.*, vol. 68, no. 2, pp. 653–676, 2019, doi: 10.1016/j.cirp.2019.05.006.

[33]  F. Klocke *et al.*, "Abrasive machining of advanced aerospace alloys and composites," *CIRP Ann. - Manuf. Technol.*, vol. 64, no. 2, pp. 581–604, 2015, doi: 10.1016/j.cirp.2015.05.004.

[34]  F. Hashimoto *et al.*, "Abrasive fine-finishing technology," *CIRP Ann. - Manuf. Technol.*, vol. 65, no. 2, pp. 597–620, 2016, doi: 10.1016/j.cirp.2016.06.003.

[35]  P. L. Tso and S. H. Wu, "Analysis of grinding quantities through chip sizes," *J. Mater. Process. Technol.*, vol. 95, no. 1–3, pp. 1–7, 1999, doi: 10.1016/S0924-0136(99)00297-6.

[36]  E. U. I. D. Marinescu, M. Hitchiner, *Handbook of Machining with grinding wheels*. .

[37]  Y. Ohbuchi and T. Obikawa, "Adiabatic shear in chip formation with negative rake angle," *Int. J. Mech. Sci.*, vol. 47, no. 9, pp. 1377–1392, 2005, doi: 10.1016/j.ijmecsci.2005.05.003.

[38]  B. Denkena and D. Biermann, "Cutting edge geometries," *CIRP Ann. - Manuf. Technol.*, vol. 63, no. 2, pp. 631–653, 2014, doi: 10.1016/j.cirp.2014.05.009.

[39]  W. B. Rowe and B. Dimitrov, *Tribology of Abrasive*. 2004.

[40]  F. Kempf, A. Bouabid, P. Dzierzawa, and B. Denkena, "Methods for the analysis of grinding wheel properties," pp. 87–96.

[41]  J. Webster and M. Tricard, "Innovations in abrasive products for precision grinding," *CIRP Ann. - Manuf. Technol.*, vol. 53, no. 2, pp. 597–617, 2004, doi: 10.1016/S0007-8506(07)60031-6.

[42]  H. Deng and Z. Xu, "Dressing methods of superabrasive grinding wheels: A review," *J. Manuf. Process.*, vol. 45, no. May, pp. 46–69, 2019, doi: 10.1016/j.jmapro.2019.06.020.

[43]  R. Dębkowski, "Experimental studies of heat dissipation by a stream of dressing products during dry dressing of conventional ceramic grinding wheels," *J. Manuf. Process.*, vol. 35, no. April, pp. 735–745, 2018, doi: 10.1016/j.jmapro.2018.09.010.

[44]  J. Böttger, S. Kimme, and W. G. Drossel, "Simulation of dressing process for continuous generating gear grinding," *Procedia CIRP*, vol. 79, pp. 280–285, 2019, doi: 10.1016/j.procir.2019.02.067.

[45] C. Heinzel and B. Kolkwitz, "The Impact of fluid supply on energy efficiency and process performance in grinding," *CIRP Ann.*, vol. 68, no. 1, pp. 337–340, 2019, doi: 10.1016/j.cirp.2019.03.023.

[46] W. H. T. D. Howes, H. K. Tonshoff, "Environmental Aspects of Grinding Fluids," vol. 40, pp. 623–630, 1991.

[47] S. Ravi, P. Gurusamy, and V. Mohanavel, "A review and assessment of effect of cutting fluids," *Mater. Today Proc.*, vol. 37, no. Part 2, pp. 220–222, 2020, doi: 10.1016/j.matpr.2020.05.054.

[48] R. L. Javaroni *et al.*, "Improvement in the grinding process using the MQL technique with cooled wheel cleaning jet," *Tribol. Int.*, vol. 152, no. December 2019, 2020, doi: 10.1016/j.triboint.2020.106512.

[49] W. F. Sales, J. Schoop, L. R. R. da Silva, Á. R. Machado, and I. S. Jawahir, "A review of surface integrity in machining of hardened steels," *J. Manuf. Process.*, vol. 58, no. August, pp. 136–162, 2020, doi: 10.1016/j.jmapro.2020.07.040.

[50] D. N. T. G. Bellows, "Introduction To Surface Integrity," vol. V 5, pp. 171–182, 1967.

[51] I. S. Jawahir *et al.*, "Surface integrity in material removal processes: Recent advances," *CIRP Ann. - Manuf. Technol.*, vol. 60, no. 2, pp. 603–626, 2011, doi: 10.1016/j.cirp.2011.05.002.

[52] E. Procedure, "Surface Layer Properties of the," vol. 51, no. 1, pp. 105–108, 2012.

[53] F. yuan Zhang, C. zheng Duan, M. jie Wang, and W. Sun, "White and dark layer formation mechanism in hard cutting of AISI52100 steel," *J. Manuf. Process.*, vol. 32, no. December 2017, pp. 878–887, 2018, doi: 10.1016/j.jmapro.2018.04.011.

[54] D. Mallipeddi, M. Norell, M. Sosa, and L. Nyborg, "The effect of manufacturing method and running-in load on the surface integrity of efficiency tested ground, honed and superfinished gears," *Tribol. Int.*, vol. 131, no. November 2018, pp. 277–287, 2019, doi: 10.1016/j.triboint.2018.10.051.

[55] H. He, H. Liu, C. Zhu, and J. Tang, "Study on the gear fatigue behavior considering the effect of residual stress based on the continuum damage approach," *Eng. Fail. Anal.*, vol. 104, no. June, pp. 531–544, 2019, doi: 10.1016/j.engfailanal.2019.06.027.

[56] M. Liu, K. Zhang, and S. Xiu, "Mechanism investigation of hardening layer hardness uniformity based on grind-hardening process," *Int. J. Adv. Manuf. Technol.*, vol. 88, no. 9–12, pp. 3185–3194, 2017, doi: 10.1007/s00170-016-9029-y.

[57] S. Papaefthymiou, A. Banis, M. Bouzouni, and R. H. Petrov, "Effect of ultra-fast heat treatment on the subsequent formation of mixed martensitic/bainitic microstructure with carbides in a crmo medium carbon steel," *Metals (Basel).*, vol. 9, no. 3, 2019, doi: 10.3390/met9030312.

[58] D. K. Matlock, S. Kang, E. De Moor, and J. G. Speer, "Applications of rapid thermal processing to advanced high strength sheet steel developments," *Mater. Charact.*, vol. 166, no. February, p. 110397, 2020, doi: 10.1016/j.matchar.2020.110397.

[59] E. Liverani, D. Sorgente, A. Ascari, L. D. Scintilla, G. Palumbo, and A. Fortunato, "Development of a model for the simulation of laser surface heat treatments with use of a physical simulator," *J. Manuf. Process.*, vol. 26, pp. 262–268, 2017, doi: 10.1016/j.jmapro.2017.02.023.

[60] J. R. Davis, "GEAR MATERIALS , PROPERTIES , AND MANUFACTURE," *Production*, p. 339, 2005.

[61] M. Knyazeva *et al.*, "Micro-magnetic and microstructural characterization of wear progress on case-hardened 16MnCr5 gear wheels," *Materials (Basel).*, vol. 11, no. 11, 2018, doi: 10.3390/ma11112290.

[62] X. Xu, J. Lai, C. Lohmann, P. Tenberge, M. Weibring, and P. Dong, "A model to predict initiation and propagation of micro-pitting on tooth flanks of spur gears," *Int. J. Fatigue*, vol. 122, no. December 2018, pp. 106–115, 2019, doi: 10.1016/j.ijfatigue.2019.01.004.

[63] J. Kattelus, J. Miettinen, and A. Lehtovaara, "Detection of gear pitting failure progression with on-line particle monitoring," *Tribol. Int.*, vol. 118, no. February 2017, pp. 458–464, 2018, doi: 10.1016/j.triboint.2017.02.045.

[64] B. He, C. Wei, S. Ding, and Z. Shi, "A survey of methods for detecting metallic grinding burn," *Meas. J. Int. Meas. Confed.*, vol. 134, pp. 426–439, 2019, doi: 10.1016/j.measurement.2018.10.093.

[65] BS ISO 14104: 2017, "Standards Publication Gears - Surface temper etch inspection after grinding , chemical method," 2017.

[66] M. Liu, T. Nguyen, L. Zhang, Q. Wu, and D. Sun, "Effect of grinding-induced cyclic heating on the hardened layer generation in the plunge grinding of a cylindrical component," *Int. J. Mach. Tools Manuf.*, vol. 89, pp. 55–63, 2015, doi: 10.1016/j.ijmachtools.2014.11.003.

[67] J. Liu, W. Yuan, S. Huang, and Z. Xu, "Experimental Study on Grinding-hardening of 1060 Steel," *Energy Procedia*, vol. 16, pp. 103–108, 2012, doi: 10.1016/j.egypro.2012.01.019.

[68] J. E. Mayer, A. H. Price, G. K. Purushothaman, A. K. Dhayalan, and M. S. Pepi, "Specific grinding energy causing thermal damage in helicopter gear steel," *J. Manuf. Process.*, vol. 4, no. 2, pp. 142–147, 2002, doi: 10.1016/S1526-6125(02)70140-0.

[69] U. Alonso, N. Ortega, J. A. Sanchez, I. Pombo, B. Izquierdo, and S. Plaza, "Hardness control of grind-hardening and finishing grinding by means of area-based specific energy," *Int. J. Mach. Tools Manuf.*, vol. 88, pp. 24–33, 2015, doi: 10.1016/j.ijmachtools.2014.09.001.

[70] D. Hou, S. Gao, J. Liu, and S. Huang, "Effect of Grinding Parameters on the

Hardness Penetration Depth of the Steel GCr15 in Internal Grind Hardening Process," *J. Phys. Conf. Ser.*, vol. 1637, no. 1, 2020, doi: 10.1088/1742-6596/1637/1/012112.

[71]   Y. Guo, M. Liu, M. Yin, and Y. Yan, "Modeling of the evolution of the microstructure and the hardness penetration depth for a hypoeutectoid steel processed by grind-hardening," *Metals (Basel).*, vol. 10, no. 9, pp. 1–17, 2020, doi: 10.3390/met10091182.

[72]   B. Eigenmann, A. Zösch, and M. Seidel, "Sensitivity of macro-and micro-residual stress states of steel surfaces to thermal influences caused by grinding burn and laser treatments," *Mater. Sci. Forum*, vol. 768–769, pp. 412–419, 2014, doi: 10.4028/www.scientific.net/MSF.768-769.412.

[73]   K. Salonitis, "On surface grind hardening induced residual stresses," *Procedia CIRP*, vol. 13, pp. 264–269, 2014, doi: 10.1016/j.procir.2014.04.045.

[74]   X. Huang, Y. Ren, W. Wu, and T. Li, "Research on grind-hardening layer and residual stresses based on variable grinding forces," *Int. J. Adv. Manuf. Technol.*, vol. 103, no. 1–4, pp. 1045–1055, 2019, doi: 10.1007/s00170-019-03329-6.

[75]   M. K. Sinha, D. Setti, S. Ghosh, and P. Venkateswara Rao, "An investigation on surface burn during grinding of Inconel 718," *J. Manuf. Process.*, vol. 21, no. January, pp. 124–133, 2016, doi: 10.1016/j.jmapro.2015.12.004.

[76]   F. Delaunay, C. Berthier, M. Lenglet, and J. M. Lameille, "SEM-EDS and XPS studies of the high temperature oxidation behaviour of Inconel 718," *Mikrochim. Acta*, vol. 132, no. 2–4, pp. 337–343, 2000, doi: 10.1007/s006040050027.

[77]   V. Moorthy and B. A. Shaw, "Magnetic Barkhausen emission measurements for evaluation of material properties in gears," *Nondestruct. Test. Eval.*, vol. 23, no. 4, pp. 317–347, 2008, doi: 10.1080/10589750802275980.

[78]   J. Heinzel, R. Jedamski, J. Epp, and B. Karpuschewski, "In-process measurement of Barkhausen noise and resulting productivity increase potential in grinding of case hardened steel," *CIRP J. Manuf. Sci. Technol.*, vol. 32, pp. 37–45, 2021, doi: 10.1016/j.cirpj.2020.11.011.

[79]   D. Sackmann, B. Karpuschewski, J. Epp, and R. Jedamski, "Detection of surface damages in ground spur gears by non-destructive micromagnetic methods," *Forsch. im Ingenieurwesen/Engineering Res.*, vol. 83, no. 3, pp. 563–570, 2019, doi: 10.1007/s10010-019-00368-z.

[80]   X. Chen and T. T. Öpöz, "Effect of different parameters on grinding efficiency and its monitoring by acoustic emission," *Prod. Manuf. Res.*, vol. 4, no. 1, pp. 190–208, 2016, doi: 10.1080/21693277.2016.1255159.

[81]   Q. Liu, X. Chen, and N. Gindy, "Investigation of acoustic emission signals under a simulative environment of grinding burn," *Int. J. Mach. Tools Manuf.*, vol. 46, no. 3–4, pp. 284–292, 2006, doi: 10.1016/j.ijmachtools.2005.05.017.

[82]   E. Brinksmeier *et al.*, "Advances in modeling and simulation of grinding processes," *CIRP Ann. - Manuf. Technol.*, vol. 55, no. 2, pp. 667–696, 2006, doi:

10.1016/j.cirp.2006.10.003.

[83] J. P. H.K.Tonshoff, "Modelling and simulation of grinding processes," *Filtr. Sep.*, vol. 37, no. 9, pp. 24–26, 2000, doi: 10.1016/S0015-1882(00)80196-2.

[84] V. K. Mishra and K. Salonitis, "Empirical estimation of grinding specific forces and energy based on a modified werner grinding model," *Procedia CIRP*, vol. 8, pp. 287–292, 2013, doi: 10.1016/j.procir.2013.06.104.

[85] D. Aslan and E. Budak, "Semi-analytical force model for grinding operations," *Procedia CIRP*, vol. 14, pp. 7–12, 2014, doi: 10.1016/j.procir.2014.03.073.

[86] U. S. Patnaik Durgumahanti, V. Singh, and P. Venkateswara Rao, "A New Model for Grinding Force Prediction and Analysis," *Int. J. Mach. Tools Manuf.*, vol. 50, no. 3, pp. 231–240, 2010, doi: 10.1016/j.ijmachtools.2009.12.004.

[87] V. Pandiyan, S. Shevchik, K. Wasmer, S. Castagne, and T. Tjahjowidodo, "Modelling and monitoring of abrasive finishing processes using artificial intelligence techniques: A review," *J. Manuf. Process.*, vol. 57, no. June, pp. 114–135, 2020, doi: 10.1016/j.jmapro.2020.06.013.

[88] L. Lv, Z. Deng, T. Liu, Z. Li, and W. Liu, "Intelligent technology in grinding process driven by data: A review," *J. Artif. Intell. Res.*, vol. 16, no. January, pp. 321–357, 2002, doi: 10.1016/j.jmapro.2020.09.018.

[89] S. Bin Wang and C. F. Wu, "Selections of working conditions for creep feed grinding. Part(III): Avoidance of the workpiece burning by using improved BP neural network," *Int. J. Adv. Manuf. Technol.*, vol. 28, no. 1–2, pp. 31–37, 2006, doi: 10.1007/s00170-004-2343-9.

[90] A. P. Markopoulos and J. Kundrák, "FEM/AI models for the simulation of precision grinding," *Manuf. Technol.*, vol. 16, no. 2, pp. 384–390, 2016, doi: 10.21062/ujep/x.2016/a/1213-2489/mt/16/2/384.

[91] J. A. Badger and A. A. Torrance, "Comparison of two models to predict grinding forces from wheel surface topography," *Int. J. Mach. Tools Manuf.*, vol. 40, no. 8, pp. 1099–1120, 2000, doi: 10.1016/S0890-6955(99)00116-9.

[92] R. L. Hecker, S. Y. Liang, X. J. Wu, P. Xia, and D. G. W. Jin, "Grinding force and power modeling based on chip thickness analysis," *Int. J. Adv. Manuf. Technol.*, vol. 33, no. 5–6, pp. 449–459, 2007, doi: 10.1007/s00170-006-0473-y.

[93] H. C. Chang and J. J. J. Wang, "A stochastic grinding force model considering random grit distribution," *Int. J. Mach. Tools Manuf.*, vol. 48, no. 12–13, pp. 1335–1344, 2008, doi: 10.1016/j.ijmachtools.2008.05.012.

[94] H. W. Park and S. Y. Liang, "Force modeling of microscale grinding process incorporating thermal effects," *Int. J. Adv. Manuf. Technol.*, vol. 44, no. 5–6, pp. 476–486, 2009, doi: 10.1007/s00170-008-1852-3.

[95] J. Tang, J. Du, and Y. Chen, "Modeling and experimental study of grinding forces in surface grinding," *J. Mater. Process. Technol.*, vol. 209, no. 6, pp. 2847–2854, 2009, doi: 10.1016/j.jmatprotec.2008.06.036.

[96]  V. Singh, P. Venkateswara Rao, and S. Ghosh, "Development of specific grinding energy model," *Int. J. Mach. Tools Manuf.*, vol. 60, pp. 1–13, 2012, doi: 10.1016/j.ijmachtools.2011.11.003.

[97]  H. N. Li, T. B. Yu, Z. X. Wang, L. Da Zhu, and W. S. Wang, "Detailed modeling of cutting forces in grinding process considering variable stages of grain-workpiece micro interactions," *Int. J. Mech. Sci.*, vol. 126, no. May 2016, pp. 319–339, 2017, doi: 10.1016/j.ijmecsci.2016.11.016.

[98]  Y. Zhang *et al.*, "Analysis of grinding mechanics and improved predictive force model based on material-removal and plastic-stacking mechanisms," *Int. J. Mach. Tools Manuf.*, vol. 122, no. January, pp. 81–97, 2017, doi: 10.1016/j.ijmachtools.2017.06.002.

[99]  M. Yang *et al.*, "Predictive model for minimum chip thickness and size effect in single diamond grain grinding of zirconia ceramics under different lubricating conditions," *Ceram. Int.*, vol. 45, no. 12, pp. 14908–14920, 2019, doi: 10.1016/j.ceramint.2019.04.226.

[100] B. S. Linke, I. Garretson, F. Torner, and J. Seewig, "Grinding energy modeling based on friction, plowing, and shearing," *J. Manuf. Sci. Eng. Trans. ASME*, vol. 139, no. 12, pp. 1–11, 2017, doi: 10.1115/1.4037239.

[101] S. Malkin and C. Guo, "Thermal Analysis of Grinding," *CIRP Ann. - Manuf. Technol.*, vol. 56, no. 2, pp. 760–782, 2007, doi: 10.1016/j.cirp.2007.10.005.

[102] C. Guo and S. Malkin, "Energy partition and cooling during grinding," *J. Manuf. Process.*, vol. 2, no. 3, pp. 151–157, 2000, doi: 10.1016/S1526-6125(00)70116-2.

[103] M. N. Morgan and B. Mills, "A Simplified Approach," vol. 45, no. 1, 1996.

[104] W. B. Rowe, J. A. Pettit, A. Boyle, and J. L. Moruzzi, "Avoidance of Thermal Damage in Grinding and Prediction of the Damage Threshold," *CIRP Ann. - Manuf. Technol.*, vol. 37, no. 1, pp. 327–330, 1988, doi: 10.1016/S0007-8506(07)61646-1.

[105] C. Heinzel, J. Sölter, S. Jermolajev, B. Kolkwitz, and E. Brinksmeier, "A versatile method to determine thermal limits in grinding," *Procedia CIRP*, vol. 13, pp. 131–136, 2014, doi: 10.1016/j.procir.2014.04.023.

[106] N. Rüttimann, M. Roethlin, S. Buhl, and K. Wegener, "Simulation of hexa-octahedral diamond grain cutting tests using the SPH method," *Procedia CIRP*, vol. 8, pp. 322–327, 2013, doi: 10.1016/j.procir.2013.06.110.

[107] N. RUTTIMANN, S. BUHL, and K. WEGENER, "Simulation of Single Grain Cutting Using Sph Method," *J. Mach. Eng.*, vol. 10, no. 3, pp. 17–29, 2010.

[108] R. D. Shen, X. M. Wang, and C. H. Yang, "Coupled FE-SPH simulation of a high-speed grinding process using a multiple-grain model," *Adv. Mater. Res.*, vol. 989–994, pp. 3248–3251, 2014, doi: 10.4028/www.scientific.net/AMR.989-994.3248.

[109] D. Julean, "SPH Simulation of single grain action in grinding," *MATEC Web Conf.*, vol. 137, 2017, doi: 10.1051/matecconf/201713703006.

[110] M. Papanikolaou and K. Salonitis, "Contact stiffness effects on nanoscale high-speed grinding: A molecular dynamics approach," *Appl. Surf. Sci.*, vol. 493, no. July, pp. 212–224, 2019, doi: 10.1016/j.apsusc.2019.07.022.

[111] W. König and K. Steffens, "A Numerical Method to Describe the Kinematics of Grinding," *CIRP Ann. - Manuf. Technol.*, vol. 31, no. 1, pp. 201–204, 1982, doi: 10.1016/S0007-8506(07)63297-1.

[112] K. Steffens and W. König, "Closed Loop Simulation of Grinding," *CIRP Ann. - Manuf. Technol.*, vol. 32, no. 1, pp. 255–259, 1983, doi: 10.1016/S0007-8506(07)63400-3.

[113] I. Inasaki, "Grinding Process Simulation Based on the Wheel Topography Measurement," *CIRP Ann. - Manuf. Technol.*, vol. 45, no. 1, pp. 347–350, 1996, doi: 10.1016/S0007-8506(07)63077-7.

[114] D. A. Doman, A. Warkentin, and R. Bauer, "Finite element modeling approaches in grinding," *Int. J. Mach. Tools Manuf.*, vol. 49, no. 2, pp. 109–116, 2009, doi: 10.1016/j.ijmachtools.2008.10.002.

[115] D. A. Doman, R. Bauer, and A. Warkentin, "Experimentally validated finite element model of the rubbing and ploughing phases in scratch tests," *Proc. Inst. Mech. Eng. Part B J. Eng. Manuf.*, vol. 223, no. 12, pp. 1519–1527, 2009, doi: 10.1243/09544054JEM1520.

[116] X. Chena and T. T. Öpözb, "Simulation of grinding surface creation - A single grit approach," *Adv. Mater. Res.*, vol. 126–128, no. November 2014, pp. 23–28, 2010, doi: 10.4028/www.scientific.net/AMR.126-128.23.

[117] D. Anderson, A. Warkentin, and R. Bauer, "Experimental and numerical investigations of single abrasive-grain cutting," *Int. J. Mach. Tools Manuf.*, vol. 51, no. 12, pp. 898–910, 2011, doi: 10.1016/j.ijmachtools.2011.08.006.

[118] J. G. Yang, Z. X. Zhou, B. Z. Li, and D. H. Zhu, "Study on the simulation model and high-speed characteristics of cylindrical grinding," *Adv. Mater. Res.*, vol. 223, pp. 826–835, 2011, doi: 10.4028/www.scientific.net/AMR.223.826.

[119] X. lei Zhang, B. Yao, W. Feng, Z. huang Shen, and M. meng Wang, "Modeling of a virtual grinding wheel based on random distribution of multi-grains and simulation of machine-process interaction," *J. Zhejiang Univ. Sci. A*, vol. 16, no. 11, pp. 874–884, 2015, doi: 10.1631/jzus.A1400316.

[120] X. Chen, T. T. Opoz, and A. Oluwajobi, "Analysis of grinding surface creation by single-grit approach," *J. Manuf. Sci. Eng. Trans. ASME*, vol. 139, no. 12, pp. 1–10, 2017, doi: 10.1115/1.4037992.

[121] D. Anderson, A. Warkentin, and R. Bauer, "Experimental validation of numerical thermal models for dry grinding," *J. Mater. Process. Technol.*, vol. 204, no. 1–3, pp. 269–278, 2008, doi: 10.1016/j.jmatprotec.2007.11.080.

[122] B. Linke, M. Duscha, A. T. Vu, and F. Klocke, "FEM-based simulation of temperature in speed stroke grinding with 3D transient moving heat sources," *Adv. Mater. Res.*, vol. 223, pp. 733–742, 2011, doi:

10.4028/www.scientific.net/AMR.223.733.

[123] A. M. O. Mohamed, A. Warkentin, and R. Bauer, "Variable heat flux in numerical simulation of grinding temperatures," *Int. J. Adv. Manuf. Technol.*, vol. 63, no. 5–8, pp. 549–554, 2012, doi: 10.1007/s00170-012-3948-z.

[124] J. Kundrák, A. P. Markopoulos, and N. E. Karkalos, "Numerical Simulation of Grinding with Realistic Representation of Grinding Wheel and Workpiece Movements: A Finite Volumes Study," *Procedia CIRP*, vol. 58, pp. 275–280, 2017, doi: 10.1016/j.procir.2017.03.192.

[125] S. Radzevich, *Handbook of practical gears design and manufacture*. .

[126] G. Guerrini, F. Lerra, and A. Fortunato, "The effect of radial infeed on surface integrity in dry generating gear grinding for industrial production of automotive transmission gears," *J. Manuf. Process.*, 2019, doi: 10.1016/j.jmapro.2019.07.006.

[127] G. Guerrini, A. H. A. Lutey, S. N. Melkote, A. Ascari, and A. Fortunato, "Dry generating gear grinding: Hierarchical two-step finite element model for process optimization," *J. Manuf. Sci. Eng. Trans. ASME*, vol. 141, no. 6, pp. 1–9, 2019, doi: 10.1115/1.4043309.

[128] G.Guerrini, "Alma Mater Studiorum – Dottorato di ricerca in meccanica e scienze avanzate dell'ingegneria - MODELLAZIONE DEL PROCESSO DI RETTIFICA A SECCO PER GENERAZIONE DI INGRANAGGI DI IMPIEGO AUTOMOBILISTICO," 2014.

[129] F. Lerra, E. Liverani, E. Landi, and A. Fortunato, "Real single grain grinding FEM simulation for case-hardened steel based on equivalent contact area analysis," *J. Manuf. Sci. Eng.*, pp. 1–24, 2021, doi: 10.1115/1.4051536.

[130] G. Q. Cai, B. F. Feng, T. Jin, and Y. D. Gong, "Study on the friction coefficient in grinding," *J. Mater. Process. Technol.*, vol. 129, no. 1–3, pp. 25–29, 2002, doi: 10.1016/S0924-0136(02)00569-1.

[131] F. Klocke, C. Wrobel, M. Rasim, and P. Mattfeld, "Approach of Characterization of the Grinding Wheel Topography as a Contribution to the Energy Modelling of Grinding Processes," *Procedia CIRP*, vol. 46, pp. 631–635, 2016, doi: 10.1016/j.procir.2016.04.011.

[132] M. Barge, H. Hamdi, J. Rech, and J. M. Bergheau, "Numerical modelling of orthogonal cutting: Influence of numerical parameters," *J. Mater. Process. Technol.*, vol. 164–165, no. October, pp. 1148–1153, 2005, doi: 10.1016/j.jmatprotec.2005.02.118.

[133] P. J. Arrazola, T. Özel, D. Umbrello, M. Davies, and I. S. Jawahir, "Recent advances in modelling of metal machining processes," *CIRP Ann. - Manuf. Technol.*, vol. 62, no. 2, pp. 695–718, 2013, doi: 10.1016/j.cirp.2013.05.006.

[134] C. Wang, F. Ding, D. Tang, L. Zheng, S. Li, and Y. Xie, "Modeling and simulation of the high-speed milling of hardened steel SKD11 (62 HRC) based on SHPB technology," *Int. J. Mach. Tools Manuf.*, vol. 108, pp. 13–26, 2016,

doi: 10.1016/j.ijmachtools.2016.05.005.

[135] R. Eisseler, K. Drewle, K. C. Grötzinger, and H. C. Möhring, "Using an inverse cutting simulation-based method to determine the Johnson-Cook material constants of heat-treated steel," *Procedia CIRP*, vol. 77, no. Hpc, pp. 26–29, 2018, doi: 10.1016/j.procir.2018.08.198.

[136] Y. Wang, C. Li, B. Li, M. Yang, and X. Zhang, "Advances and Recent Patents in the Field of Grinding Temperature Measurement Methods," *Recent Patents Mater. Sci.*, vol. 8, no. 1, pp. 55–68, 2015, doi: 10.2174/1874464808666150304233653.

[137] A. Brosse, P. Naisson, H. Hamdi, and J. M. Bergheau, "Temperature measurement and heat flux characterization in grinding using thermography," *J. Mater. Process. Technol.*, vol. 201, no. 1–3, pp. 590–595, 2008, doi: 10.1016/j.jmatprotec.2007.11.267.

[138] R. Pavel and A. Srivastava, "An experimental investigation of temperatures during conventional and CBN grinding," *Int. J. Adv. Manuf. Technol.*, vol. 33, no. 3–4, pp. 412–418, 2007, doi: 10.1007/s00170-006-0771-4.

[139] A. Lefebvre, P. Vieville, P. Lipinski, and C. Lescalier, "Numerical analysis of grinding temperature measurement by the foil/workpiece thermocouple method," *Int. J. Mach. Tools Manuf.*, vol. 46, no. 14, pp. 1716–1726, 2006, doi: 10.1016/j.ijmachtools.2005.12.009.

[140] A. Lefebvre, F. Lanzetta, P. Lipinski, and A. A. Torrance, "Measurement of grinding temperatures using a foil/workpiece thermocouple," *Int. J. Mach. Tools Manuf.*, vol. 58, pp. 1–10, 2012, doi: 10.1016/j.ijmachtools.2012.02.006.

[141] B. Denkena, A. Bouabid, and A. Kroedel, "Single grain grinding: a novel approach to model the interactions at the grain/bond interface during grinding," *Int. J. Adv. Manuf. Technol.*, vol. 107, no. 11–12, pp. 4811–4822, 2020, doi: 10.1007/s00170-020-05219-8.

[142] W. F. Ding, J. H. Xu, Z. Z. Chen, C. Y. Yang, C. J. Song, and Y. C. Fu, "Fabrication and performance of porous metal-bonded CBN grinding wheels using alumina bubble particles as pore-forming agents," *Int. J. Adv. Manuf. Technol.*, vol. 67, no. 5–8, pp. 1309–1315, 2013, doi: 10.1007/s00170-012-4567-4.

[143] W. F. Habrat, "Effect of bond type and process parameters on grinding force components in grinding of cemented carbide," *Procedia Eng.*, vol. 149, no. June, pp. 122–129, 2016, doi: 10.1016/j.proeng.2016.06.646.

[144] B. ZHAO, T. YU, W. DING, and X. LI, "Effects of pore structure and distribution on strength of porous Cu-Sn-Ti alumina composites," *Chinese J. Aeronaut.*, vol. 30, no. 6, pp. 2004–2015, 2017, doi: 10.1016/j.cja.2017.08.008.

[145] V. Gopan and K. L. D. Wins, "Quantitative Analysis of Grinding Wheel Loading Using Image Processing," *Procedia Technol.*, vol. 25, no. Raerest, pp. 885–891, 2016, doi: 10.1016/j.protcy.2016.08.198.

[146] A. Zahedi and B. Azarhoushang, "FEM Based Modeling of Cylindrical Grinding Process Incorporating Wheel Topography Measurement," *Procedia CIRP*, vol. 46, pp. 201–204, 2016, doi: 10.1016/j.procir.2016.03.179.

[147] R. L. Hecker, S. Y. Liang, and X. Jian, "Grinding force and power modeling based on chip thickness analysis," pp. 449–459, 2007, doi: 10.1007/s00170-006-0473-y.

[148] R. L. Hecker, I. M. Ramoneda, and S. Y. Liang, "Analysis of wheel topography and grit force for grinding process modeling," *Trans. North Am. Manuf. Res. Inst. SME*, vol. 31, pp. 281–288, 2003.

[149] F. Klocke *et al.*, "Modelling of the Grinding Wheel Structure Depending on the Volumetric Composition," *Procedia CIRP*, vol. 46, pp. 276–280, 2016, doi: 10.1016/j.procir.2016.04.066.

[150] K. Salonitis, P. Stavropoulos, and A. Kolios, "External grind-hardening forces modelling and experimentation," *Int. J. Adv. Manuf. Technol.*, vol. 70, no. 1–4, pp. 523–530, 2014, doi: 10.1007/s00170-013-5260-y.

[151] K. Salonitis, T. Chondros, and G. Chryssolouris, "Grinding wheel effect in the grind-hardening process," *Int. J. Adv. Manuf. Technol.*, vol. 38, no. 1–2, pp. 48–58, 2008, doi: 10.1007/s00170-007-1078-9.

[152] V. Gopan and K. L. D. Wins, "Quantitative Analysis of Grinding Wheel Loading Using Image Processing," *Procedia Technol.*, vol. 25, no. Raerest, pp. 885–891, 2016, doi: 10.1016/j.protcy.2016.08.198.

[153] A. Fortunato, A. Ascari, E. Liverani, L. Orazi, and G. Cuccolini, "A comprehensive model for laser hardening of carbon steels," *J. Manuf. Sci. Eng. Trans. ASME*, vol. 135, no. 6, pp. 1–8, 2013, doi: 10.1115/1.4025563.

[154] Z. B. Hou and R. Komanduri, "On the mechanics of the grinding process - Part I. Stochastic nature of the grinding process," *Int. J. Mach. Tools Manuf.*, vol. 43, no. 15, pp. 1579–1593, 2003, doi: 10.1016/S0890-6955(03)00186-X.

[155] A. Sue and G. Schajer, *Material Factors - Handbook of residual stressand deformation of steel*. 2002.

[156] AGMA 915-1-A02, "Inspection Practices - Part 1: Cylindrical Gears - TangentialMeasurements," p. 46, 2002.

[157] B. Denkena, A. Schindler, and S. Woiwode, "Calculation method of the contact area in flank machining for continuous generating grinding," *Appl. Math. Model.*, vol. 40, no. 15–16, pp. 7138–7146, 2016, doi: 10.1016/j.apm.2016.02.030.